UNIVERSITÀ DI PARMA

Università degli Studi di Parma

Dottorato di Ricerca in Tecnologie dell'Informazione

XXXV Ciclo

System-level models for Smart Grid simulations and their integration into a campus Micro Grid model

Coordinatore:
Prof. Marco Locatelli

Tutor:
Prof. Roberto Menozzi

Dottorando: *Marco Simonazzi*

Anni Accademici 2019/2020 – 2021/2022

Contents

List of Figures

List of Tables

List of Acronyms

AC	Alternating Current
BESS	Battery Energy Storage System
CC/CV	Constant Current/Constant Voltage
c-HIL	control-HIL
CHP	Combined Heat and Power
DC	Direct Current
DER	Distributed Energy Resources
DG	Distributed Generator
DoD	Depth of Discharge
DT	Digital Twin
EMT	Electromagnetic Transient
ESS	Energy Storage System
EV	Electric Vehicle
FC	Fuel Cell
FET	Field Effect Transistor
FSM	Finite State Machine
GHG	Green House Gas
HIL	Hardware-in-the-Loop
ICT	Information And Communication Technologies
ISA95	International Society of Automation-95
LED	Light Emitting Diodes
LPT	Load Power Tracking
MBD	Model-based Design
MG	Micro Grid
MGCC	Microgrid Central Controller
MIL	Model-in-the-Loop

MPP	Maximum Power Point
MPPT	Maximum Power Point Tracking
MV	Medium Voltage
NG	Nano Grid
NPG	National Power Grid
PCC	Point of Common Coupling
PDN	Power Distribution Network
PG	Power Grid
p-HIL	power-HIL
PI	Proportional-Integrative (controller)
PIL	Processor-in-the-Loop
PSO	Particle Swarm Optimization
PV	Photovoltaic
PWM	Pulse Width Modulation
RES	Renewable Energy Sources
SC	Smart City
SC4SL	Smart City 4.0 Sustainable LAB
SCADA	Supervisory Control and Data Acquisition
SF	Soiling Factor
SIL	Software-in-the-Loop
SOA	Safe Operating Area
SoC	State of Charge
TSO	Transmission System Operator
UPSC	University of Parma South Campus

Introduction

Nowadays humanity is called to respond to important challenges dictated by the economic, social and environmental crisis we are currently experiencing.

This requires, in a relatively short time, a radical change in society, concerning many of its aspects. In the last decades, people have become more and more accustomed to living with technologies, that have become essential tools in everyday life. For this reason, technology is called to be the main enabler to respond to the requirements dictated by the ecological transition. However, it is immediate to understand how technology, for its own sake, is not enough. Educating people to live in a smarter and sustainable way is essential in order to look forward to the years to come with confidence. We have to rethink the way we live together on a territory, work and produce locally and globally.

In this context, the concept of Smart City opens the possibility to integrate and cooperate all the main aspects of the life of the society with the aim of reaching a more equal, inclusive and, above all, sustainable living. In the long term, it will also enable us to adopt a sustainable development approach, by favoring renewable energies, modifying our consumption behavior, and limiting waste. In fact, unsustainable consumption of resources and development patterns are having serious impact on our planet, as is the depletion of natural resources, pollution, reduced biodiversity and increased environmental problems.

This Smart City approach requires a holistic perspective that differs from the traditional one where thematic issues were studied independently. This is due both to the need to reconcile and integrate multiple specific viewpoints and disciplines, and to the wide range of stakeholders (individual citizens, administrators, the business world, etc.) [1].

From an energy management perspective, electrical energy has a central role in the future of cities. In fact, energy efficiency optimization and local self-sufficiency are crucial achievements in facing traditional resources run-out and global market instability and unreliability.

The shift toward renewable energy sources (e.g., photovoltaic, solar, wind, geothermal, biomass/biogas, etc.) implies the widespread diffusion of distributed generation, generally, on a small and medium scale. These energy sources are often characterized by erratic and non-dispatchable nature, in that they are strictly dependent on meteorological and environmental conditions or based on irregularly available raw matter. The result is that one main point of the modern grid is to bring together, in terms of availability in time, the offer of energy with the load demand. This requires the installation of energy storage systems that can store the energy in excess and give it back when there is a deficit of production. In this context, the grid of the future will have to be a Smart Grid.

Proper sizing of the components of a Smart Grid, as well as studying the introduction of new components, namely renewable generation, storage, etc., and ensuring acceptable system reliability and security, is not a trivial task. Offline simulation models and Digital Twins, together with the already partially present supervisory, control and monitoring systems, open the way for new smart tools for Smart Grid planning, development, and live automated control. In this perspective, it is necessary to implement system-level models with tight execution-time constraints. In fact, they must be able to run in real-time (e.g., in live Digital Twins) or even faster than real-time (to allow making predictions on the evolution of the system). Therefore, it is necessary to move from the traditional modelling approach, based on detailed physical models, to top-level behavioral models.

This dissertation is organized as follows.

- Chapter 1 gives an overview about the Smart Grids and their role in the Smart City framework. After introducing the concepts of Smart City and Smart Grid, highlighting the main aims and assets of each one, a brief study on Micro Grid architectures (1.4.1) and control (1.4.2) is presented, coming from a literature review work carried out during the PhD years. Then, in 1.5, the focus is moved to the state of the art on Smart

Grid simulations, introducing the main topic of the work, detailed in Chapter 2.

- Chapter 2 presents the main research activity carried out. The simulation model of a campus-level Micro Grid is presented, showing details about the developed library of components and considerations on the chosen approach. The University of Parma South Campus is taken as an example of a district-level grid, conceived to accommodate, in the next years, all the elements to build a Smart Micro Grid.
- Chapter 3 presents a smart soiling monitoring system for photovoltaic modules developed at the university campus. Here it is shown how the models implemented in Chapter 2 can be customized to model a Nano Grid where new concepts (like the smart soiling sensor) can be included in order to test their effectiveness and effect through long-time (tens of years) simulations.
- Chapter 4 gives a further example involving the simulation library. In this case, the simulation model of a DC Nano Grid is developed to design and size the power supply system to charge a fleet of industrial electric vehicles. The model includes the behavior of the vehicles, of the charging stations and of the job scheduling algorithm coordinating the vehicles' operation.
- Chapter 5 presents a work carried out in collaboration with Infineon Technologies Austria. Here the behavioral modelling approach is applied to the case of on-board automotive power distribution networks. Behavioral modelling allows to perform mission profile simulations keeping the simulation time within reasonable bounds. This allows system designers to study the interaction between components at different levels of the distribution network, also in an early development stage, when physical prototypes are not yet available.

This PhD work is part of the Smart City 4.0 Sustainable LAB funded by the Emilia-Romagna region (see 1.2).

Chapter 1

Smart Cities and Smart Grids

The concept of Smart City (SC) is very wide, with numerous facets related with the areas in which it is inserted. In the literature, the origin of the term "Smart City" is traced back to the end of the 19th century and it gained popularity in the 20th century [2]. Since the beginning, the concept of Smart City was related to ideas about the future of society, economy, and urban settlements under the effect of the advancing technologies.

1.1 Definition of Smart City

In the literature there is no unique definition of SC. In 2014 the International Telecommunication Union presented a study of definitions and terms associated to the smart sustainable city topic. They found out more than one hundred different definitions reviewing articles obtained from a variety of sources, covering all the areas of interest on the topic, from academia and research communities, government initiatives, international organizations, corporate/company profiles, trade associations, standards development organizations, etc. [3]. The most frequently recurring keywords in SC definitions have been grouped in 8 categories:

1) quality of life and lifestyle,
2) infrastructure and services,

3) Information Communication Technologies (ICT), communication, intelligence, information,
4) people, citizens, society,
5) environment and sustainability,
6) governance, management, and administration,
7) economy and finance,
8) mobility.

The chart in Figure 1.1 gives a comprehensive view of the number of occurrences of the keywords found for each category.

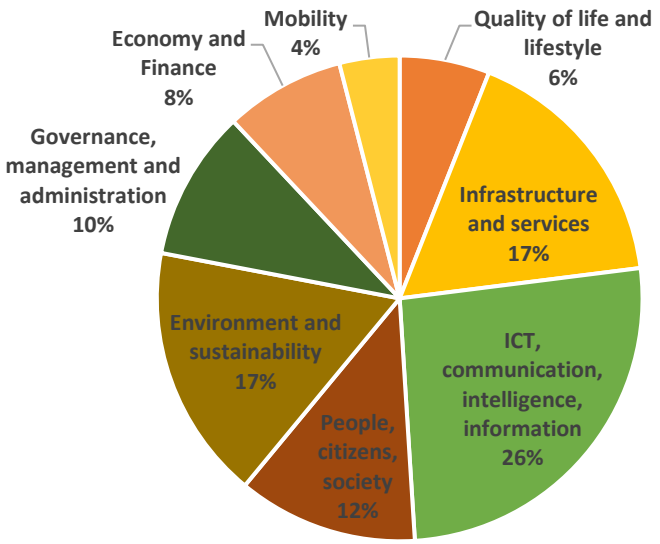

Figure 1.1: Number of smart city related keyword for each category found by the International Telecommunication Union.

What most smart city definitions have in common is the statement of the need to consider an innovative and forward-looking use of the infrastructural systems, with positive outcomes on the climate, environment, and social and economic impact. Among them, electricity is identified as a key factor for its central role in modern life, and the increasing relative weight in the energy use. In addition, it requires a network of sensors and communication systems for capturing and sharing information. The energy systems and the city itself will have to be flexible, adapting to

the different conditions and needs (population, environment, governance, mobility requirements), and anticipating the potential variations in all components and at all levels in the constituent systems [4].

Another important element to take into consideration when giving a definition of smart city is that although the conceptual view of smart cities can have a general validity, all implementations will inevitably be local. Each city is unique; each energy grid is unique; and their design, operation, and path to smartness will be unique. However, this fact accentuates the value of a common reference framework for the evaluation of the impacts potentially deriving from the implementation of Smart Grids (SG) and cities. This common framework will allow comparing results, learning common lessons, reflecting on the relative value of technologies and services, and most importantly of the opportunities for replicating, adjusting, and scaling up solutions.

1.2 The Smart City 4.0 Sustainable LAB initiative

The Smart City 4.0 Sustainable LAB (SC4SL) is a local research laboratory initiative of the Emilia-Romagna region founded in 2018 at the University of Parma to support public administrations and institutions and local stakeholders in the smart city transition [5]. In 2019, it developed into an initiative involving all the universities of the Emilia-Romagna region with the aim of promoting a deeply interdisciplinary and holistic approach to the development of smart and wise cities that enclose the penetration of new technologies, the advancement of sustainability policies, the valorization of artistic and cultural heritage, and a principle of inclusiveness applied to both people and places.

In May 2019, a protocol of agreement was signed with the Emilia-Romagna Regional Government with the main goal of defining SC development lines over a three-year time horizon, and a program featuring several work directions, including academic research towards a working methodology for public administrations, pilot projects for city administrations and regional institutions, and educational support for public administrations and the definition of emerging issues.

The SC4SL is at the center of a regional-scale network made of 46 research groups and 292 researchers working in the regional universities, covering all the disciplines that can contribute to innovate and valorize contemporary cities. The working group (2019/2022) features 10 PhD students whose doctoral research started in November 2019, 10 supervisors and 10 tutors. The PhD positions are co-funded by the Regional Government and by the research groups of the participating universities, with the aim of developing SCs research lines through a long-term collaborative effort [6].

1.3 Smart Grids

The European Technology Platform of Smart Grids defines a SG (concept represented in Figure 1.2) as an electricity network that intelligently integrates the actions of all the users connected to it, namely generators, consumers and those that assume both roles (known as "prosumers") with the aim of efficiently delivering sustainable, economic and secure electricity supplies [7]. There are many other definitions, all of them highlighting the ability to automatically manage the energy production and demand making autonomous decisions with the aim of optimally accommodating the needs of the consumers and the availability of the producers. The National Institute of Standards and Technologies (NIST) defines the SG as a modern grid that allows bi-directional flows of energy and utilizes two-way communication and control capabilities that lead to a wide range of new functionalities and applications, in contrast to the state of the art of the present grid, where the energy is delivered unidirectionally from generation centers to consumption centers [8]. The Energy Independence and Security Act of 2007 conceives the SG as a modernization to the electrical network with monitoring capabilities, which increases grid resiliency to disruptions, and automatically optimizes grid operation of interconnected system components, starting from central generating units and distributed generation (DG) through transmission networks, down to load centers [9]. The US-based Electric Power Research Institute (EPRI) defines the smart grid as the transition from the current grid, where the flow of power is permitted from the central generation to load locations, into a

grid where there is a peer-to-peer consumer interactions, DG, and control centers [10].

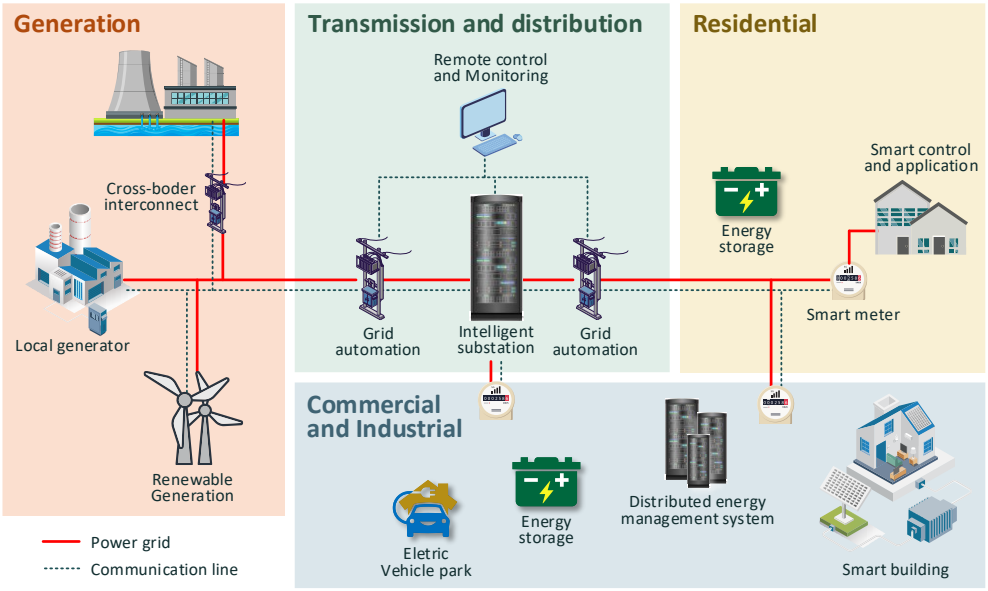

Figure 1.2: The Smart Grid concept.

Table 1.1 shows a comparison of the key aspects of the SG compared to the conventional PG.

Developing a smart grid would allow to flexibly manage the capacity and capabilities of the grid for accommodating variable power demand, integrating new sources of energy, managing bidirectional and flexible sub-grids, and to allow new players to participate in new energy markets. It is especially the renewable and distributed types of energy sources (wind, solar, small hydro) that require such smart flexibility to integrate them in the system without affecting the reliable operation of the grid. Therefore, the smart grid is one key technology for reaching the climate goals, which heavily rely on increasing the share of RES [11].

The smart grid framework involves (directly or indirectly) most of the assets and stakeholders of the SC. In fact, as highlighted in Figure 1.3, the main asset, namely the technical one, is inevitably linked with other two important assets: environment

and economy. The interactions between these three aspects necessarily involve stakeholders pertaining to the most varied areas of the society.

From this, it emerges that the concept of SG is closely related to the concept of SC, nevertheless, it is important to underline that a SG can be built as a standalone infrastructure applying only to the energetic aspects. However, to reach a complete smartness, it is not sufficient to have a SG, it is necessary to have an entirely smart system covering most of the aspects of the SC framework (Figure 1.4). An obvious example is given by the future of transportation systems and vehicles migrating to the electric power supply.

Table 1.1: Comparison of the main aspects of a conventional and a smart grid.

Conventional Grid	***vs***	**Smart Grid**
One-directional communication		Bi-directional communication
Electromechanical		Digital
Large capacity central generation		Distributed generation with various capacities
Limited number of sensors		Sensors dominant system
Less scope for self-monitoring		Complete scope for self-monitoring
Less scope for automatic restoration		Complete scope for Automatic restoration or Self-healing
Less adaptable in case of failures and blackouts		Adaptive and allows islanding
Restricted control		Ubiquitous control
Limited choices for consumers		Wide variety of choices for consumers
Hierarchical structure		Network structure
Less feasible for feedback network		The inherent and real-time control
Wide area interrupts at the time of outage		Filtering and islanding disconnection
Network restriction control		Network comprehensive control
Customers and subscriptions provided with limited services		Customers and subscriptions provided with various services
Radial Network		Dispersed Network
Slower in response during emergencies		Quicker in response during emergencies
Small volumes of data available		Large quantities of data available

A SG must be:

- **flexible**: fulfilling customers' needs whilst responding to the changes and challenges ahead;

- **accessible**: granting connection access to all network users, particularly for renewable power sources and high efficiency local generation with zero or low carbon emissions;
- **reliable**: assuring and improving security and quality of supply, consistent with the demands of the digital age with resilience to hazards and uncertainties;
- **economic**: providing best value through innovation, efficient energy management and level-playing-field competition and regulation.

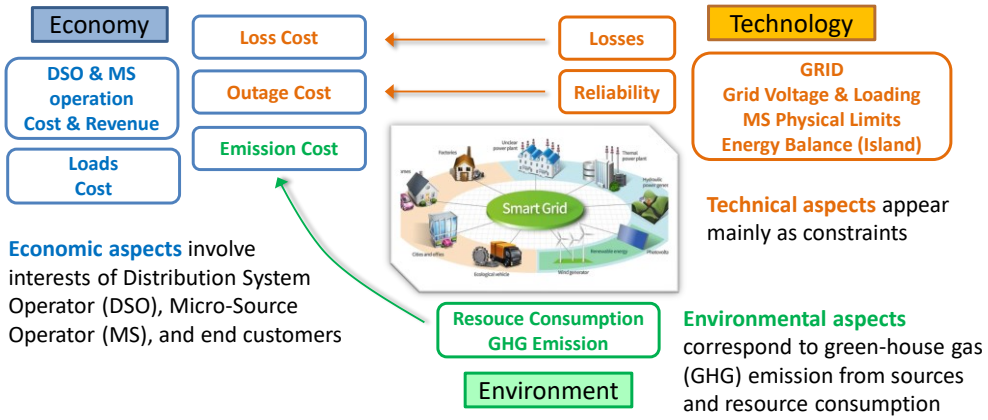

Figure 1.3: SGs involve most of the assets and stakeholders of the SC.

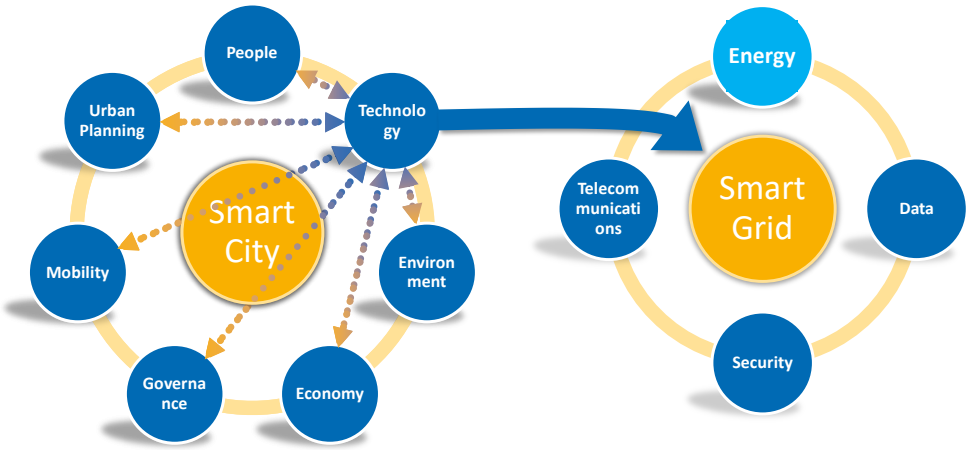

Figure 1.4: SC and SG intercorrelation.

These requirements come from the main future needs of the electricity grid stakeholders, namely:

- **user-centric approach**: increased interest in electricity market opportunities, value added services, flexible demand for energy, lower prices, micro-generation opportunities;
- **electricity network renewal and innovation**: pursuing efficient asset management, increasing the degree of automation for better quality of service; using system wide remote control; applying efficient investments to solve infrastructure ageing;
- **security of supply**: limited primary resources of traditional energy sources, flexible storage; need for higher reliability and quality; increase network and generation capacity;
- **liberalized markets**: responding to the requirements and opportunities of liberalization by developing and enabling both new products and new services; high demand flexibility and controlled price volatility, flexible and predictable tariffs; liquid markets for trading of energy and grid services;
- **interoperability of electricity networks**: supporting the implementation of the internal market; efficient management of cross border and transit network congestion; improving the long-distance transport and integration of renewable energy sources; strengthening security of supply through enhanced transfer capabilities;
- **DG and (RES)**: local energy management, losses and emissions reduction, integration within power networks;
- **central generation**: renewal of the existing power-plants, development of efficiency improvements, increased flexibility towards the system services, integration with RES and DG;
- **environmental issues:** reaching Kyoto Protocol targets; evaluate their impact on the electricity transits; reduce losses; increasing social responsibility and sustainability; optimizing visual impact and land-use; reduce permission times for new infrastructure;
- **demand response and demand side management:** developing strategies for local demand modulation and load control by electronic metering and automatic meter management systems;

- **politics and regulatory aspects:** continuing development and harmonization of policies and regulatory frameworks;
- **social and demographic aspects:** considering changed demand of an ageing society with increased comfort and quality of life [12].

The core of the SG operation is the energy management which ensures that the stability between supply and demand is maintained, while respecting all system constraints for economical, reliable, and safe operation of the electrical system. It also includes optimization, which ensures a reduction in the cost of power generation.

Generators, retailers, and consumers view the transmission network as a public resource to which they should have unlimited access. This approach has the desirable effect of pushing the system towards an optimal utilization of the assets. However, this optimization is constrained by security limits since wide-spread service interruptions spanning over long periods of time are unacceptable in our modern societies due to their huge economic and social costs. Since transmission system operators are responsible for maintaining the reliability of the electric power system, they must therefore define the operating limits (security constraints) that must be respected.

While energy management in a distribution system helps improve system performance, it also presents limitations and challenges, such as confidentiality on the customer side, operations in a large system, regular system upgrades, and reliability issues. To adjust the flow of electricity exchanged from suppliers to consumers, to improve flexible and reliable grids, the integration of numerous components as RES, distributed control rooms and ESSs is needed. This requires the use of information and communication technologies (ICT) from the points of generation to customers in a smart way, as an integral part of the SG framework.

A key element in SG implementation are the smart meters, namely, digital sensors coupled to intelligent control systems implementing smart metering techniques, running analytical algorithms for automating, controlling and monitoring the bidirectional flow of electricity between source and user. Smart metering, control and actuation require real-time, two-way communication to permit, among other things, fast recovery of power service after a blackout: rotating power outages can cause a disruptive domino effect that negatively impacts banking, communications, manufacturing, traffic and security.

The widespread use of online ICT systems and communication networks, however, exposes to cyber-attacks. Hackers can access the supposedly protected data and

inject false information into the grid measurements, which cannot be easily detected by existing operational practices.

1.4 Micro Grids and Nano Grids

Micro Grids (MG) are small-scale (e.g., district-level) electrical distribution networks consisting of distributed generators (renewable and/or non-renewable generators), heterogenous loads, and energy storage devices that operate in grid-connected or islanded mode, coordinated and interfaced by suitable power electronic converters and devices [13].

The power delivered by RES in the early stages of their integration in the traditional grid was infinitesimal in comparison to the one coming from the conventional generators and, hence, their impact on the power network was quite unnoticeable. However, with recent developments and commitments toward renewable and sustainable power, RES such as photovoltaic (PV), wind, hydropower, and hydrogen power are rapidly penetrating the power grid. Therefore, microgrid small-scale operation facilitates flexibility to consolidate appropriate control schemes and power management algorithms to maintain the quality of power supplied to the local loads as well as the one exchanged with the higher-level SG [14]. The same applies when MGs are designed to establish a point of common coupling (PCC) that plays a key role in the formation of DC, AC, and hybrid AC-DC microgrids for various domains of voltage and frequency levels. In this respect, several power electronic interfacing configurations and topologies have been proposed not only to achieve a diversified power generation framework but also to enable MGs to manage the power and energy flows effectively [15], [16].

1.4.1 Micro Grid and Nano Grid Architectures

As schematically represented in Figure 1.5, MGs can be classified based on their topology in three major groups, namely, AC, DC and hybrid [17], [18]. NGs can operate as AC, DC or hybrid structures, too [19], [20], but they usually have smaller capacity and serve a smaller area (e.g., a single building or load) [21]–[23].

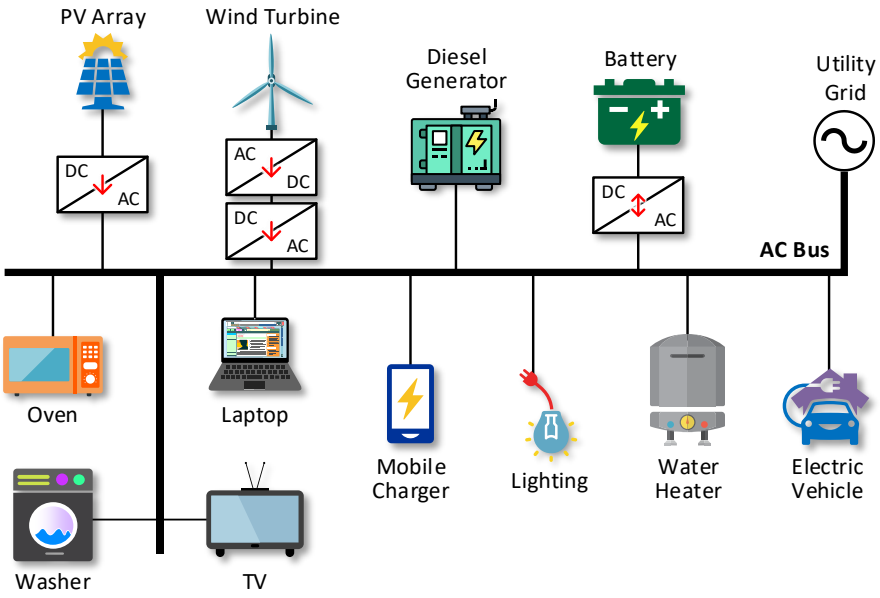
PV Array
Wind Turbine
Diesel Generator
Battery
Utility Grid
DC
AC
AC
DC
DC
AC
DC
AC
AC Bus
Oven
Laptop
Mobile Charger
Lighting
Water Heater
Electric Vehicle
Washer
TV

(a)

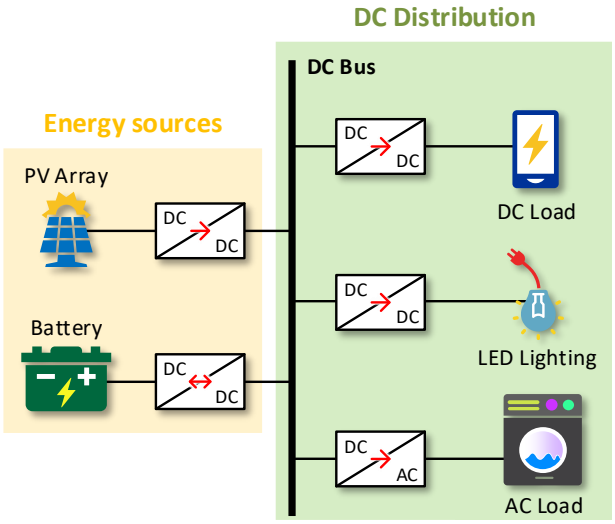
DC Distribution
DC Bus
Energy sources
PV Array
DC
DC
DC Load
DC
DC
LED Lighting
Battery
DC
DC
DC
AC
AC Load

(b)

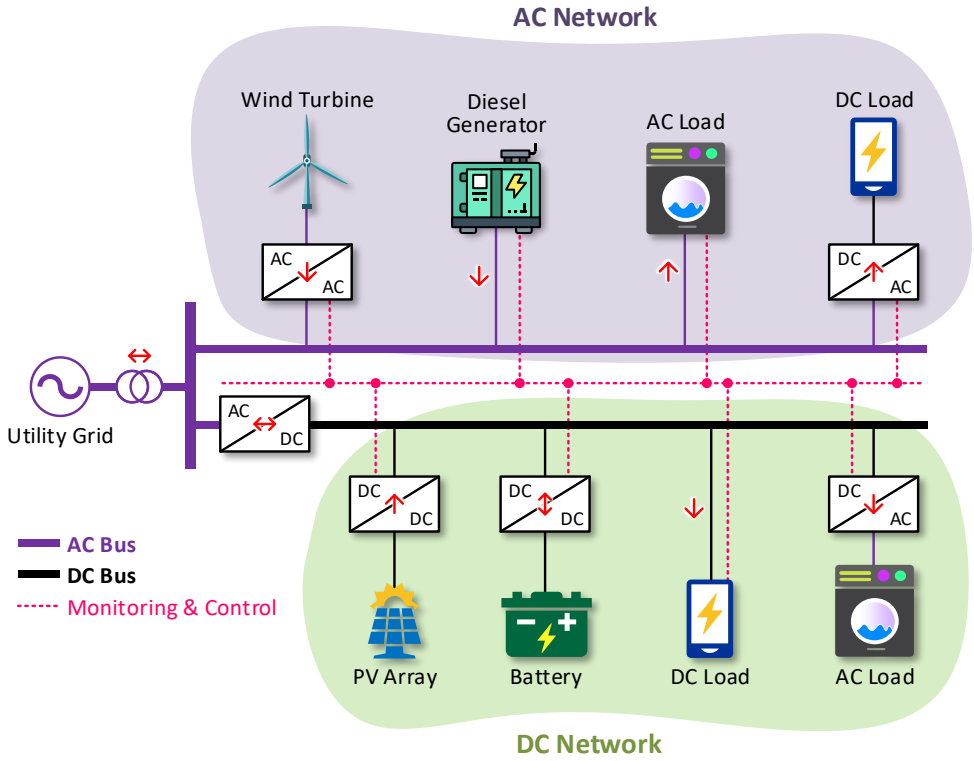

(c)

Figure 1.5: Main MG and NG architectures. (a) in an AC grid, (b) is a DC grid, (c) is a hybrid architecture with both AC and DC busses.

Another common trait between MGs and NGs is the ability to operate both in islanded and grid-connected mode [19].

Most of the power transmission in the world is based on AC technology, which historically imposed itself on DC transmission mainly thanks to easy transformer-based voltage step-up for long-distance dispatch [24], [25].

In the case of the AC NG of Figure 1.5a, energy flows into the AC NG feeder from the utility grid as well as from DERs that may be DC sources, such as PV arrays or batteries, requiring DC/AC converters; however, AC/DC/AC back-to-back converters are often utilized with AC power sources like wind farms, micro-turbines, or tidal power stations, to adapt the voltage level and frequency produced by the AC generators to the grid requirements [26]. On the other hand, large segments of

residential and commercial loads consist of low power electronics like personal computers, battery chargers, or LED lighting systems that require AC/DC conversion to be connected to an AC NG.

Connecting these DC loads directly or through high-efficiency DC/DC converters to the bus of a DC NG (Figure 1.5b) would reduce the need for energy conversion stages and improve the overall efficiency and reliability of the system [27], [28]. Recently, DC NGs have thus become increasingly attractive, also due to the improved performance and reduced cost of native DC systems such as PV, BESS, electric vehicles (EVs), fuel cells (FCs), which can be connected to a DC grid efficiently and reliably [18], [29]. In fact, avoiding double conversion from DC to AC on the generation side and from AC to DC at the load end, the system complexity is reduced and its efficiency and reliability are increased [23], [26], [30]. Moreover, the absence of reactive power in DC distribution lines reduces power losses and voltage drops and increases the capacity of electrical lines [26]. In [31], the transmitted power is found to increase up to a factor of ten moving from AC to three-line DC distribution.

Future DC NG will likely use two voltage levels: a high-voltage DC (e.g., 380 V) for home appliances or EV charging, and a low-voltage DC (e.g., 48 V) for supplying computers and low-power electronics [19], [21], [27], [32], hence the need for efficient DC/DC conversion.

The DC NG is connected to the utility grid via a bidirectional AC/DC converter that must be properly controlled to compensate for the voltage ripple arising on the DC voltage bus: ref. [33] discusses a zero-sequence operation mode of the converter and gives a summary of other ripple mitigation approaches.

Ref. [21] for example considers a commercial power system scenario with a large number of non-linear loads such as lighting appliances, computers, monitors, adjustable-speed drives for air conditioning, etc. A traditional grid scenario, where each load is supplied in AC, is compared with a DC-based architecture demonstrating that the latter is convenient from the efficiency, reliability and economic points of view. A DC bus voltage equal to the peak value of the standard 230 V AC line is shown to be the best solution for supplying native AC loads with DC power. This prevents overloading of the input rectifiers of the power supply units by lowering the amount of current flowing.

Ref. [34] describes a home-level, small power DC NG with an AC interface with the PG. A comparison between the modified DC version of the home appliances and

the legacy AC ones is carried out to show the convenience of the DC distribution. Ref. [35] also presents a residential-level NG implementation featuring a low voltage DC (LVDC) bus with an additional AC grid interface. Ref. [36] demonstrates the benefits of DC migration showing results of efficiency improvements of various system components in a commercial building supplied by 380 V DC and providing local 24 V plugs for small loads.

Finally, a hybrid NG (see Figure 1.5c) combines separately controlled AC and DC distribution lines, to exploit the advantages of both AC and DC grids [37]–[39]: DC loads and DERs can be connected to the DC bus, while AC loads and DERs can be connected to the AC bus, potentially eliminating the need for DC/AC/DC or AC/DC/AC conversion, thus increasing efficiency and reducing complexity and cost. In hybrid microgrids [40], the design can be optimized to minimize the cost of investments and maximize the energy efficiency through the optimal sizing of DERs, loads and ESSs following different approaches: a combination of different particle swarm optimization (PSO) based algorithms in [41], a multi-objective optimization of the mathematical model of the MG/NG aimed at minimizing daily energy consumption and greenhouse gas (GHG) emission [39], or through a time-of-use approach to reduce the cost of energy [42].

Ref. [43] presents a case study of hybrid AC-DC NG, part of a larger campus-level microgrid. The NG can operate in islanded mode in case of microgrid faults. The NG is equipped with two sets of PV arrays – separately connected to AC and DC subsystems – and a battery-based storage system used by both the subsystems to level-off the PV output power. The DC distribution bus features a 48 V DC voltage while the AC bus is a four wire, three-phase bus with 120 V line-to-neutral voltage. DC/DC buck converters interface a set of PV arrays with the DC subsystem. The other set of PV arrays is connected to the AC subsystem via DC/AC inverters. The AC and DC buses are interlinked through bidirectional AC/DC converters that transfer power between the two subsystems and regulate the bus voltage amplitudes. The NG connects with the higher-level MG on the AC side.

Most NGs, conceived as the evolution of an existing part of a legacy AC grid, are characterized by a hybrid topology, allowing to take advantage of the DC distribution while maintaining the possibility to power AC loads and to exchange energy with an upper-level distribution grid (usually in AC).

The architecture of a power system impacts its scalability, reliability, robustness, resilience, and cost. This means that it is possible to draw another classification for MGs and NGs considering the type of bus used for power distribution. An interesting comparative analysis of DC microgrid architectures which can be extended to AC and hybrid MGs and NGs was given in [44]. Here single-bus (Figure 1.6a,b), ring-bus (Figure 1.6c), zonal-bus (Figure 1.6d), ladder-bus (Figure 1.6e), and multi-terminal (Figure 1.6f) structures are compared in terms of bus voltage levels, BESS connection, inherent stability, expandability to multiple buses, and reliability. Each of these solutions has its own strengths and drawbacks, and more research in this area is necessary to reduce their complexity level and solve existing problems. However, in the absence of standardization, numerous optimal system architectures can be defined in relation to the chosen physical variables and to the requirements of the loads.

1.4.2 Micro Grid and Nano Grid Control

Together with the specific NG architecture, the adopted control strategy is another key aspect impacting on the choice and design of power converters.

Given the complexity of energy grids, the approach followed in the development of their control system is typically hierarchical [45], with a variety of possible solutions. As early as in 2010, the authors of ref. [46] proposed a general approach to hierarchical control of microgrids derived by the multilevel hierarchical control of the International Society of Automation-95 (ISA95) standard. The 6 levels envisioned by this standard can be reduced in this context to 4 (levels 0-3). As the considered level increases, stability and robustness of operation of the lower levels require a decreasing bandwidth of downward control and reference signals. The resulting 0-3 levels (Figure 1.7) are the following:

Level 0 – Inner control loops: The regulation of each power module is performed at this level. Both feedback and feedforward control loops can be implemented to regulate the output voltage and the current while keeping the system stable. This level supports load sharing among parallel-connected power converters.

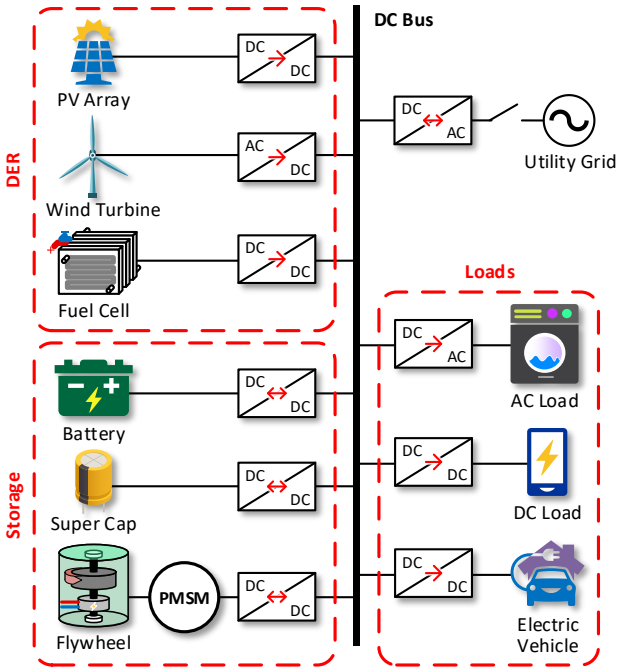
DC Bus
DER
PV Array
Wind Turbine
Fuel Cell
DC
DC
AC
DC
DC
DC
AC
Utility Grid
Loads
AC Load
DC Load
Electric Vehicle
Storage
Battery
Super Cap
Flywheel
PMSM

(a)

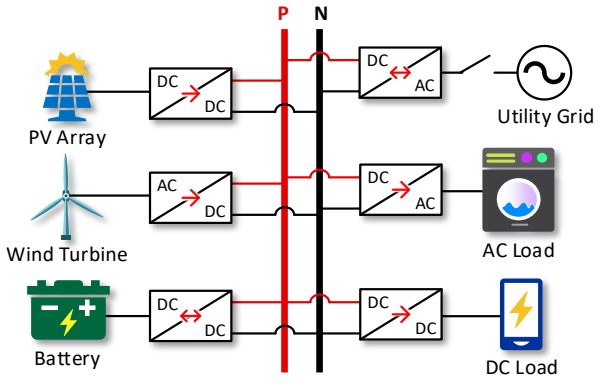
P
N
PV Array
Wind Turbine
Battery
DC
DC
AC
DC
DC
DC
DC
AC
DC
AC
DC
DC
Utility Grid
AC Load
DC Load

(b)

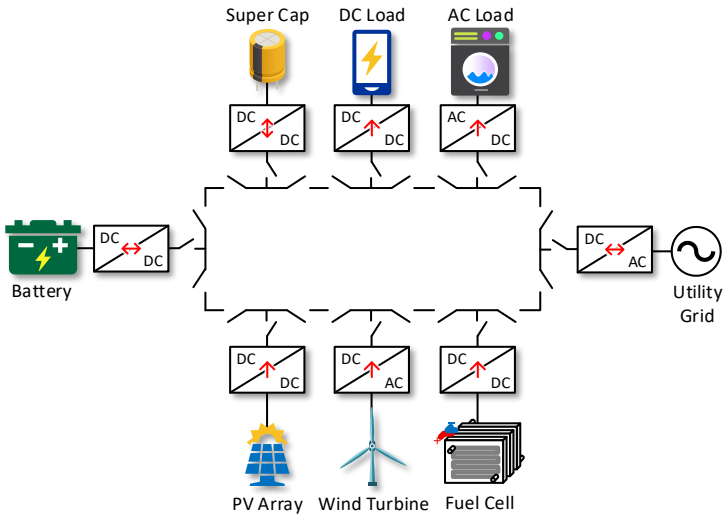
Super Cap
DC Load
AC Load
DC
DC
DC
DC
AC
DC
Battery
DC
DC
DC
AC
Utility
Grid
DC
DC
DC
AC
DC
DC
PV Array
Wind Turbine
Fuel Cell

(c)

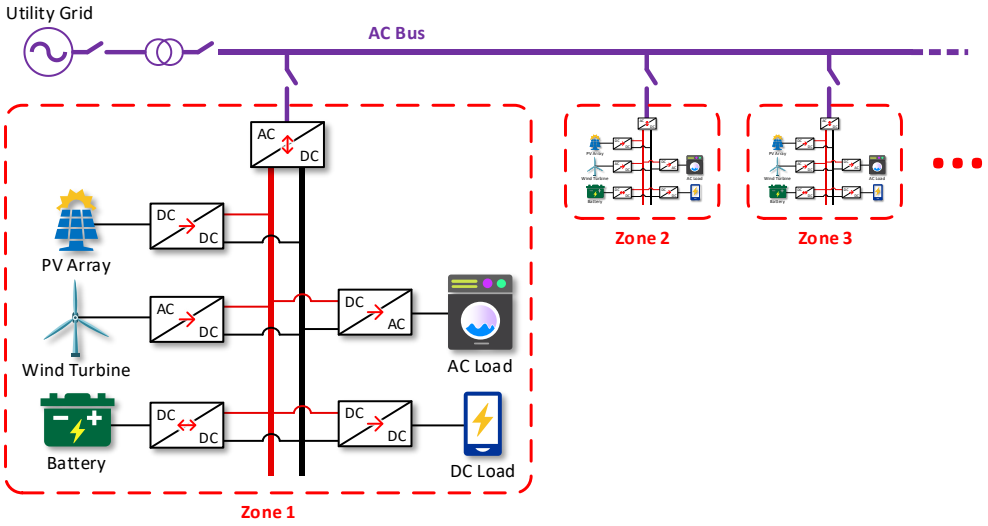
Utility Grid
AC Bus
AC
DC
PV Array
DC
DC
AC
DC
Wind Turbine
AC Load
DC
DC
DC
DC
Battery
DC Load
Zone 1
Zone 2
Zone 3

(d)

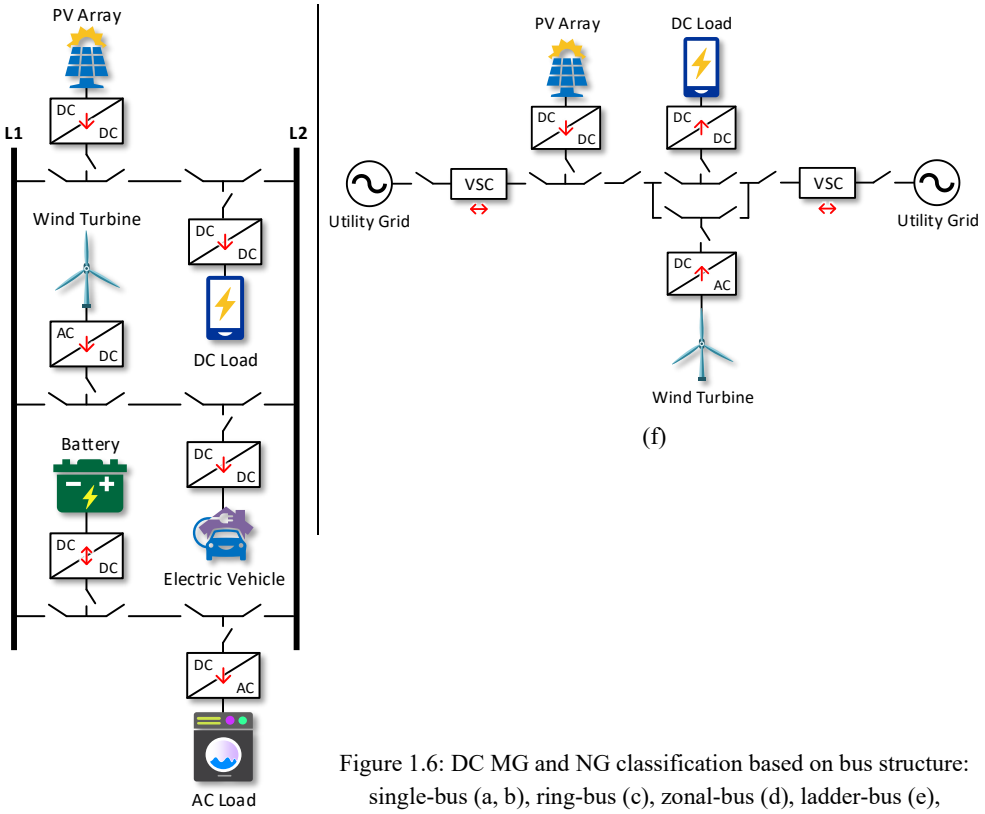

Figure 1.6: DC MG and NG classification based on bus structure: single-bus (a, b), ring-bus (c), zonal-bus (d), ladder-bus (e), multi-terminal (f).

Level 1 – Primary control: at this level a droop-control technique is typically applied for stability and damping which emulates the physical behavior of conventional sources; virtual impedance emulation can also be implemented.

Level 2 – Secondary control: some parameters of the primary control are passed to the secondary control to ensure that the electrical levels in the MG/NG are those required. This level can also include a synchronization control loop for seamless connection/disconnection with the utility grid to ensure smooth transitions between grid-connected and islanded modes.

Level 3 – Tertiary control: this level controls the power flows between the MG/NG and the utility grid. Here storage and source dispatching are scheduled by the distribution or transmission system operator (TSO).

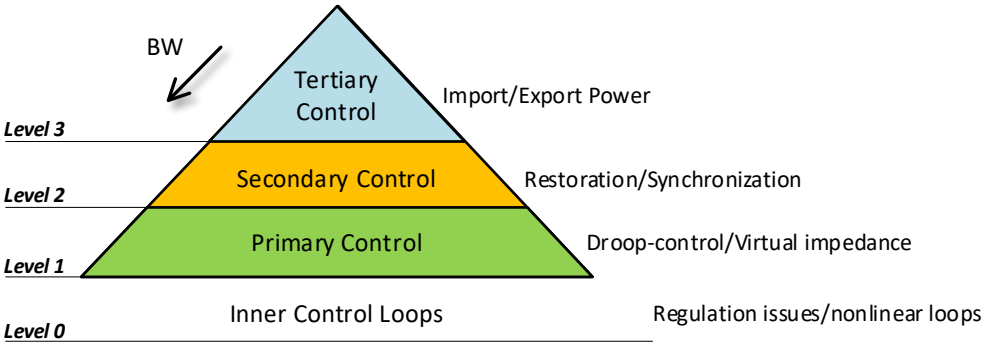

Figure 1.7: Graphical schematization of the general hierarchical control approach derived from ISA95 standard.

Figure 1.8 shows a hierarchical control structure with conventional droop control for AC microgrids proposed in [45]. The secondary control is used not only to synchronize all the microgrid units, but also to manage the synchronization between the microgrid with the main utility grid. Above secondary control, the tertiary control is used for controlling and managing the power flows between microgrid and main grid. At this level, one of the tasks can be power re-distribution among DERs. The optimum economic operating point is reached by regulating the set point of each resource unit [47].

Considering the voltage amplitude E_i and the angular speed ω_0 of the i-th inverter connected to the AC grid bus, the equations of the conventional P/ω and Q/E droop characteristics shown in Figure 1.9 are the following:

$$\omega_i = \omega_0 - G_{\omega\text{-}i} \cdot P_i \qquad E_i = E_0 - G_{E\text{-}i} \cdot Q_i \tag{1.1}$$

where P_i and Q_i are, respectively, the active and reactive power at the output of the i-th inverter, ω_0 is the angular frequency at no load, E_0 is the inverter output voltage at no load, and $G_{\omega\text{-}i}$ and $G_{E\text{-}i}$ are the frequency droop coefficient and voltage droop coefficient of the i-th inverter, respectively.

Droop coefficients are calculated as follows:

$$G_{\omega\text{-}i} = \frac{\Delta\omega}{P_{i\text{-}max}} \qquad G_{E\text{-}i} = \frac{\Delta E}{Q_{i\text{-}max}} \tag{1.2}$$

where $\Delta\omega$ and ΔE are the maximum accepted deviation of angular speed and voltage, respectively, and $P_{i\text{-}max}$ and $Q_{i\text{-}max}$ are the nominal active and reactive power supplied by the inverter, respectively.

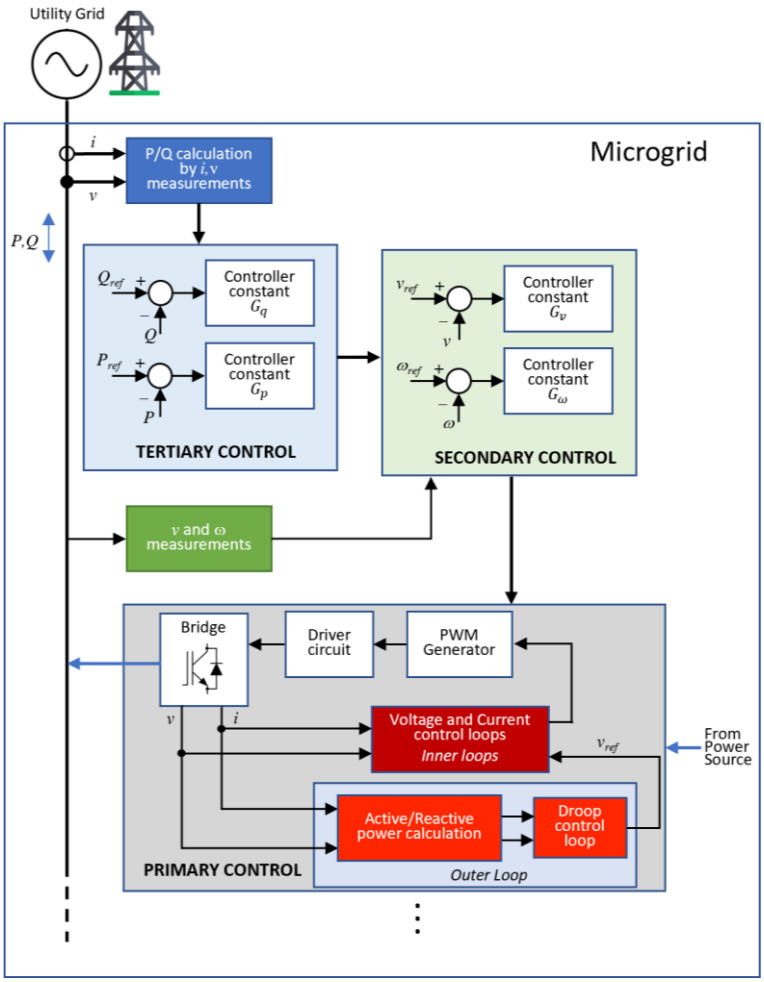

Figure 1.8: Hierarchical control structure with conventional droop control for AC microgrids.

One of the distinct advantages of droop control is that it does not require critical communication connections between parallel-connected converters, which improves the system reliability [48], [49].

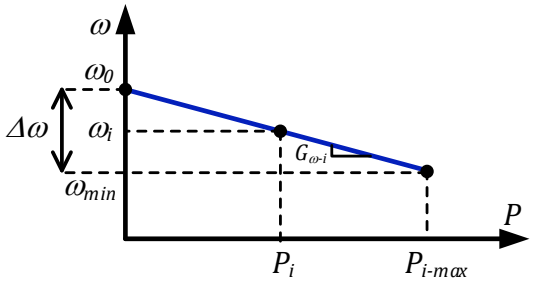

Figure 1.9: Conventional P/ω (a) and Q/E (b) droop characteristics.

By droop regulation the primary control achieves the required power sharing, at the expense of some deviation of frequency and voltage from their rated values. Secondary control – implemented by a higher-level hierarchical entity (e.g., a supervisor unit) – then takes charge sensing the microgrid voltage amplitude and frequency and compensating the deviations.

An interesting review of droop control techniques [50] shows solutions featuring an intermediate control loop in addition to the conventional ones, with voltage and frequency performance improvement of inverters parallel-connected with the AC grid bus.

The droop regulation can be applied also in DC MGs or NGs. Of course, in this case the control operations are different from those required in AC microgrids. While in an AC microgrid two units are required to control frequency and voltage, in a DC microgrid the control is applied to voltage alone. Of course, it follows that the control of AC and DC microgrids must be implemented with different algorithms and approaches. However, the control strategies can share the same classification.

- **Conventional droop control**: it is one of the popular decentralized control strategies [51], adopted to minimize or eliminate the current circulating between converters without a communication link. It also provides good voltage regulation.
- **Virtual-Resistance-based Droop Control**: by inserting a virtual droop resistance that is a function of the voltage at the output of the DC/DC converter connected to the DC bus distributing the electricity to the loads, it is possible to achieve a non-linear droop characteristic improving the voltage regulation compared to the conventional droop control [52].
- **Adaptive Droop Control**: adaptive control does not require in-depth knowledge of the system for control design, unlike conventional and virtual resistance droop techniques. In fact, in this case the control parameters are self-adapted to satisfy both power sharing and DC bus voltage stability criteria [53].

In any case, the droop units execute control algorithms to guarantee system performance and stability.

The main goals of microgrid control can be listed as follows [7]:

- smooth switching from grid-connected mode to islanded mode, and vice versa;
- efficient regulation of voltages and currents in both islanded and grid-connected modes;
- efficient proportional load power-sharing;
- ensure stability with constant power load as well as non-linear ones;
- coordinate DERs, BES and others storage devices included in the system;
- control the power flows in the microgrid and, if grid-connected, with the utility grid;
- synchronize the microgrid with the utility grid;
- prevent grid failures and avoid black starts;
- ensure uninterrupted power supply to critical loads (e.g., hospitals);
- maximize DER potential;
- minimize transmission losses;
- optimize generation cost;
- reduce the cost of load dispatching;

- optimize the microgrid energy production to be competitive in the energy market.

A plethora of microgrid control strategies can be found in the literature. Figure 1.10 shows in a diagram a possible taxonomy of microgrid control techniques [54]. In the next paragraphs we will focus specifically on the classification based on controller function.

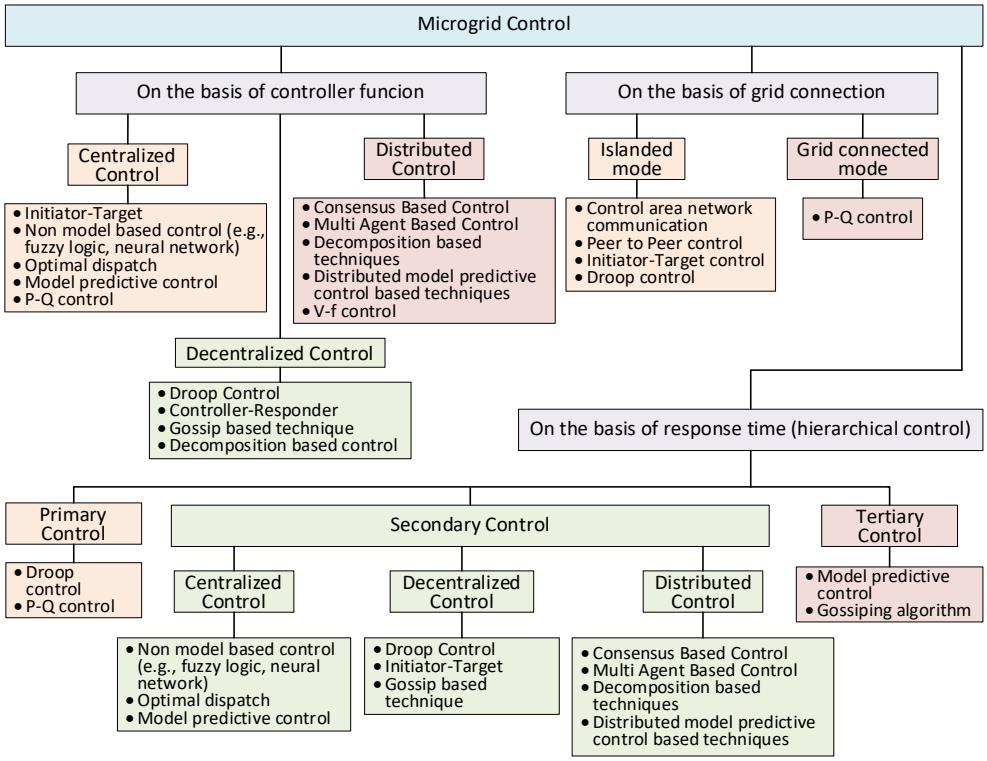

Figure 1.10: Schematic classification of MG/NG control techniques.

1.4.2.1 Centralized Control

In the case of centralized control, the distributed generators of the grid are connected to a control unit such as a microcontroller, or a switch, or a server that provides reference values for primary control. In this technique, a microgrid central controller (MGCC) gathers data from the controlled distributed generators, based on which it performs calculations to determine the control actions necessary to properly manage

the power flows in the microgrid [55]. A schematic diagram of a microgrid with this type of control is shown in Figure 1.11. Hierarchically, a device controller operates at the primary control level.

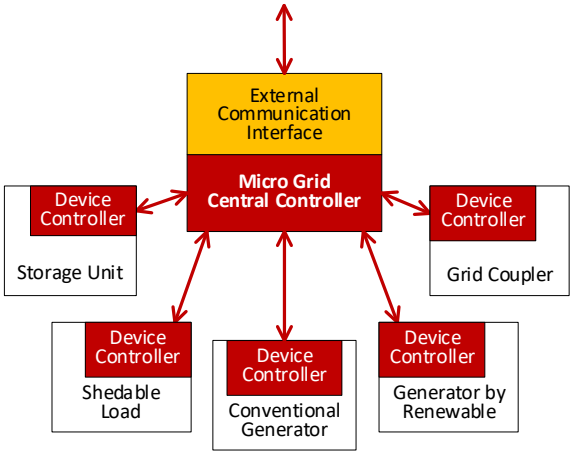

Figure 1.11: Schematic diagram of a microgrid with centralized control.

The control commands need to be transferred to the peripheral units via an appropriate communication medium. The strong reliance on high-speed communication between the MGCC and its monitored and controlled units is the main disadvantage of this method, because any communication fault will affect the performance of the whole microgrid and may even result in complete black-out. Beside poor fault tolerance capability, the major drawbacks of this control method include the need for supervisory control, and low scalability. Among the advantages of the centralized controller are the effective controllability of the whole system, the need for a single controller, and the possibility to define general strategies for monitoring and controlling the system.

In DC microgrids, the central control is typically implemented with the master-slave architecture shown in Figure 1.12 for managing parallel operation of multiple distributed sources [56]. In this case, a converter operates as master voltage source converter controlling slave units feeding the required current as ordered by the master controller.

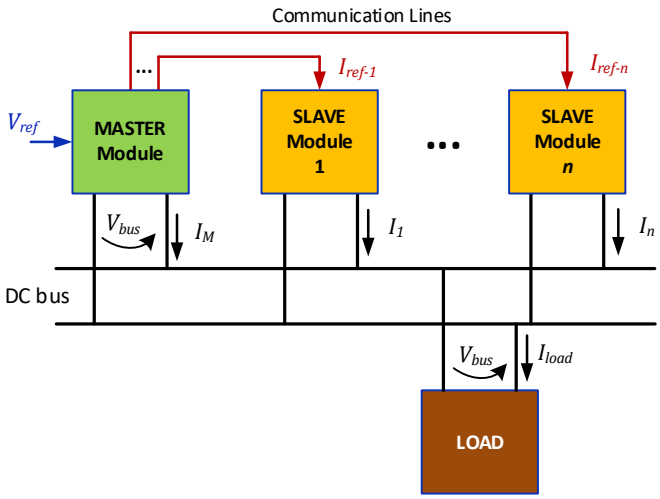

Figure 1.12: Scheme of a Master-Slave architecture for centralized control of a MG.

Problems related to specific converters can be solved with different methods. For example, PWM controlled DC/DC step-up converters can usually regulate the output voltage over a small range, and works have been published aiming to solve or mitigate this problem. As an example, authors in ref. [57] showed the results obtained using a master-slave approach with phase-shift control for an input-series and output-parallel full-bridge converter. Features like flexibility and simple implementation make it suitable for high power and high voltage grids.

In [58], an improved master-slave control strategy based on I-ΔV droop addresses the problem of smooth transition between grid-connected and islanded modes. Here, when the microgrid is grid-connected, the energy storage converter operates as a slave controlling the current as in conventional master-slave control, while during island detection and islanding it smoothly transitions to voltage control with a droop approach.

1.4.2.2 Decentralized control

In a decentralized architecture primary and secondary level controls are implemented in microgrid units above the converter controls. Different topologies can be found in the literature, with (Figure 1.13a) or without (Figure 1.13b) an MGCC controlling distributed generators (DG) as proposed in [59].

The decentralized control strategy is considered the most reliable, but there are limitations due to the absence or to the reduced band of communication links.

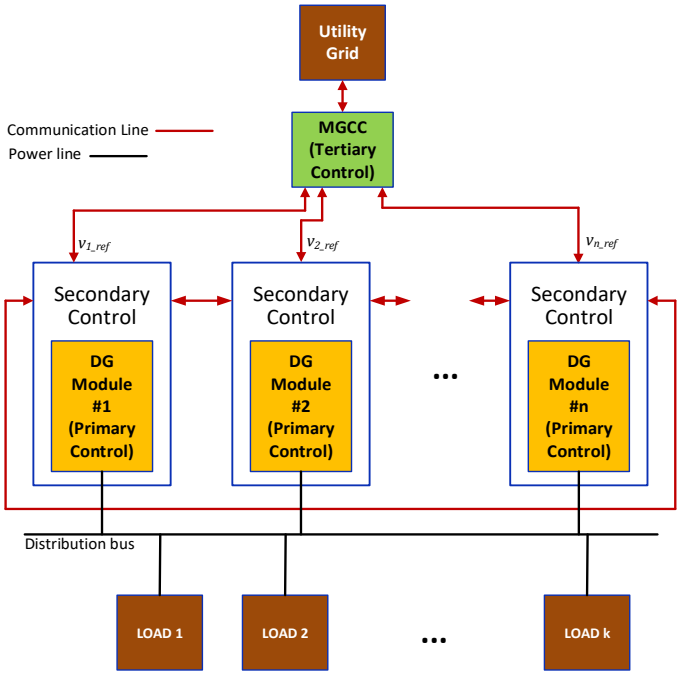

(a)

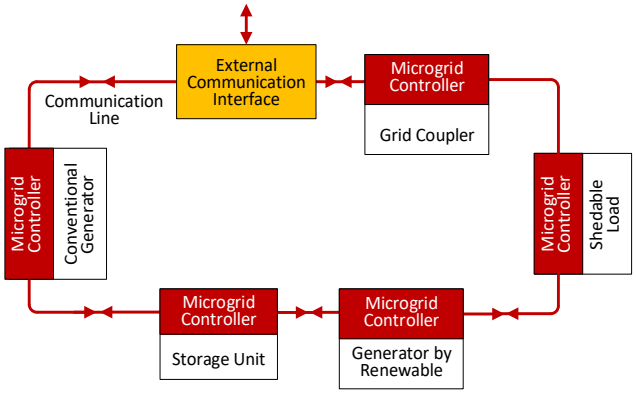

(b)

Figure 1.13: MG decentralized control architectures with (a) or without (b) an MGCC.

1.4.2.3 Distributed Control

In this case, the controllers of each power electronic unit are connected to a network to form a distributed secondary control mainly aimed at maintaining proper load sharing and steady grid voltage. This approach has the advantages of both centralized and decentralized control architectures.

Figure 1.14 shows a diagram of a distributed control architecture [60]. Here, each unit uses local variables, as voltage and frequency, exchanged with its neighbors. The communication link is bidirectional to allow global optimization as in a centralized scheme.

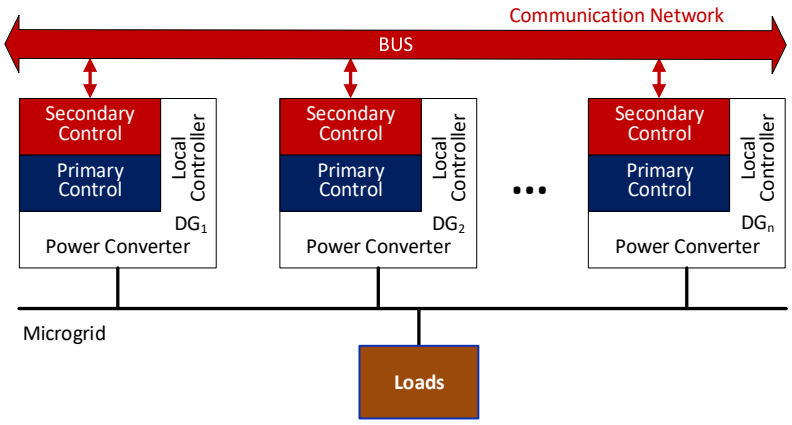

Figure 1.14: Diagram of a distributed control architecture.

Compared with architectures using single centralized control, this solution reduces the risk of global system failure since the system is immune to one-point failures. It also provides good stability along with reduced communication cost. Moreover, distributed control is highly scalable (significant increase in DG units makes it quite difficult to up-scale a centralized control system).

The main problems include voltage and frequency restorations, and power-sharing improvements [61].

The techniques used for a distributed secondary control are different. For example [62], [63]:

- Multi-agent system;
- Consensus-based technique;

- Decomposition-based techniques;
- Distributed model predictive control-based techniques.

1.5 State of the art on simulations

As analyzed in the previous chapter, the traditional power generation and distribution systems will be supplanted by the SG concept and framework which will transform the way the legacy power grid has been traditionally designed and managed. The plethora of actors involved in this process, including intermittent and variable generation from RES, mobile loads, and storage, such as EVs and the need of plug-and-play functionalities, will increase the uncertainty and complexity of the energy management system [64]. Consequently, this complexity accelerates the need to identify the appropriate computational tools to perform designing and sizing actions in this future SG context.

However, there is a plethora of black-box simulation tools in this area, which challenges the network designer and operators to find an appropriate tool based on their objectives and on the kind, size, and topology of the grid. In general, this simulation software allows the user to define the number, the size and the nominal parameters of the model of each component of the network. After running the simulation, they provide results including the optimal size of each component of the system and provide detailed information about energy flows among various components. Some, additionally compute statistics about carbon footprint and financial/cost analysis.

Several tools are conceived to help transmission network operators to model and analyze power generation systems or power transmission and distribution systems. Authors in [65] give a comprehensive review of these tools, alongside to short-circuit and power-quality and stability analysis tools. Many other black-box tools are designed to cope with modelling complete energy systems including generation (also from RES), storage and typical load consumption profiles. A complete review of these tools is given in [66]. In addition, ref. [67] gives a more refined review and comparative analysis restricted to 19 simulation tools for hybrid renewable energy systems.

If we shift the focus from black-box (always offline) systems towards the tools used in research for the design, sizing, and optimization of developed prototypes, as well as tools employed in online systems, including Hardware-In-The-Loop (HIL) or Supervisory Control and Data Acquisition (SCADA) facilities, simulation tools can be classified in two main categories: *offline* and *real-time* [68], [69].

Most of the power system simulators are *offline*, namely, they run the simulation on a standard processor (e.g., a personal computer or workstation) and provide the results in an output file or on the screen. They do not interact with any external equipment, and they operate on local available datasets and information: everything that needs to be included in the simulation is modeled within the simulator. In case it is necessary to increase the total computational power, or when we need to split the model among different specialized simulation platforms, one or more parts of the system can be modeled and run on different platforms, externally interconnected by means of proper interfaces and communication protocols. This is called a *co-simulation*, but it is still an offline simulation paradigm. The main characteristic of the offline simulation is that it does not have to coordinate its simulation speed with any real-time event. Almost all power-flow and transient stability simulators are considered offline simulators, as well as Electromagnetic Transient (EMT) simulators. In off-line simulations, the speed of the simulation can be faster (or much faster) or slower (or much slower) than the real-time evolution of a phenomenon. Therefore, in some cases offline simulations are convenient compared to real-time ones in case the computation can be executed faster; vice versa, there are cases when a slow-executing model can perform better if run on a real-time specialized simulator, even when it does not require to interact with real-world equipment.

Real-time simulators perform instantaneous time domain simulations running in hard real-time using dedicated, purpose-built, high performance, multicore, multi-processor computing platforms with real-time/low-latency input/output interface capabilities. While their simulation results are the same as off-line simulation, their real-time nature and I/O capabilities allow them to connect to external equipment (automation and control as well as, in some cases, power equipment) for closed loop testing, which is called HIL simulation.

A special application of the real-time simulation paradigm is the case where a simulator interacts, controls and exchange live data and signals with an online real-world physical system or network. In this case it is called *online* simulation.

These simulators can help with the decision-making process in system control: it is the case of SCADA systems.

1.5.1 Model-based Design

Model-based design (MBD) is a mathematical and visual method of addressing the problems associated with designing complex control systems and is being used successfully in many motion control, industrial equipment, aerospace, automotive, and power electronics applications. It provides an efficient approach for the four key elements of the development process cycle, namely:

1st modeling a plant (system identification),
2nd analyzing and synthesizing a controller for the plant,
3rd simulating the plant and controller,
4th deploying the controller.

This allows to integrate all these phases and to provide a common framework throughout the entire design process.

This MBD paradigm is significantly different from the traditional design methodology. Rather than using complex structures and extensive software code, designers can now define advanced functional characteristics using continuous time and discrete-time building blocks. These models, along with some simulation tools, can lead to rapid prototyping, virtual functional verification, software testing, and validation. MBD is a process that enables faster, more cost-effective development of dynamic systems, including control systems, signal processing, and communications systems. In MBD, a system model is at the center of the development process, from requirements development, through design, implementation, and testing. The control algorithm model is a specification that is continually refined throughout the development process [68].

The MBD framework workflow consists of four steps as outlined in Figure 1.15. The first step is called Model-in-the-Loop (MIL), Figure 1.16: it consists in an offline simulation where neither the controller, nor the plant, operates in real-time. At this step engineers can study the performance of the system and design the control algorithms in a virtual environment, by running computer simulations of the complete system or subsystem.

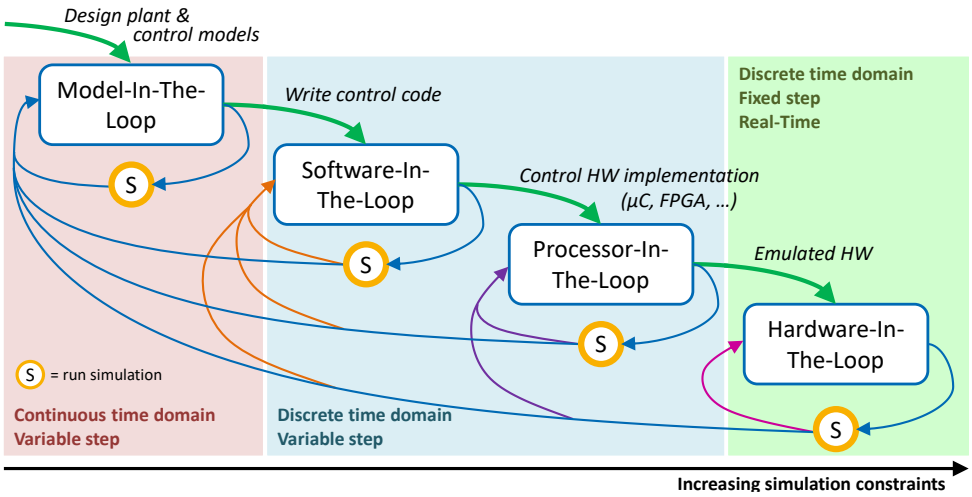

Figure 1.15: MBD simulations. Workflow: from MIL to HIL.

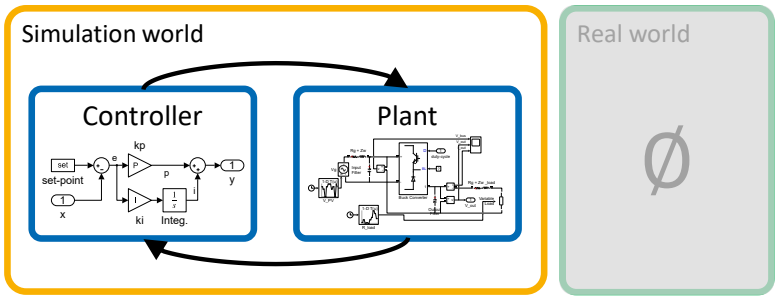

Figure 1.16: MIL: setup of the offline simulation model of the system.

The second phase is SIL, Figure 1.17. Here the control section of the model is re-written or converted into code (e.g., C/C++) and inserted in the model by means of *S-functions* (system-functions). *S-functions* allow to define how a subsystem works during different phases of the simulation, such as initialization, update, derivatives, outputs, and termination. In every step of a simulation, a method is invoked by the simulation engine to fulfill a specific task [70]. This allows to lower the level of abstraction, getting closer to the real implementation.

A step further consists in deploying the control code on a real (embedded) device, like a microcontroller, a DSP, an FPGA, etc., as shown schematically in Figure

1.18. This third phase is called Processor-in-the-Loop (PIL). The control device then needs, to communicate with the simulation environment by means of standard interfaces and protocols like JTAG (e.g., over USB), TCP or UDP over Ethernet, etc. In this way, the processor is provided with virtual signals coming from the simulated plant, it can process them, and it produces control outputs which are sent back to the model of the plant, closing the loop. This phase allows the designers to test the performance of the processing unit and to revise the code, to optimize the whole execution. It is important to note that, at this stage, the controller is not exchanging any signals with the real world, therefore no hardware interface peripherals are used yet.

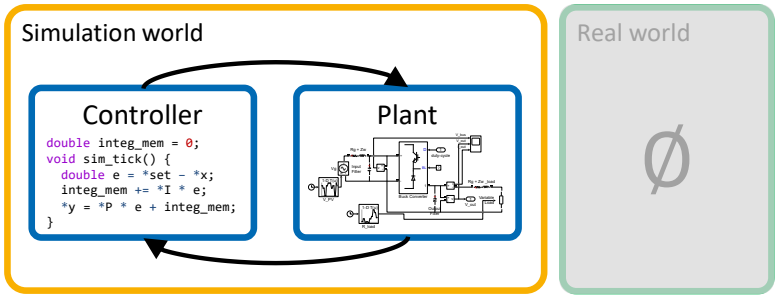

Figure 1.17: SIL: the control logic is compiled into executable code.

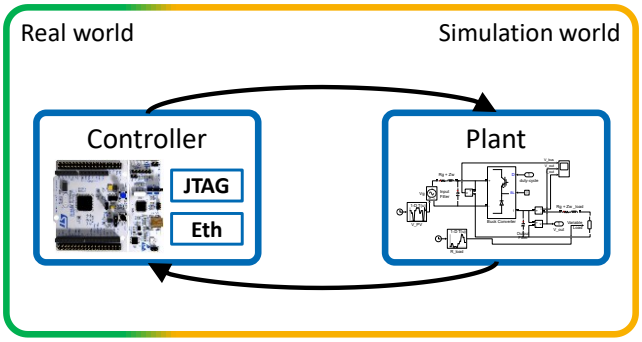

Figure 1.18: PIL: the control code is deployed to an embedded device and interfaced with the simulated plant through a data communication line.

The last step is HIL. As shown in Figure 1.19, it is a technique for combining a simulation model of a system with actual physical control hardware, such that the hardware performs as though it were integrated into the real system. The hardware

controller and associated software are connected to a mathematical simulation of the system plant, which is executed on a dedicated simulator in real-time. To connect the real-time model to the hardware controller, the simulator is equipped with specialized hardware enabling it to receive electrical signals from the controller, as actuator commands to drive the plant, and it converts these signals into the physical variables connected to the plant model. After that, the plant model calculates the physical variables that represent the outputs of the plant, these values are converted into electrical signals (that represent the voltages produced by the sensors) and they are fed to the controller inputs. Here, also the physical I/O capabilities (both digital, analog, and specialized peripherals e.g., PWM generation) of the controller are involved and tested.

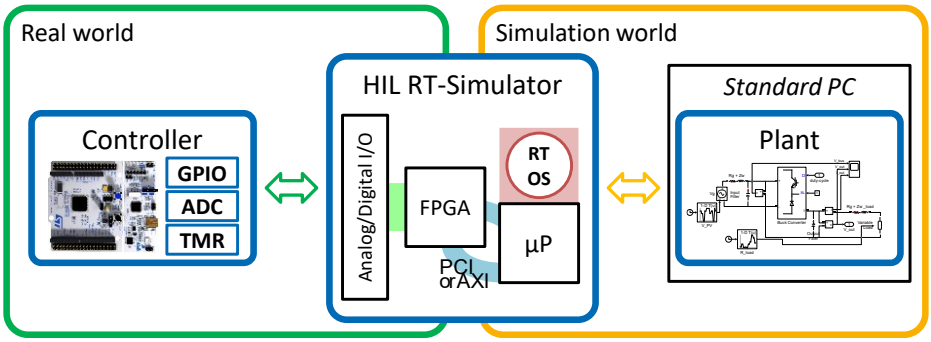

Figure 1.19: HIL: the embedded controller is interfaced with a specialized simulator, exchanging physical signals.

Moving the focus from the controller to the plant, the HIL paradigm can be reversed, namely, the control section and, optionally, a section of the plant, are simulated by a real-time software and interfaced with a physical implementation of the plant (or the remaining part of it) as in Figure 1.20. In this case it is referred to as power-HIL (p-HIL) – while the previous case is sometimes called control-HIL (c-HIL). In this case, too, it is necessary to have a specialized simulation platform, equipped, in addition, with ad-hoc interfaces that allow the exchange of power signals with the physical system.

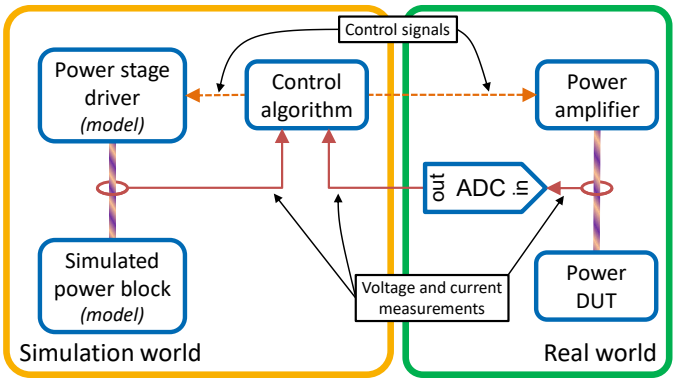

Figure 1.20: p-HIL: the plant (or a part of it) is setup in the real world and interfaced with a speialized simulator able to echange both control and power signals.

1.5.2 Digital Twins and SCADA in Smart Grids

During the last decade, the rapid diffusion of the HIL (especially p-HIL) paradigm led to the possibility of exploring a new world where real-time simulation models are paired and interact directly with on-field technologies and systems. This paved the way for the diffusion of the concept of Digital Twin (DT) and of SCADA systems within smart grids. Furthermore, these technologies are receiving a strong boost in the context where online monitoring, flexibility in operation, better inventory, management, and personalization of services are the most promising market pulls, and where availability of cheap sensors and communication technologies, together with the widespread diffusion of artificial intelligence, cloud and edge computing are the major technology push [71].

A DT is a detailed virtual representation of a physical system. According to the literature, the DT approach should contain three major components: the physical system (physical twin), the virtual model of the system (i.e., the DT itself) and a bidirectional information link in between physical and virtual twins [72]. The two second components can be implemented by means of an HIL system.

When a DT is connected to its physical counterpart, it does not only give real-time information for more sophisticated decision making, but it can also make predictions about how the system will evolve or behave in the future, augmenting

sensor data with synthetic data generated from faster-then-real-time parallel simulations.

The DT approach can achieve three main results:

- fine tuning and validation of the DT model, thanks to data collected in real-time on the field;
- perform offline simulations involving the DT to predict or study the effects of changes to the system (e.g., introduction of new components or parts, change in the size of components, etc.) or to the environment in which the system operates;
- perform online simulations where the DT (or multiple instances of it) runs in real-time (or faster-than-real-time), allowing to make automated decisions in a more informed way, perform data statistics and analysis to detect/predict the equipment status and defects in time [73], and, finally, allowing human interaction and monitoring (sometimes called human-in-the-loop) through advanced graphical user interfaces (see Figure 1.21).

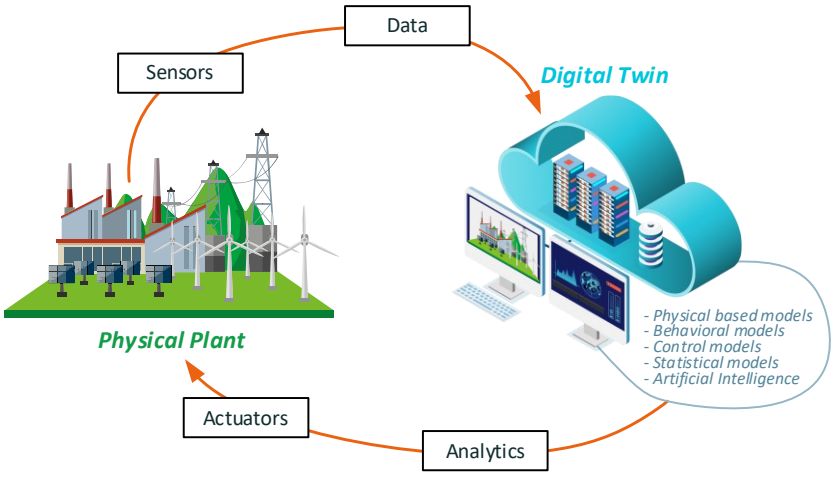

Figure 1.21: Diagram of an online DT.

Modeling the behavior of physical systems is the first step towards creating a DT of an asset, however, in the context of the distribution network, the complexities in the present and especially in future scenarios (with high penetration of distributed

RES generation) is significant. Therefore, implementing models by traditional approach, namely, individual modeling of the physics underlying each single component, in a way that they can meet the functional requirements of a DT is not practical or even feasible. This calls for simplified behavioral models, easily (or automatically) tunable with data from the field. The complexity of detailed physical models describing many interconnected dynamic systems also represents a big problem when the target is reaching real-time (or higher) performance.

In particular, in EMT domain simulations the length of the simulation time-steps is strictly related to the switching frequency of the converters, requiring very high temporal resolution, thus lot of solver iterations. This leads to models capable of very fine representation of the system dynamics but simulations running much slower than real-time. Therefore, this kind of models are very useful, thanks to their level of detail, in designing single components of a system (e.g., power converters, device-level control algorithms, etc.), but they can represent an unacceptable overhead in system-level (grid-level) simulations. A way to overcome this is designing behavioral models in phasor-domain simulations. To summarize the concept, in Figure 1.22 the DT approach capabilities are drawn in a virtual model-fidelity/simulation-speed space.

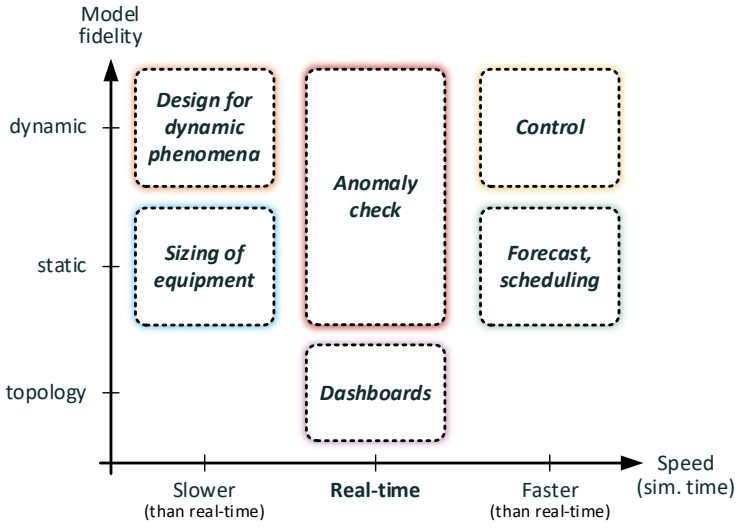

Figure 1.22: Correlation between simulation-speed and model-fidelity considering different DT deliverables.

In the power systems area, online DTs represent the natural evolution for SCADA systems, allowing to build the control centers for the future SG [74].

According to [75], SCADA systems are defined as a collection of equipment that will provide a remote operator with sufficient information to determine the status of a particular piece of equipment or a process, and take actions regarding that equipment or process without being physically present. The terminology SCADA is generally used when the process to be controlled is spread over a wide geographic area, like power systems. To date, the majority of DSO employ SCADA technologies to manage the distribution network with different functions at different levels of the system (Figure 1.23), including centralized and distributed power generation plants. SCADA involves three major activities:

- data acquisition from the field,
- monitoring and supervisory control of the plant,
- automated (or manual) decision making and actuation.

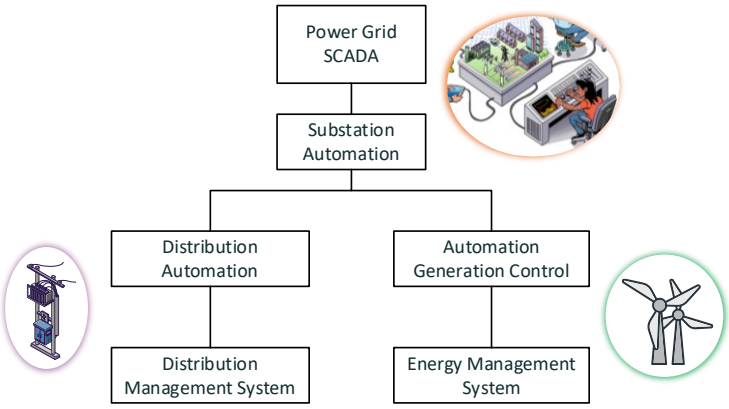

Figure 1.23: SCADA applications in power systems.

Historical data analysis is another important function performed by the power system SCADA, where the post-event analysis is done using the data available after the event has happened (e.g., the post-outage analysis where the data acquired by the SCADA system can provide insights into the sequence of events during the outage). The insertion of a DT of the system within the SCADA systems enables estimations of the short-term evolution of signals in the network, and to test in advance the outcome of actions that can be taken in an automated manner.

1.6 Contributions of the thesis

The main contribution of this thesis is to provide a library of behavioral models for top-level simulations of SGs. Secondly, a building thermal model is integrated with electrical models in order to obtain a comprehensive energy model. As we will show in simulation results, the goal of the given approach is to obtain information about the evolution of the system in terms of energy and power exchange between the actors of the grid, the state of the main components (storage systems, loads activation and scaling, PV production, fault detection and islanded operation…), voltages and currents values in phasor domain. A further important advantage is given by the fact that this kind of models allows simulations to be carried out on a large time scale (in the order of months to years) with a particularly low ratio between the simulated time span and the computation time: less than 0.15% using standard CPUs in the case of the models presented in the following chapters. As detailed in the previous paragraphs, this aspect is of particular importance when you need to perform real-time or faster than real-time simulations (e.g., in DT applications or in predicting/estimating the evolution of a system). These execution times are orders of magnitude lower than those generally required by simulations in the EMT domain where detailed electrical or physical models are employed. In the latter case, in fact, the simulation execution speed is much lower than the real-time as the maximum simulation time step is bound to the physical dynamics of the electronic components and/or to the maximum operating frequency of the switching components [76].

The behavioral approach allows to make system-level considerations about the introduction and sizing of new grid components considering many aspects, from the electrical one to the economic balance, the environmental benefits, etc.

Chapter 2

University of Parma South Campus Grid Model

The smart MG paradigm is one of the key elements in the process of accommodating the penetration of DERs at the distribution level. The diffusion of erratic, non-dispatchable DERs makes distributed autonomous control a necessary complement of standard control strategies conceived for one-directional energy flows that are destined to be displaced by much more complex and less predictable bidirectional flow patterns. Besides, the aggregation of DERs, Battery Energy Storage Systems (BESSs), and loads, in potentially autonomous clusters such as Micro- or Nano-Grids fosters efficiency, sustainability and grid resilience. Smart energy MGs are therefore key ingredients of the recipe for Smart Cities [77].

University campuses are natural playgrounds for the development of MG concepts, thanks to the ideal scale and a dynamic environment from both intellectual and real-estate development points of view [78]–[86].

Authors in [78] present an energy management algorithm for the optimal dispatching applied to the case of the Savona Campus Smart Polygeneration Microgrid, considering Combined Heat and Power (CHP) units, boilers, electrical storage, and electric loads. In [79], the same facility is employed as a test bed for studying the effects of the PV penetration on the campus grid from an economical point of view. Paper [80] present a design proposal for the future implementation of a microgrid in the University Campus of UNICAMP in Brazil: a description of the state-of-the-art

of the microgrid is given and the introduction of new components is discussed. Ref. [81] describes the University of New Mexico grid and argues about the introduction of a communication system infrastructure to interact with the outside world to regulate the internal energy consumption according to energy availability. In [82], the introduction of a commercial SCADA system into the Federal University of Ceará campus grid is described. The aim is to improve the quality of service by increasing the reliability and security of the power distribution system. Authors in [83], present the case of study of the Trieste University Campus: a power flow simulation model is designed, and the introduction of smart meters and actuators is discussed, giving preliminary experimental results. In [84] the National Laboratory of Smart Grids of the University of Colombia is described. In particular, the design of a multi-layer reference model is discussed, and a commercial data management and data-driven decision-making platform is chosen to fulfill all the functions and objectives of the framework. Authors in [85] present the case of the Saudi Arabia University Campus where energy metering and management systems are installed in many of the facilities' buildings. An automated control system is set up to schedule lights and air handling units resulting in a 14.3% reduction in energy consumption. Finally, in ref. [86] the development of a DT of the National Autonomous University of Mexico smart grid is presented. The DT is obtained by combining two commercial systems, namely, a SCADA platform and a power systems simulator. The DT is employed in integrating new renewable energy sources linked to balance increasing load demand, analyzing power outages and energy quality, studying the integration of electric vehicles, etc…

The University of Parma South Campus (UPSC) hosts 4 departments and 10 research centers covering a wide spectrum of scientific and technological disciplines, together with recreational and sports facilities, cafeterias, etc. The number of students, faculty and staff is in the range of ten thousand. The installation of 677 kWp of photovoltaic (PV) power generation and ten charging stations for electric vehicles (EVs) marked the beginning of a process that should see, in the next few years, upscaling of PV generation capability, BESS deployment, and installation of a metering network to monitor and control the energy grids (electrical and thermal). The electric MG will be integrated with the thermal grid [87], [88] into a smart energy grid for optimized performance and efficiency.

Detailed modeling of the key elements of the energy infrastructure and of the MG as a whole is a necessary step in this process: first, as a design and planning tool; in the second stage, as the backbone of the MG control system. This chapter describes the development of a MATLAB-based campus MG DT and its use to investigate possible scenarios of PV generation and BESS deployment in combination with EV charging stations [89]. In particular, a library of models for the components of a campus MG is presented including:

- a model for the PV plants with MPPT control algorithm;
- a model for the BESS for grid-connected and islanded operation modes;
- a detailed model of the heat-pump-based heating/cooling system of a campus building, coupling the dynamic thermal model with the electric grid model; this kind of comprehensive energy grid modeling will likely gain importance in the near future as the concept of integrated energy districts and their modeling become more common;
- outdoor lighting load modeling;
- active power/frequency (P-f) droop characteristics for the estimation of MG frequency variations in islanded mode.

It is worth pointing out that at the present stage the model is not intended to serve MG control purposes [90], [91], load flow or stability analysis; rather, it is aimed at giving a physical description of the main components of the electric MG as a guide to development planning [92]–[95].

2.1 Modeling Approach

The UPSC MG DT is built in MATLAB-Simulink environment. Because the aim is to study the evolution of the grid towards increased smartness, it is necessary to evaluate its economic and environmental sustainability over long periods of time, which calls for simulating time windows of at least a year. Therefore, simplifications are required in order to reduce the computational load and make simulations much faster than real-time. A discrete-time three-phase phasor-domain simulation [96] method is adopted, which implies, in particular, that the frequency is considered to be constant (a few considerations about the inclusion of frequency variations are

given in 2.4). The model is developed in the *Simscape Electrical Specialized Power Systems* environment.

An ideal voltage generator represents the connection with the national power grid (NPG), which is currently the main source of energy for the UPSC. From this Point of Common Coupling (PCC), the internal grid is organized in a tree-like structure with additional loops serving buildings of recent construction and for emergency and backup purposes. Each node of the tree is equipped with a transformation cabinet. Transformers, transferring power from medium voltage to low voltage utilities, are modelled by the Simscape block *Three phase transformer (Three windings)*. Medium voltage (MV) distribution lines have no neutral reference, whereas low voltage power is distributed with the additional neutral wire. Each distribution cable is modelled by the block *Distributed Parameters Line* with per-unit-length values of resistance, inductance, and capacitance specific for the UPSC case. End-side utilities consist of buildings or building compounds. In total, the model currently includes 18 facilities, including classrooms, scientific laboratories, offices, sport facilities (with outdoor and indoor facilities and swimming pools), canteens and cafeterias. A schematic diagram of the UPSC MG is shown in Figure 2.1.

2.2 The Campus Grid Model

In this section the MATLAB/Simulink models of the components of the MG DT are described. Loads include generic campus buildings, a detailed model of a building heating/cooling system, and outdoor lighting loads. Loads are modeled as current sinks, with active power absorption profiles described in the paragraph 0. Reactive power absorption is considered based on a constant load angle that characterizes the individual loads. Generation is currently limited to PV (paragraph 2.2.4), and storage to battery banks (paragraph 2.2.5); a battery like model is also used for the EV charging stations (paragraph 2.2.6).

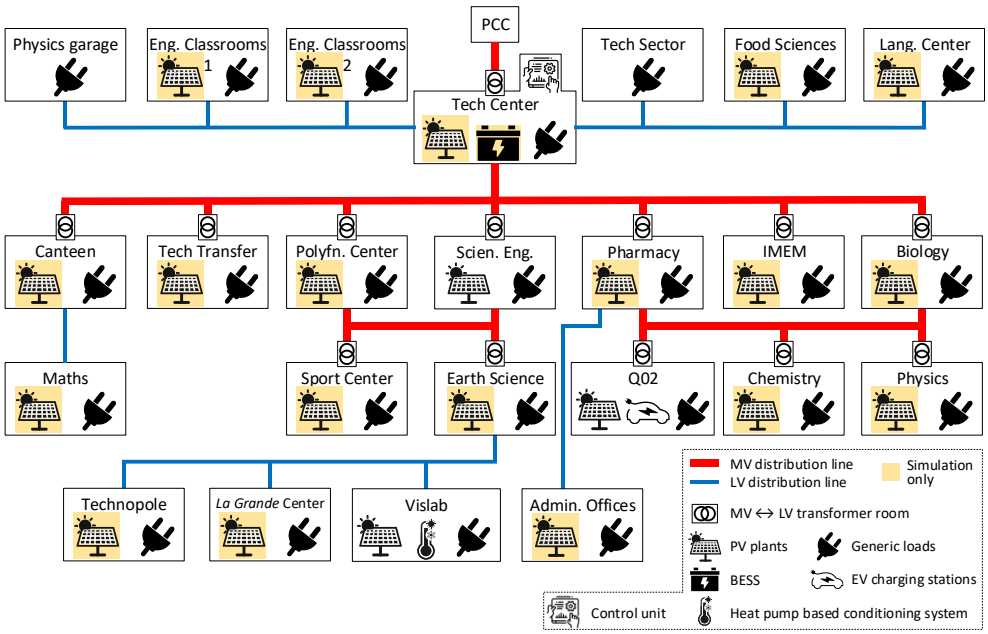

Figure 2.1: Schematic diagram of the UPSC grid model.

2.2.1 Generic Building Modeling

Loads are modeled considering weekly power consumption profiles. The UPSC grid development plan includes the deployment of a network of smart metering devices for consumption monitoring. However, to date, the only available data comes from legacy metering devices recording the monthly consumption of selected buildings and of the whole campus. Thus, our consumption profiles are built based on reasonable scaling of the available measured profiles. In the case of office buildings, realistic power consumption profiles based on a measurement campaign performed on a representative building are built, upscaling or downscaling figures depending on the building area and population. In particular, the weekly consumption profile of a representative building is measured at three different times of the year: (1) winter (average of a few weeks from December to February); (2) spring (end of April) (Figure 2.2); (3) early summer (mid-June). These sample profiles are then scaled according

to the monthly energy consumption of the whole UPSC (Figure 2.3); in Figure 2.4 the computed yearly profile for the sample building is plotted, obtained by scaling the measured data of Figure 2.2 according to the overall consumption of Figure 2.3.

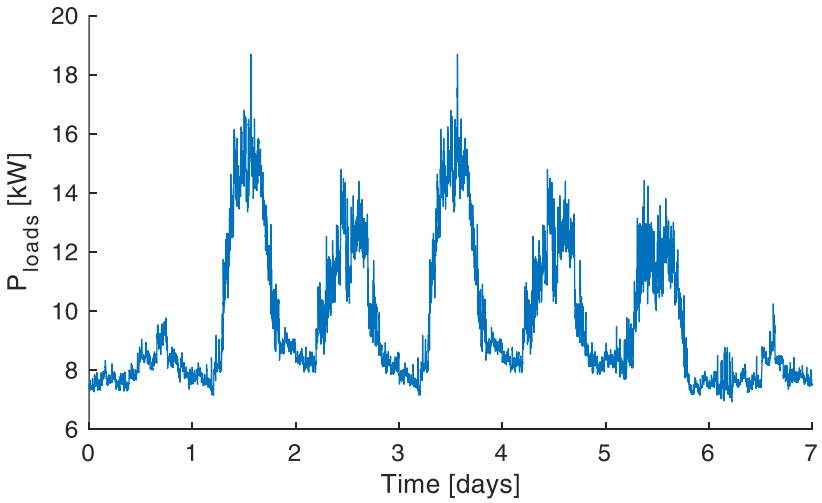

Figure 2.2: Typical weekly load power profile for a sample UPSC building. Data measured in mid-June.

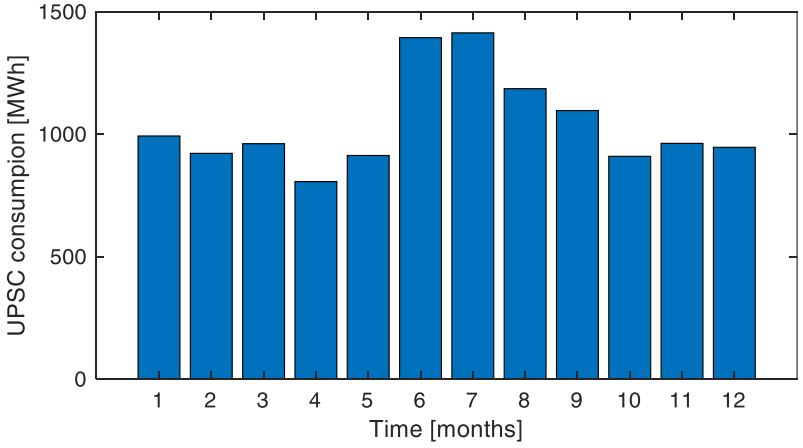

Figure 2.3: Total monthly consumption of the UPSC over a year.

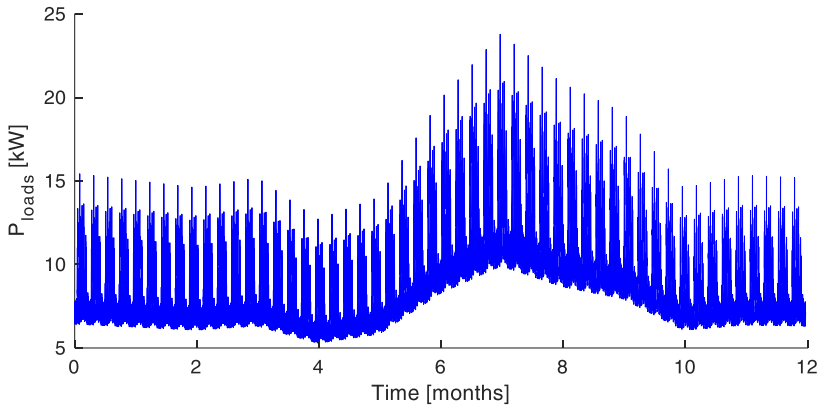

Figure 2.4: Calculated yearly power profile for a sample building.

2.2.2 Building Heating/Cooling System Modeling

The integration of thermal and electrical energy aspects in a single model has not received much attention in the literature. This will likely have to change due to the increasing diffusion of heat pump systems, often fed by rooftop PV. This paragraph shows an example of a combined electrical/thermal model. The UPSC building we modeled (*Vislab* in Figure 2.1) is one of the most recently built in the campus. Unlike the others, it is equipped with its own heat pump heating/cooling system.

To reduce the model complexity, all the rooms are lumped into a single *Building Air Thermal Mass*; likewise, roof, walls, and windows are each represented by a single thermal mass. Figure 2.5 shows the Simulink implementation: the thermal masses describing roof, walls and windows are coupled on one side with the indoor air thermal mass, on the other with the external atmosphere. Heat conduction and convection coefficients are input parameters regulating the heat flow on either side. The outdoor air temperature comes from a measured dataset.

The heating or cooling action performed by the fan coil units is modeled by means of a controlled *Thermal Power Source* that transfers heat from the convector coil to the indoor air mass according to the control signal *Fan Coil Thermal Power*. The convector coil is a pipe wherein flows the thermal fluid coming from the heat pump, with a thermal mass representing its thermal capacitance. The *Fan Coil Thermal Power* is computed based on the fan running state (on/off, speed) and the heat

exchange efficiency of the fan coil. The fan is activated by a hysteresis thermostat featuring four different temperature set points, as shown in Table 2.1, depending on the season (summer cooling, winter heating, or midseason off-state) and working hours, (*normal* operation during working hours and days, quiet operation otherwise: the quiet mode is meant as a compromise between energy saving and the need to keep temperature fluctuations within acceptable bounds).

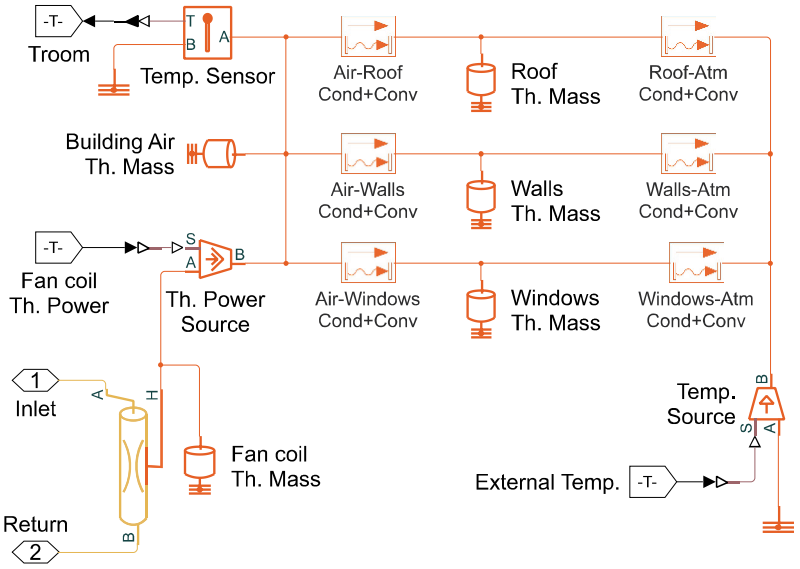

Figure 2.5: Simulink implementation of the thermal model of the *VisLab* building.

Table 2.1: Temperature hysteresis thresholds employed in the thermostat implementation for the activation of the fan coil units.

		Season	
		Summer	**Winter**
Mode	**Normal**	22 ÷ 23 °C	20 ÷ 21 °C
	Quiet	26 ÷ 28 °C	13 ÷ 14 °C

When the fan coil is active, its speed depends on the difference between the room temperature and the thermostat set point, as detailed in Table 2.2 (in *quiet*, the speed is L1).

Table 2.2: Fan speed as a function of the difference between the room temperature and the temperature set point of the thermostat controller.

$\Delta T = T_{room} - T_{set}$	**Fan speed level**
$\Delta T \leq 0.5$ °C	L1 (30% of max speed)
0.5 °C < $\Delta T \leq 1.5$ °C	L2 (70% of max speed)
$\Delta T > 1.5$ °C	L3 (max speed)

The fan state (on/off, speed) is combined with the heat exchange efficiencies shown in Figure 2.6 to yield the *Fan Coil Thermal Power*. *Troom* on the horizontal axes of the charts in Figure 2.6 is not the actual room temperature but an equivalent value that accounts for the variations of both room and fluid temperatures (e.g., in the heating case of Figure 2.6 (top), efficiency decreases as the actual room temperature increases and/or as the fluid temperature decreases; the opposite happens in the cooling case).

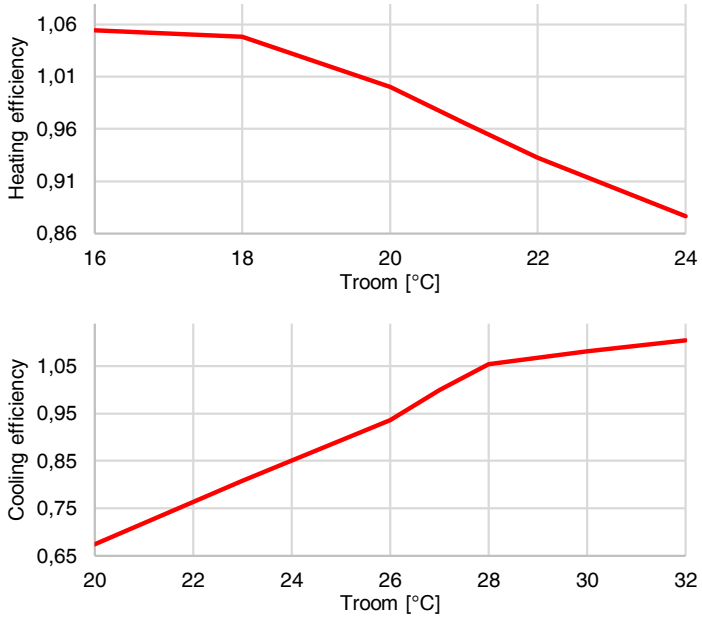

Figure 2.6: Fan coil heat exchange efficiency curves as a function of the room air temperature for heating (nominal temperature: 20 °C) (top), and cooling (nominal temperature: 27 °C) (bottom). The efficiency is defined to be 1 at the nominal temperature. (Data from a manufacturer data sheet.)

The algorithm governing the operation of the fan coil unit model (Figure 2.5) is described by the following set of equations:

$$P_{th} = a \cdot c_s \cdot P_{th_{nom}} \cdot f\left(T_{room_{eq}}\right) \tag{2.1}$$

$$T_{room_{eq}} = T_{room} - \left(T_{liquid} - T_{liquid_{ref}}\right) \tag{2.2}$$

$$P_{el} = b \cdot c_s \cdot P_{el_{nom}} \tag{2.3}$$

$$a = \begin{cases} 1, & s = \text{L3} \\ 0.7, & s = \text{L2} \\ 0.3, & s = \text{L1} \\ 0.05, & s = \text{L0} \end{cases} \quad b = \begin{cases} 1, & s = \text{L3} \\ 0.7, & s = \text{L2} \\ 0.3, & s = \text{L1} \\ 0, & s = \text{L0} \end{cases} \tag{2.4}$$

where:

P_{th}	computed thermal power provided by the fan coil to the indoor air mass;
a	fan thermal exchange capability (non-zero even when off, due to coil-to-air heat exchange);
c_s	binary variable indicating the activation state of the conditioning system (when zero, it means that also the recirculating liquid is stopped);
$P_{th_{nom}}$	nominal thermal power of a fan coil unit (different when heating or cooling);
$f(\bullet)$	non-linear efficiency/room temperature function of a fan coil unit (see Figure 2.6);
$T_{room_{eq}}$	computed equivalent room temperature;
T_{room}	temperature of the air inside the building;
T_{liquid}	temperature of the liquid inside the coil;
$T_{liquid_{ref}}$	reference temperature of the liquid inside the coil (50 °C when heating, 10 °C when cooling);
P_{el}	computed amount of electrical power absorbed by the fan coil unit;
b	similar to a, but applied to the electrical power absorbed by the unit;
$P_{el_{nom}}$	nominal electrical power rating of a unit;
s	fan speed setting (Table 2.2, L0 means that the fan is off).

The maximum instantaneous thermal power that can be provided by the fan coil to the air is computed starting from the nominal power capability $P_{th_{nom}}$ of the fan coil and it is scaled considering the equivalent room temperature $T_{room_{eq}}$ (difference between the temperature of the circulating liquid and the one of the air inside the building) according to the heat exchange efficiency curves (Figure 2.6). The value we obtain is scaled again (a coefficient), proportionally to the fan speed (s). Note that when the fan is turned off, if the temperature of the liquid is different from the room temperature, the power exchange is non null.

Heat exchange efficiency curves (Figure 2.6) given in manufacturer datasheets are computed considering a fixed (nominal) temperature for the circulating liquid ($T_{liquid_{ref}}$). However, in real operational scenarios T_{liquid} varies during time, thus the exchange efficiency of the fan coil also depends on the temperature of the liquid. That is the reason why we introduce equation (2.2) in order to estimate an equivalent room temperature to be employed with datasheet efficiency curves.

The electrical consumption of the fan coil, due to the motor driving the fan, is computed by scaling (b factor) the nominal power of the motor $P_{el_{nom}}$ in a way proportional to the selected fan speed (s).

The building subsystem model (Figure 2.5) is coupled with the heat pump unit subsystem model (Figure 2.7), which features:

- a pair of pipes implementing a lumped model of the thermal liquid circuit;
- a water tank, which is the thermal storage of the system;
- two recirculation pumps;
- a heat exchanger, whereby the thermal power generated by the heat pump is transferred to the thermal liquid;
- a controlled thermal power source connected to the heat exchanger, representing the thermal pump heating action;
- a temperature source for outdoor temperature reference.

The implementation of Figure 2.7 consists of two thermal liquid circuits, each with its own *Circulating Pump*. The *Circulating Pump 1* pumps water from the tank through a heat exchanger where the water is heated up or cooled down by the heat pump (*Power Source*), before flowing back into the tank. The heat exchanger is also

coupled with the ambient temperature (*Tamb Source*) to emulate the system thermal losses. The second circuit, driven by the *Circulating Pump 2* pumps water from the tank through the pipeline that supplies the fan coil unit. The amount of thermal power provided to the water by the heat pump is proportional to the difference between the water temperature set point and the actual value of the temperature of the liquid in the tank. The control logic uses different temperature set-point ranges depending on the time of the day and on the working days' calendar, according to Table 2.3.

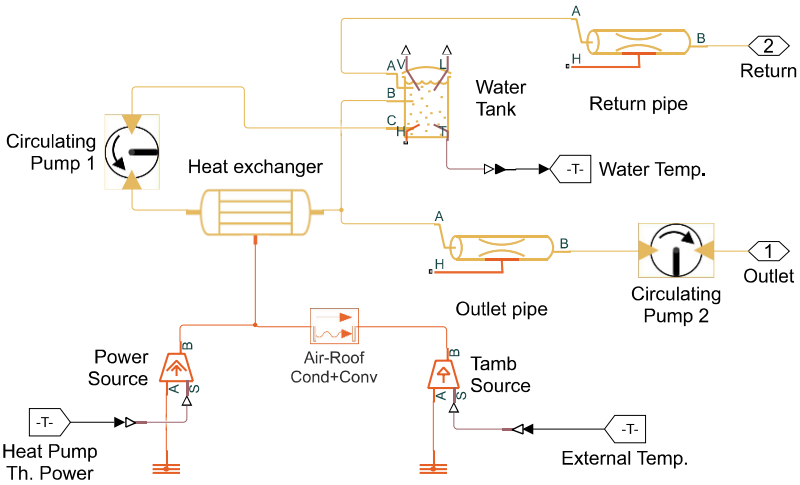

Figure 2.7: Model of the heat pump unit with the water tank, the heat exchanger and the circulating pumps.

Table 2.3: Water temperature range thresholds employed in the control of the heat pump unit.

		Season	
		Summer	**Winter**
Mode	**Normal**	10 ÷ 18 °C	40 ÷ 50 °C
	Quiet	16 ÷ 20 °C	38 ÷ 42 °C

The time dependence of the electric power consumption of the heating/cooling system, displayed in Figure 2.8 for a sample week in January, shows the daily early morning peaks due to the heating pump restoring the liquid to the *Normal* conditions after the nighttime rest, and the intra-day oscillations due to the on off and step speed

regulation of the fan coil units. The total electric energy consumption for the air conditioning is of about 12 MWh during the first part of the year (heating mode), 3 MWh during the summer period (cooling mode) and 8 MWh during the final part of the year (heating mode), with a global annual consumption of about 23 MWh.

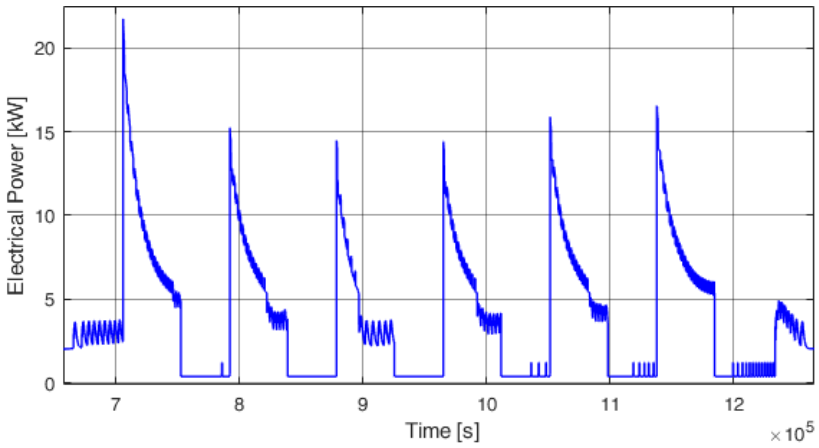

Figure 2.8: Power consumption of the air conditioning system of the *VisLab* building for a week in January.

2.2.3 Outdoor Lighting Modeling

Outdoor lighting is generally estimated to contribute about 15% of the whole urban electric energy consumption [97]. We modeled two outdoor lighting subsystems, one for street lighting, one for the areas surrounding the campus buildings.

The street lighting subsystem allows for simple calculations starting from a given set of parameters, namely:

- illumination level E in lux (luminous flux per unit area);
- coefficient of utilization c_U, the value of which (close to 0.3) depends on the lamp fixture (fixture type, mounting height, length of the mast arm, etc.);
- maintenance factor f_M (generally close to 0.9);
- width of the roadway w_R, in meters [m];
- distance between the luminaries d_L, in meters [m];
- length of the street L_S, in meters [m].

It is possible to obtain the average light radiation flux ϕ_A in Lumen, applying the following formula [98]:

$$\phi_A = \frac{E \cdot w_R \cdot d_L \cdot f_M}{c_U} \tag{2.5}$$

then, the required lamp power in Watt is estimated by using the empirical formula (obtained from interpolation of data [98] coming from various lamp sizes):

$$P_{lamp} = 0.0682 \cdot {\phi_A}^{0.8742} \tag{2.6}$$

Finally, we compute the number of lamps (n_{lamps}) required to cover the entire street length, and the total nominal power (P_{tot}) of the street lighting subsystem:

$$n_{lamps} = \frac{L_S}{d_L} \tag{2.7}$$

$$P_{tot} = P_{lamp} \cdot n_{lamps} \tag{2.8}$$

This nominal (maximum) power is used as a reference value for a scheduling algorithm that accounts for both the natural light level and the time of the day or night, turning lights on when natural light falls below the set threshold (with an appropriate hysteresis value). The illumination level is then regulated by the daily dimming profile in Figure 2.9. For better physical emulation of the electrical behavior, the reactive power absorbed by the lamp drivers is estimated, considering that the power factor is close to one when the dimming level is 100% and it decreases to 0.8 ÷ 0.85 for the lowest dimming levels.

As for the illumination of the outdoor areas surrounding the campus buildings, the mask parameters in input to the block are:

- nominal power of each lighting element (lamp);
- equivalent perimeter of the building (considering only the areas actually illuminated);
- type of lamp (LED or halogen).

The total lamp power is estimated starting from data of a specific installation around a reference building. The same scheduling and dimming profile are used as for street lighting.

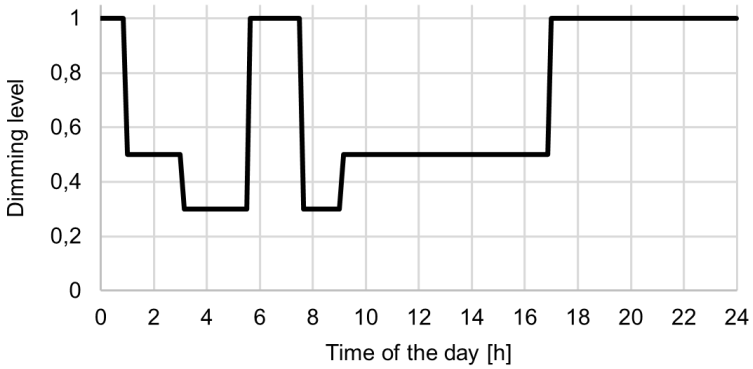

Figure 2.9: Dimming profile used for the outdoor lighting systems.

The UPSC grid model features 5 street lighting subsystems (4 main streets plus 1 for parking areas) for a total nominal power of about 11 kW. For the building external lighting, we instantiate a subsystem for each building, with nominal powers ranging from < 1 kW to > 8 kW, depending on the length of the illuminated perimeter; the total nominal power is 56 kW.

2.2.4 Photovoltaic Plant Modeling

The UPSC currently features a total PV production of 677 kWp; divided into three plants installed on different locations. The largest plant is installed on a building (denoted as Q02) that mostly hosts teaching facilities and consist of two installations: one (270 kWp) on the rooftop, the other (250 kWp) on a solar shelter. The second plant is divided in many installations placed on the rooftops of the engineering buildings; it consists of 7 sub-plants, six of which rated 20 kWp and one rated 10 kWp, for a total of 130 kWp. The third plant is rated 27 kWp and it is located on the roof of the VisLab spin-off facility.

As shown in Figure 2.10, PV plants are modeled as an array of modules in series (N_s) and parallel (N_p) governed by a Maximum Power Point Tracking (MPPT) controller [99]. For the sake of simulation speed, the entire PV array and the MPPT controller are described by mathematical blocks implementing the corresponding equations.

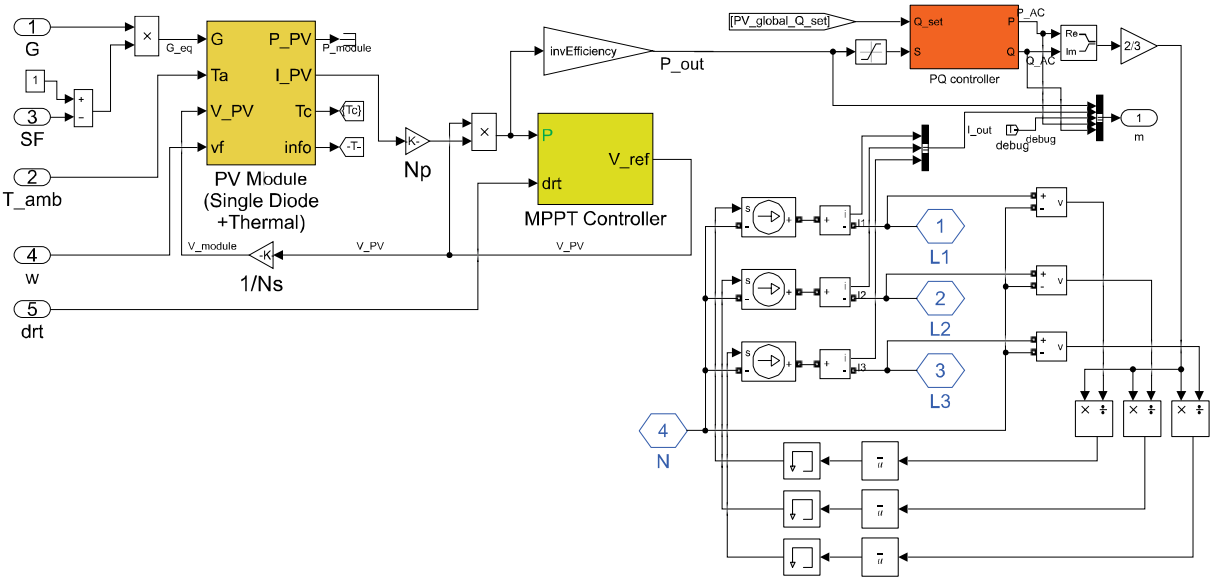

Figure 2.10: PV plant model with MPPT controller.

The PV module (Figure 2.11) is described as series of elementary PV cells and it is modeled by the 1-diode equations [100], [101] supplemented by a static thermal model [102] that computes the cell temperature starting from ambient temperature and wind speed profiles. The equations of the 1-diode model are combined in order to obtain a block able to compute the current output of a module based on ambient data (namely, irradiance and cell temperature), the voltage across the module and the current at the previous simulation step. This choice allows to simplify the mathematical solution that would otherwise require numerical inversion of an exponential expression. All the equations are inserted by means of a *MATLAB function* block.

The implementation of the PV module model is graphically summarized in Figure 2.12, where:

- V_{mod} and I_{mod} are, respectively, the voltage across the module and the current generated by it,
- G and G_{ref} are the input irradiance and the one at Standard Test Conditions (STC) [103],
- T_c and T_r are the input cell temperature and the one at STC,

- $\mu_{V_{OC}}$ and $\mu_{I_{SC}}$ are the temperature dependency factors respectively for the open-circuit voltage and the short-circuit current,
- I_L is the photogenerated current, while $I_{L_{ref}}$ is the one at STC,
- I_d is built-in diode current,
- R_{sh} and R_s are, respectively, the parallel and series resistance of the module,
- n_s is the number of cells in series in the module,
- γ is the ideality factor of the cell,
- q nad k are physical constants, namely, the elementary charge ($q = 1.6 \cdot 10^{-19}\ C$) and the Boltzmann constant ($k = 1.38 \cdot 10^{-23}\ J \cdot K^{-1}$),
- I_0 is the reverse saturation current, while $I_{0_{ref}}$ is the saturation current at STC.

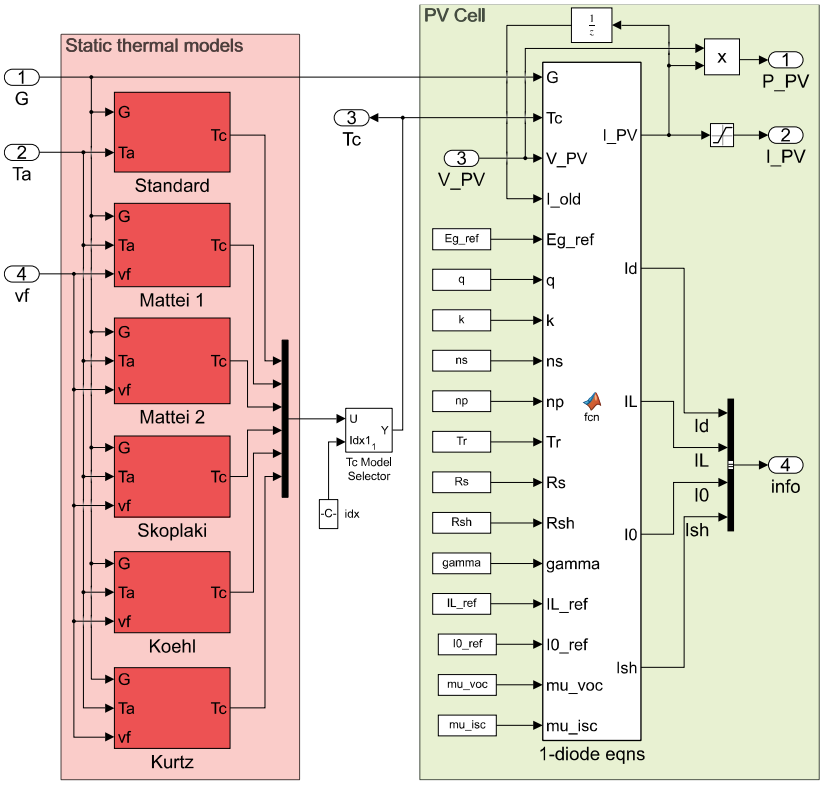

Figure 2.11: PV module model (*Single Diode + Thermal*).

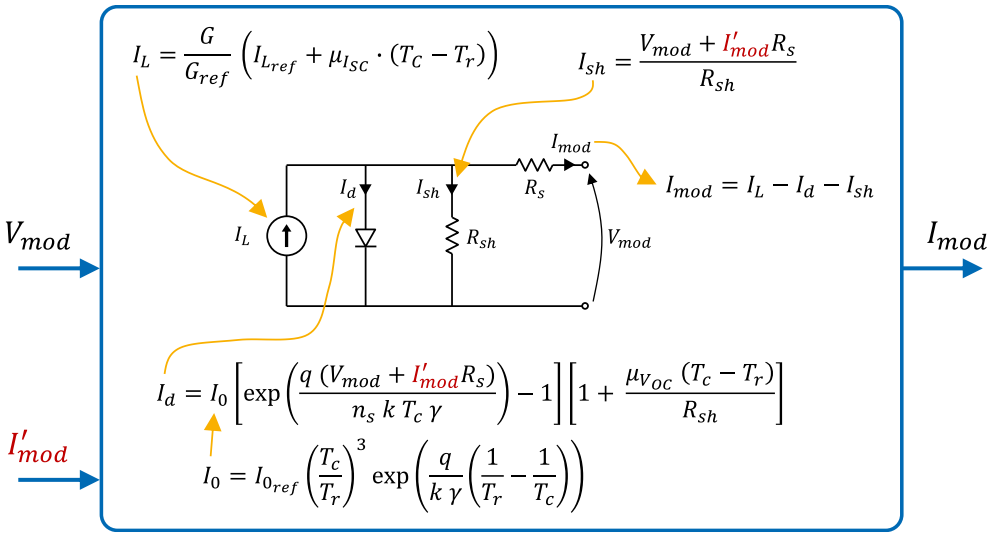

Figure 2.12: Graphical representation of the 1-diode model for the PV module.

The PV module model is designed to automatically tune the equations' constants (R_{sh}, R_s, γ, $I_{0_{ref}}$, $I_{L_{ref}}$) in the model initialization phase (after the compilation and before starting the simulation loop) starting from common datasheet parameters, namely:

- V_{MPP}, the voltage at the maximum power point (MPP) at STC;
- I_{MPP}, the current at the MPP at STC;
- V_{OC}, the open circuit voltage at STC;
- I_{SC}, the short circuit current at STC;
- the number of cells in the module, n_s;
- the temperature dependency factors, $\mu_{V_{OC}}$ and $\mu_{I_{SC}}$.

The tuning of the constants is performed by evaluating, in the order, the following set of expressions:

$$I_{L_{ref}} \cong I_{SC} \tag{2.9}$$

$$R_{sh} = \frac{V_{MPP}}{I_{SC} - I_{MPP}} \tag{2.10}$$

$$R_s = \frac{k\,T_r\,n_s\,\dfrac{log\left(\dfrac{I_{L_{ref}} - I_{MPP} - \dfrac{V_{MPP}}{R_{sh}}}{I_{L_{ref}} - \dfrac{V_{OC}}{R_{sh}}}\right)}{q} - V_{MP} + V_{OC}}{I_{MPP}} \tag{2.11}$$

$$\gamma = q\frac{V_{MPP} + I_{MPP}\,R_s - V_{OC}}{k\,Tr\,n_s\,log\left(\dfrac{I_{L_{ref}} - I_{MPP} - \dfrac{V_{MPP} + I_{MPP}\,R_s}{R_{sh}}}{I_{L_{ref}} - \dfrac{V_{OC}}{R_{sh}}}\right)} \tag{2.12}$$

$$I_{0_{ref}} = \frac{I_{L_{ref}} - \dfrac{V_{OC}}{R_{sh}}}{exp\left(q\dfrac{V_{OC}}{k\,T_r\,\gamma\,n_s}\right) - 1} \tag{2.13}$$

$$I_{L_{ref}} = I_{SC} + I_{0_{ref}}\left(exp\left(q\,I_{SC}\frac{R_s}{\gamma\,k\,T_r\,n_s}\right) - 1\right) + I_{SC}\frac{R_s}{R_{sh}} \tag{2.14}$$

The automatic procedure from datasheet specifications to model parameters can be performed in a light way thanks to the simplicity of the 1-diode model, which does not require to know physical details about the PV-cells. On the other hand, the 1-diode model is good enough to reasonably estimate the PV plant power production. In fact, if compared, for example, with the 2-diode model, which gives a more physically sophisticated description, it shows a difference in power estimation error below 1% [104].

2.2.4.1 Cell Temperature Estimation

The most important factor affecting the energy yield of a PV cell is the solar irradiance; however, since solar cells are made of semiconductors, they are also very sensitive to temperature. As accounted for in 1-diode equations, the open-circuit voltage decreases significantly with increasing temperature of the PV module,

whereas the short circuit current increases slightly. Depending on the technologies, the $\mu_{I_{SC}}$ factor ranges from around 0.04 to 0.09 %/°C, while the $\mu_{V_{OC}}$ is in the range of -0.25 %/°C to -0.45 %/°C, giving a total MPP variation from -0.13 %/°C to -0.48 %/°C [105].

For most PV installations, direct measurements of the cell temperature are not available, thus cell temperature datasets are almost non-existent. Therefore, it is necessary to empirically parameterize the physical relation between the PV cell temperature (T_c), ambient air temperature (T_a), incoming irradiance (G) and other meteorological parameters, among which the most significant is the wind speed (v_w). Authors in [102] compare six different cell temperature static estimation models. Through experimental validation they identify the one proposed in [106] (*Mattei 1-2*) as the most suitable for the majority of the PV plants with modules made of silicon-based cells. Nevertheless, in case of amorphous silicon PV modules the model in ref. [107] (*Koehl*) has proved to be more accurate; finally, in case of Cadmium Telluride (CdTe) cells, the model in [108] (*Kurtz*) is found to give the best match. In (2.15) we report the equation of the *Mattei 1* model for cell-temperature (T_c) estimation:

$$T_c = \frac{U_{PV}(v_w)\cdot T_a + G\cdot[\tau\cdot a - \eta_r\cdot(1-\beta_r\cdot T_r)]}{U_{PV}(v_w)+\beta_r\cdot\eta_r\cdot G} \tag{2.15}$$

where:

- U_{PV} is the heat exchange coefficient of the PV module [W·m^{-2}·°C^{-1}] empirically defined in [106] as $U_{PV}(v_w) = 26.6 + 2.3\ v_w$;
- v_w is the wind speed [m/s];
- T_a is the ambient temperature [°C];
- G is the solar irradiance [W/m^2];
- $\tau \cdot a$ is the product between transmittance and absorption coefficients of the PV cell: one can assume 0.81 as typical value;
- η_r is the efficiency of the module when operated in STC;
- β_r is the temperature coefficient at STC;
- T_r is the STC reference temperature (25 °C).

For the sake of completeness, below we give the equations of the *Koehl* (2.16) and *Kurtz* (2.17) models:

$$T_c = T_a + \frac{G}{U_0 + U_1 \cdot v_w} \tag{2.16}$$

$$T_c = T_a + G \cdot e^{-3{,}473 - 0{,}0594\, v_w} \tag{2.17}$$

where:

v_w, T_a, G are the same as in (2.15);

U_0, U_1 are constants depending on the specific PV cell technology: in case of amorphous silicon typical values are $U_0 = 25.73$ and $U_1 = 10.67$ [m^{-1}·s] (see [102] for additional values).

In our model we implemented all six equations reviewed in [102], namely *Standard*, *Mattei 1*, *Mattei 2*, *Skoplaki*, *Koehl*, *Kurtz* (Figure 2.11). The user is allowed to select the desired one from the mask of the PV plant subsystem: the default choice is *Mattei 1*.

2.2.4.2 MPPT Controller

The MPPT controller observes its internal voltage set-point (*V_ref*) and the power output (*P*) of the two most recent simulation time steps and determines the optimum operating point on a virtual I-V curve. We choose to implement the *perturb and observe* MPPT algorithm thanks to its computational simplicity. As shown in Figure 2.13, for each step of the discrete time simulation, power and voltage increment or decrement (ΔP_{PV} and ΔV_{ref}) are observed, allowing to determine if the present operating point of the PV plant is to the right or left with respect to the MPP.

An increase or decrease action is taken accordingly on the voltage reference output of the controller (V_{ref} in Figure 2.10). In particular, if the power output is decreasing (the system is moving away from the MPP), we need to take an action on V_{ref} opposite to the last one taken, therefore, if the voltage was decreasing (we are to the left of the MPP), we increase it and, vice versa, if it was increasing (we are to the right of the MPP), we decrease it. In the opposite way, if the power is increasing (the system is approaching the MPP), we keep taking the same action on V_{ref}, therefore, if the voltage was decreasing (we are to the right of the MPP) we keep decreasing it, vice versa, if it was increasing (we are to the left of the MPP), we keep

increasing V_{ref}. In Figure 2.14 we show the Simulink implementation of the MPPT controller with an additional control logic to stop the perturb action when the MPP has been reached, and an additional *curtailment* signal that allows to perform a *Load Power Tracking* (LPT) algorithm when the UPSC grid is required to operate in islanded mode and there is an excess in energy production.

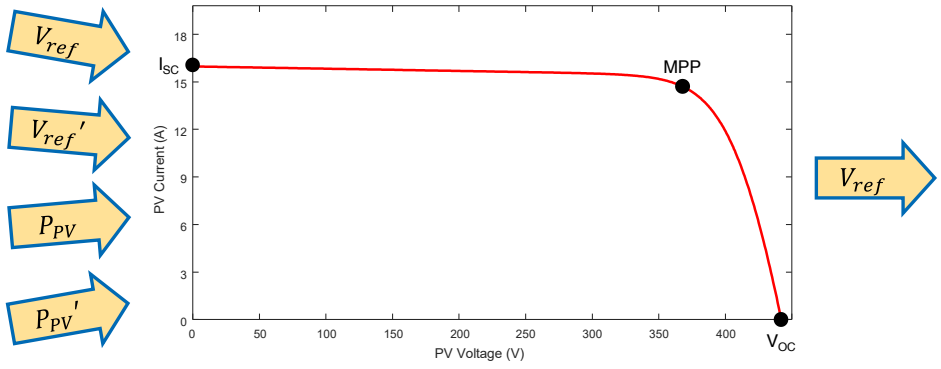

$\Delta P_{PV} > 0$	$\Delta V_{ref} > 0$	Operating point	$(\Delta P > 0) \oplus (\Delta V > 0)$	Action
0	0	left	0	Increase V_{ref}
0	1	right	1	Decrease V_{ref}
1	0	right	1	Decrease V_{ref}
1	1	left	0	Increase V_{ref}

Figure 2.13: Graphical representation of the *perturb and observe* MPPT algorithm implementation.

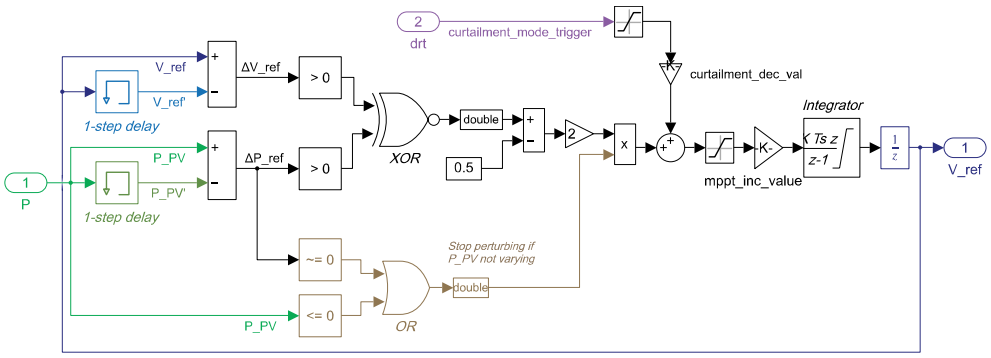

Figure 2.14: Simulink implementation of the *perturb and observe* MPPT control algorithm.

2.2.4.3 Interface with the UPSC Grid

As shown in Figure 2.10, the power output obtained by the equations (*P_out*) is then injected into the Simscape power grid (at nodes *L1*, *L2*, *L3*) by three current generators, each with a complex set point obtained dividing the complex power by the measured grid voltage. The real and imaginary part of the injected power are computed by the *PQ controller* subsystem. The input signal *Q_set* is the reactive power exchanged with the NPG. The controller determines the value of the output Q in order to minimize the reactive power *Q_set*. The maximum reactive power that can be injected (or absorbed) is limited by $cos\varphi = 0.9$ (a typical value for PV inverters). The *P* output is computed from the DC power (*P_out*) and the reactive power.

For islanded MG operation, the PV plants and the BESS must be sized in such a way as to keep service disruption and load shedding within acceptable limits. This implies, in particular, that over significant parts of the year the PV plant production may exceed the load demand. When this happens, and the BESS is in full-charge conditions, the PV power production must be curtailed. Therefore, the MPPT controller model supports a derating mode, the activation of which is driven by a central supervision unit. In derating mode the controller drifts from the MPP according to the derating value provided, thus decreasing the output power according to the load demand.

The solar irradiance data used for computing the PV energy production, as well as temperature and wind speed records, come from the ARPAE database of the Emilia Romagna region [109].

2.2.5 BESS Modeling

As shown in Figure 2.15, the storage system model consists of four sub-systems: (1) the interface with the campus distribution grid when the UPSC is powered by the NPG through the PCC (Converter AC Side - gc); (2) the interface with the campus grid for operation in islanded mode (Converter AC Side - ngc); (3) the charge/discharge controller (gc Controller); (4) the Battery block. 3 and 4 are implemented with mathematical blocks and equations. The interface blocks represent at a high level of abstraction the DC/AC and DC/AC converters.

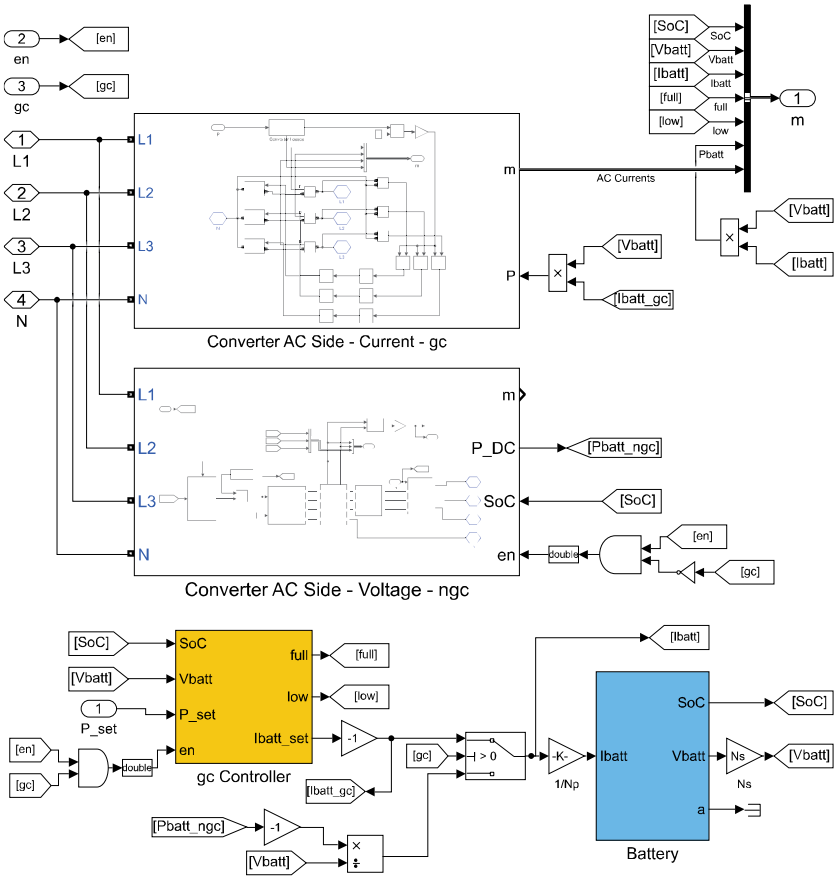

Figure 2.15: BESS Simulink implementation.

When in grid-connected mode, the interface with the AC grid is modeled with three current generators, similarly to the PV interface model described above. The generated or absorbed power is computed by the gc Controller. The model accounts for conversion efficiencies (assumed constant for simplicity). The *gc Controller* features an integral controller that computes the set-point for the current entering or exiting the battery. According to the battery output voltage, power is computed and used as set-point for the AC/DC or DC/AC interface plus/minus the conversion losses. The gc Controller is coordinated by a central control unit that provides the power set point (P_set). Charge and discharge rates are computed based on the requested power (positive for discharging, negative for charging) and the maximum

ratings of the converter and battery. The BESS output saturates when the request exceeds the maximum ratings. The P_set signal is determined by the central control unit, the policy of which is to minimize the energy bought from the NPG by storing the PV energy excess in the BESS.

When the MG disconnects from the NPG (e.g., during faults) and works in islanded mode, the *Converter AC Side - ngc* interface is selected: the conversion stage is a 3 phase amplitude controlled AC voltage source, as shown in Figure 2.16. The amplitude of the output voltages is computed by the *Vadjust* subsystem according to the instantaneous value of the state of charge (SoC). 50% SoC corresponds with an output voltage equal to the nominal value; then, the output voltage amplitude is varied above or below the nominal value if the SoC goes over or under its midpoint, respectively. This allows different BESS installations to automatically equalize the respective SoC by supplying more or less energy to the grid. The voltage/SoC slope is constant when 22% < SoC < 90% and becomes steeper outside this range to prevent battery overcharging and over-discharging. In islanded mode, a central control unit receives data from the BESS: upon reaching the full SoC value (90%), the control unit sends a derating value to the PV MPPT controllers, based on the SoC and its slope.

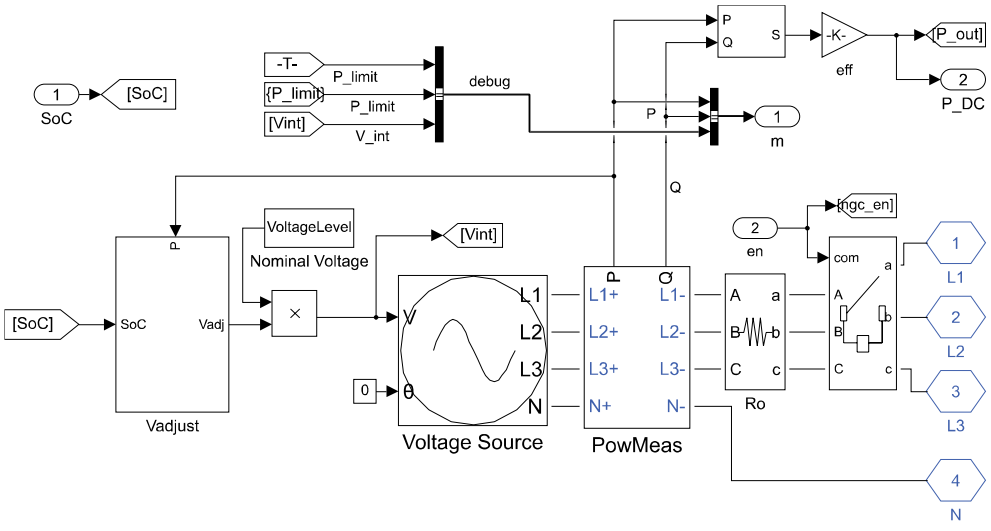

Figure 2.16: BESS AC interface when operated in islanded mode.

The battery cells (Figure 2.17) are modeled by the Tremblay Dessaint equations [110], wherein the SoC is computed by a time-domain integration of the cell current; the output voltage is computed based on the SoC using an empirical equation tuned on the basis of the following parameters extracted from the discharge curve: the output voltage at fully charged cell (E_{full}); the output voltage and depth of discharge (DoD) at the end of the exponential zone (E_{exp}, Q_{exp}); the output voltage and DoD at the end of the nominal zone (E_{nom}, Q_{nom}); the model also requires a value for the internal equivalent series resistance and an estimate of the battery dynamic response time (experimentally determined to be 30s for most applications [110]). The dynamic response time is necessary to compute a filtered time profile of the current (i^*) used to recreate the dynamic behavior.

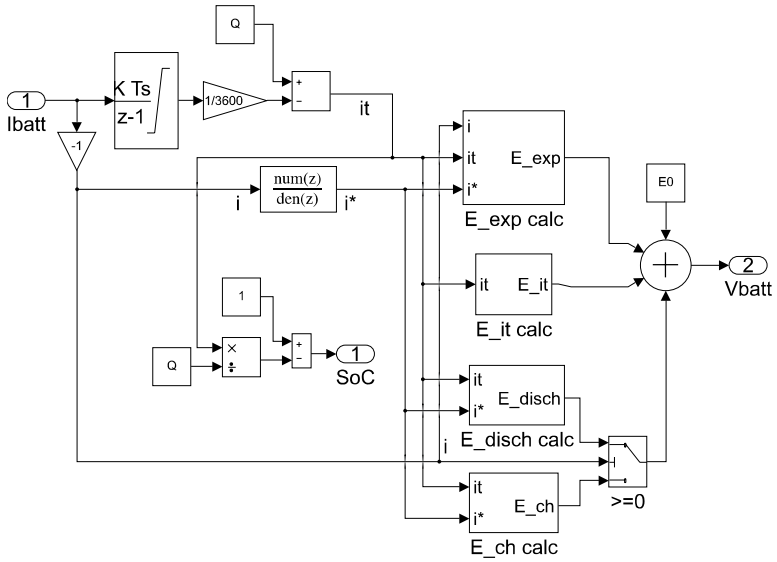

Figure 2.17: Battery cell model.

Two slightly different equations are employed in computing the battery terminal voltage (V_{batt}) for the discharge and charge modes:

- *discharge mode:*

$$V_{batt} = E_0 - R \cdot i - K\frac{Q_{full}}{Q_{full}-Q_d}(Q_d + i^*) + A\exp(-B \cdot Q_d) \tag{2.18}$$

- charge mode:

$$V_{batt} = E_0 - R \cdot i - K\frac{Q_{full}}{Q_{full}-Q_d}Q_d - K\frac{Q_{full}}{Q_d - 0.1 \cdot Q_{full}}i^* + A\exp(-B \cdot Q_d) \quad (2.19)$$

where:

V_{batt} [V]	is the cell output voltage;
R [Ω]	is the internal series resistance;
Q_{full} [Ah]	is the battery full capacity (at 100% SoC);
Q_d [Ah]	is the battery discharge level;
i [A]	is the current exiting the battery,
i^* [A]	is the filtered version of the current computed in order to emulate the dynamic response of the battery.

The constants A, K, E_0, in the equations above are computed at the model initialization phase (before the simulation starts) by setting the cell parameters values, namely: E_{full}, E_{exp}, Q_{exp}, E_{nom}, Q_{nom}. The constant B is set at $3/Q_{exp}$, as empirically obtained in [110].

The BESS model features reactive power compensation implemented in the same way as in the PV model.

2.2.6 EV Charging Station Modeling

The battery cell model described above is used to emulate the operation of the 10 EV charging stations located in front of the Q02 building (where we also have the largest PV plant, as discussed before). Since no field data have been collected yet from this facility, we simulated a reasonable rate of random activation of the charging stations (during working hours and days). Each station is described (as in Figure 2.18) by a charge controller, the interface with the AC grid, and a battery cell pack simulating the EV under charge. When the start signal is activated (a vehicle charging request), if the station is not busy with a previous charge request the SoC is reset and charging proceeds until full SoC is achieved. Charging is regulated by the *Charger & Control* subsystem, which implements a constant current/constant voltage (CC/CV) algorithm [111]. Figure 2.19 shows an example of a charging profile of one of the charging stations computed by the model.

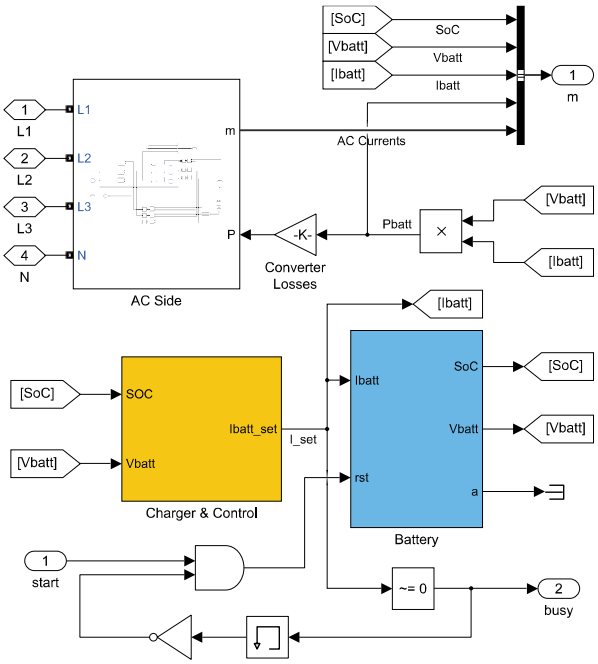

Figure 2.18: Simulink model of an EV charging station.

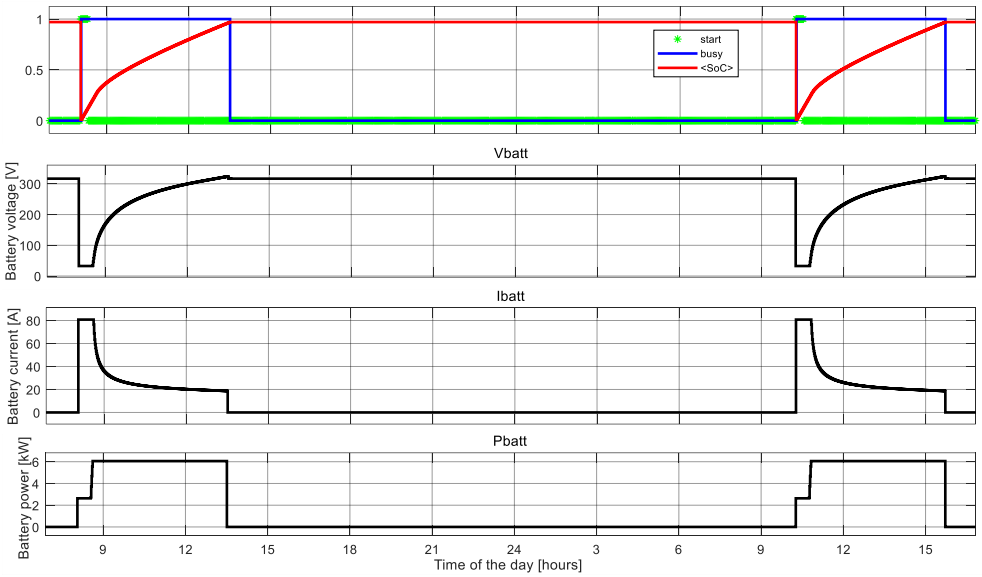

Figure 2.19: Example of 2 charging cycles performed by an EV charging station.

2.3 Simulation Results

Since the aim of our model is to support planning for increasing penetration of PV generation and BESS, maintaining at the same time satisfactory grid performance, two key aspects are the economic benefits and the environmental footprint.

From an economic point of view, we consider the following indicators (prices and costs in Table 2.4):

- cost of energy bought from the power grid (C_{PG}^{b} $\left[\frac{€}{\text{kWh}}\right]$);
- revenue from energy sold to the grid (C_{PG}^{s} $\left[\frac{€}{\text{kWh}}\right]$);
- capital cost (installation and maintenance) for PV plants (20 year depreciation time) (C_{CPV} $\left[\frac{€}{\text{kW}_\text{p} \cdot \text{year}}\right]$);
- capital cost (installation and maintenance cost) for the BESS (10 year depreciation time) (C_{CESS} $\left[\frac{€}{\text{kWh} \cdot \text{year}}\right]$).

The total cost C_{TOT} at the end of the year is computed as:

$$C_{TOT} = \int_0^{T_{stop}} (P_{PG}^{+}(t)\ C_{PG}^{b} - P_{PG}^{-}(t)\ C_{PG}^{s})\ dt + \\ + \frac{T_{stop}}{8760}\ (IS_{PV}\ C_{CPV} + IS_{ESS}\ C_{CESS}) \qquad (2.20)$$

where:

P_{PG}^{+} is the power coming from the power grid (kW);
P_{PG}^{-} is the power (absolute value) injected into the NPG (kW);
IS_{PV} is the overall size of the PV installations expressed in kW_p;
IS_{ESS} is the total installed BESS capacity in kWh;
T_{stop} is the duration of the simulation time window in hours.

As far as the environmental footprint is concerned, we consider the CO_2 emission due to the energy bought from the NPG. The CO_2 emission rate (R_{CO_2}) is estimated based on real-time data from [112] ($0.270 \frac{\text{kg}(CO_2)}{\text{kWh}}$ for northern Italy). The total amount of CO_2 emitted over the simulation period is given by:

$$T_{CO_2} = \int_0^{T_{stop}} P_{PG}^{+}(t)\ R_{CO_2}\ dt \qquad (2.21)$$

Table 2.4: Prices and costs considered in the model for economic estimates.

C_{PG}^{b}	C_{PG}^{s}	C_{CPV}	C_{CESS}
$0.182\ \frac{€}{kWh}$	$0.09\ \frac{€}{kWh}$	$25\ \frac{€}{kW_p \cdot year}$ (from [113])	$35\ \frac{€}{kWh \cdot year}$ (from [114])

We performed simulations comparing three configurations of the UPSC grid: 1) no PV, no BESS; 2) 3 MWp installed PV, no BESS; 3) 3 MWp installed PV, 4.5 MWh installed BESS. We considered three 1-week scenarios in the months of April, June, and November. The PV installation size assumes complete covering of the available rooftop area and is approximately equal to the peak load demand. The size of the BESS is tuned so that the whole SoC dynamics is exploited during operation.

Before discussing the obtained results, it is important to point out that the prices and the costs considered in this simulation campaign are referred to mean values computed in the year 2020 considering the specific case of the UPSC. The aim of this dissertation is to focus on the methodology, therefore, simulation results are intended to show the kind of considerations and evaluations that can be made thanks to the developed models, once the constraints dictated by the specific case of study have been fixed.

Figure 2.20 illustrates the results for the April week. The power coming from (if positive) or injected to (if negative) the grid is shown in Figure 2.20a. With neither PV nor BESS (solid red line), the whole load demand is serviced by the NPG and power can only take on positive values. With PV generation (dotted blue line), during daytime the load demand is completely satisfied by PV, with energy surplus during peak production hours sold to the NPG (negative power values). At nighttime, loads are supplied by the NPG. Finally, when we introduce the BESS (black dot-dashed line) the amount of energy sold to the NPG is minimized because the excess PV production is stored in the batteries. Figure 2.20b shows the power exchanged with the BESS: positive when supplying loads (discharging), negative when storing energy (charging). Figure 2.20c shows the SoC.

Table 2.5 gives the total economic (capital plus running costs) and carbon impact of the UPSC grid over 3 weeks in the months of April, June, and November, respect-

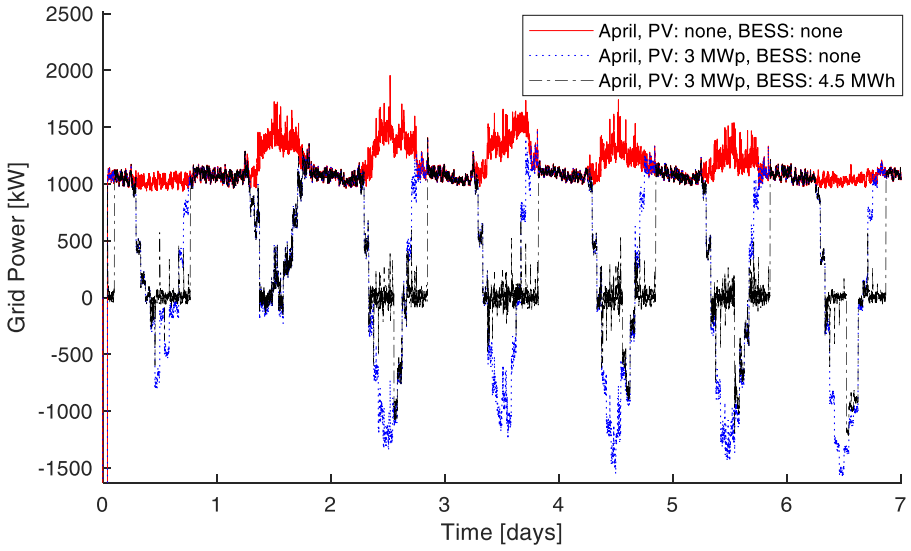
April, PV: none, BESS: none
April, PV: 3 MWp, BESS: none
April, PV: 3 MWp, BESS: 4.5 MWh
Grid Power [kW]
Time [days]
2500
2000
1500
1000
500
0
-500
-1000
-1500
0
1
2
3
4
5
6
7

(a)

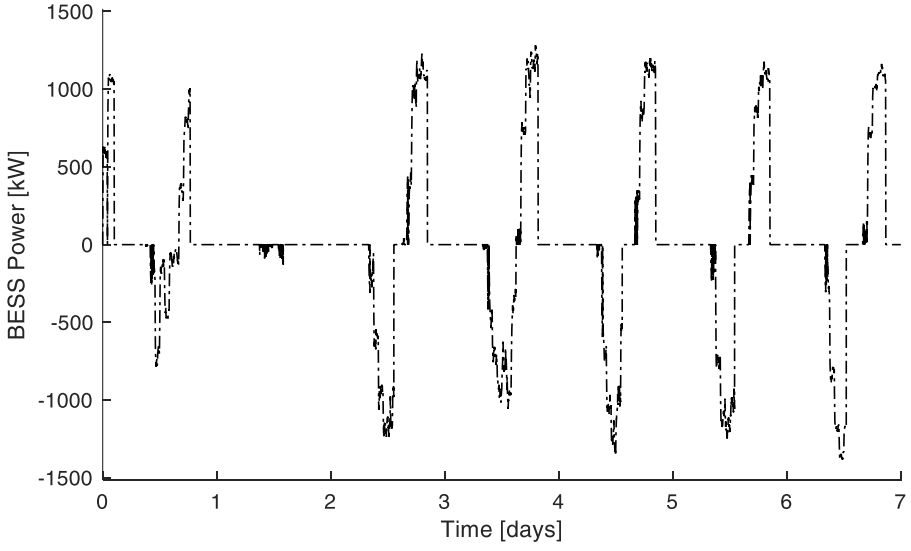
BESS Power [kW]
Time [days]
1500
1000
500
0
-500
-1000
-1500
0
1
2
3
4
5
6
7

(b)

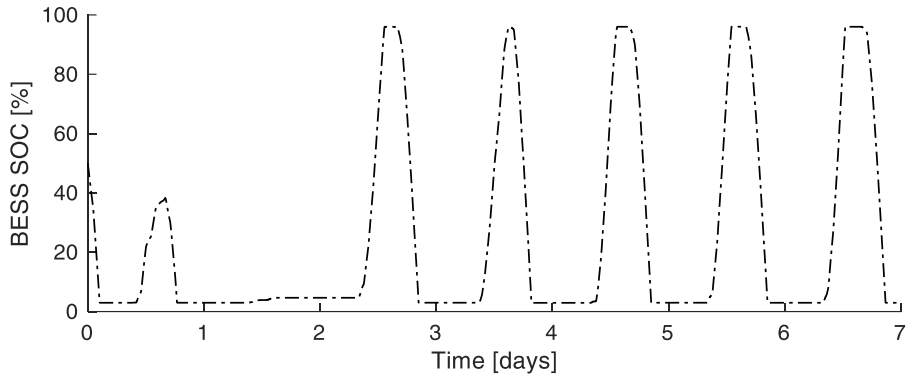

(c)

Figure 2.20: Simulation results for a week at the end of April. (a) Three scenarios are compared: with connection to the utility grid only (red line); with 3 MW_p PV plants installation (blue dotted line); with 3 MW_p PV plants combined with a centralized 4.5 MWh BESS (black dot-dashed line). (b) Power exchanged with the BESS. (c) State of charge of the BESS.

tively. Simulation results show that from an economic point of view, large benefit comes from PV installation, while the BESS brings no additional cost reduction. PV plants are expected to bring economic savings in a 16% - 51% range and CO2 yearly emission reduction between 16% - 42%, depending on weather conditions. Conversely, the additional installation of a BESS is not economically convenient: relative to the PV only case the estimated loss is 13% - 29%. However, the BESS yields 4% - 19% CO2 reduction.

We also performed year-long simulations, summarized in Table 2.6, for the years 2014, 2015, and 2016. In Figure 2.21, we give a detailed view of the total economic expenditure (energy + system operation costs) and of the CO_2 emission trends for the year 2016 over the 3 considered scenarios. Year-long simulations also confirm that with the current prices the introduction of a BESS is unfavorable from a purely economic point of view (8-9% economic loss if compared to the PV only case), but it allows to decrease the CO2 emissions by an additional 5-6% relative to the PV-only case. However, it is expected that in the next few years the economic outlook for BESS installations will improve [114]. In, particular, according to a recent survey by NREL [115], the next 5 years should bring a 14-36% cost reduction, with a middle-of-the-road value around 25.

We performed an additional set of year-long simulations in order to assess the effect of the reactive power compensation systems the PV and BESS models.

Table 2.7 shows the results for 2014, 2015 and 2016 with and without reactive power compensation, considering a typical power-factor limit of 0.9.

Table 2.5: Results of week-long simulations under three scenarios. The PV and BESS installed capacities, where present, are 3 MWp and 4.5 MWh, respectively.

		April	**June**	**November**
Total expenditure [10^3 €]	*no PV no BESS*	31.8	41.4	38.6
	PV no BESS	15.6 (-51%)	25.5 (-38%)	32.4 (-16%)
	PV + BESS	20.0 (-37%)	32.8 (-21%)	36.6 (-5%)
Total CO_2 emissions [10^3 kg]	*no PV no BESS*	66.0	88.0	77.3
	PV no BESS	38.4 (-42%)	56.2 (-36%)	64.7 (-16%)
	PV + BESS	31.1 (-53%)	53.9 (-39%)	61.3 (-21%)

Table 2.6: Results of year-long simulations under three scenarios. The PV and BESS installed capacities, where present, are 3 MWp and 4.5 MWh, respectively.

		2014	**2015**	**2016**
Total expenditure [10^6 €]	*no PV no BESS*	2.20	2.20	2.20
	PV no BESS	1.55 (-30%)	1.48 (-33%)	1.49 (-32%)
	PV + BESS	1.67 (-24%)	1.62 (-26%)	1.63 (-26%)
Total CO_2 emissions [10^6 kg]	*no PV no BESS*	4.24	4.24	4.24
	PV no BESS	3.04 (-28%)	2.95 (-30%)	2.93 (-31%)
	PV + BESS	2.88 (-32%)	2.78 (-34%)	2.79 (-34%)

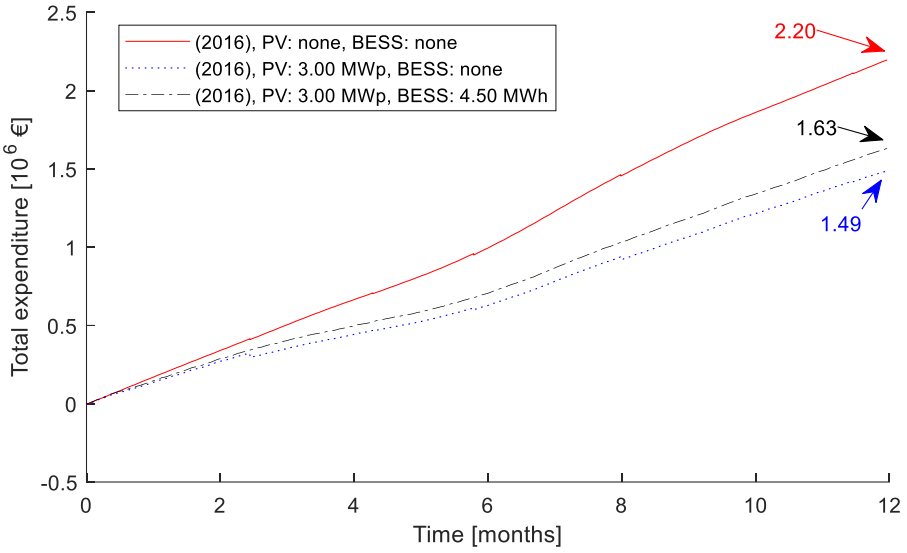

(a)

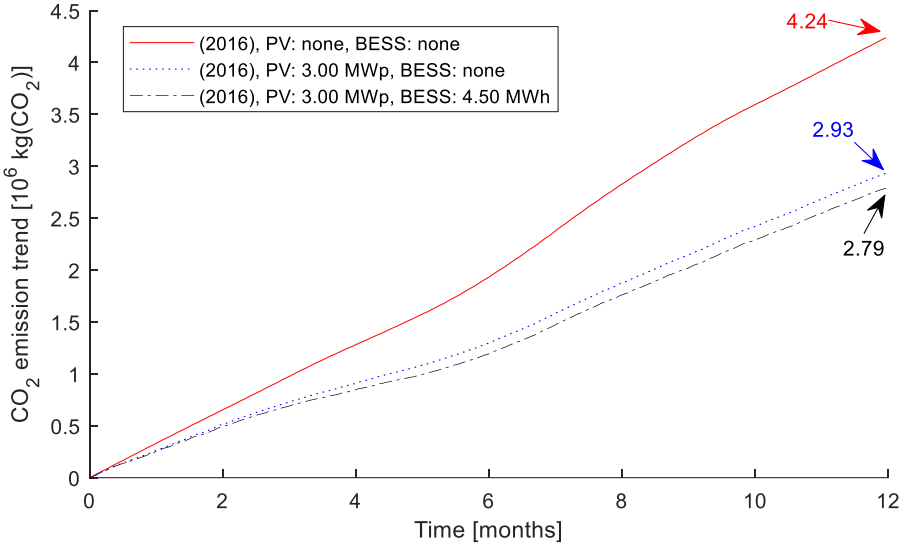

(b)

Figure 2.21: Total economic expenditure and CO_2 emission trends for the year 2016 over the 3 considered simulation scenarios.

An example of islanded mode operation in the case of NPG fault is shown in Figure 2.22. When undervoltage (< 85% of the nominal voltage) or overvoltage (> 110% of the nominal voltage) are detected, the main controller triggers a Grid fault signal, the campus grid is physically disconnected from the NPG (the Grid connected mode signal goes low) and the BESS starts operating accordingly as an AC voltage generator.

Table 2.7: Reactive energy exchanged with the power grid with and without reactive power compensation by PV and BESS.

		2014	**2015**	**2016**
Reactive energy exchanged with the grid [MVARh]	*Without Q compensation*	4432	4432	4429
	With Q compensation	3217	3153	3054
	Δ (%)	-27.4%	-28.9%	-31.0%

The example shows two faults. The first one happens at a high solar irradiance time of day, when the PV production exceeds the load demand and the BESS is at high SoC level (over 90%). As shown in Figure 2.22 (Power Grid Power chart), just before the fault the exchange between the campus grid and the NPG is nearly zero due to high PV production. When the fault happens (red trace in the top chart), the grid is disconnected and about 20 minutes later the PV plants are put in derating mode (green trace in the top chart) due to the full charge condition of the BESS, in order to curtail the excess of local energy production. When the second fault happens (red trace in the top chart), the SoC of the BESS is below 12.5%, so 90% of the loads are disconnected (Load Shedding chart), in order to guarantee servicing high priority loads. After a few minutes, thanks to PV production, the BESS SoC starts rising (BESS SoC chart), and the load shedding action moves to lower priority classes, resulting first in 25% (after 5 minutes) and then 50% (after 20 minutes) of the loads restored to operation.

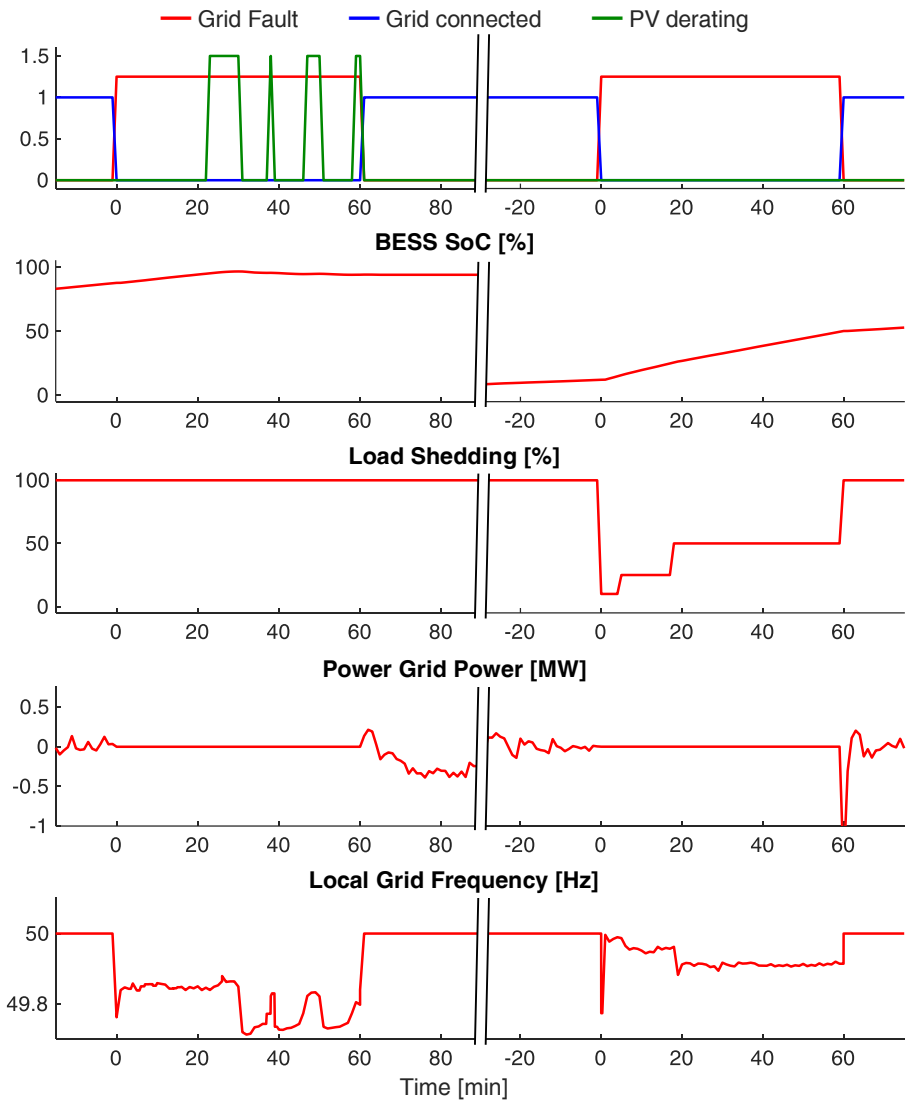

Figure 2.22: Islanded MG operation in two instances of power grid fault.

2.4 Droop Characteristics

When the UPSC grid is in islanded mode, the MG frequency is not fixed by the NPG. As discussed in 2.1, to achieve fast simulations over long time intervals our approach is based on a phasor simulation solver, which considers the frequency constant. This makes it impossible to consider a frequency control loop with primary and secondary control such as should be implemented in the real microgrid (see 1.4.2). However, we implemented a simple mathematical estimation of the islanded MG frequency based on the typical characteristics of a power/frequency (P/f) droop control [46], [116], [117]:

$$f_i = f_0 - k_i \cdot \left(P_i - P_{i_0}\right) \tag{2.22}$$

where P_i is the power supplied to the local grid by the *i*-th unit and P_{i_0} is its reference value; f_0 is the nominal frequency (no load conditions); f_i is the output frequency; k_i is the P/f droop.

Two different droop characteristics are implemented for the PV plants and for the BESS, respectively, to emulate the following scenarios:

1) as long as the load demand is lower than (or equal to) the total available PV power, frequency regulation is performed by the PV units;
2) when the load demand cannot be satisfied by the PV plants, regulation is taken over by the BESS. In the latter case, frequency regulation considers both the power delivered by the storage system and its SoC.

In Figure 2.23a we show the PV droop curve, where f_0 is the nominal frequency (50 Hz in Europe) and f_1 is the value when PV units are at full-load condition; Δf_{PV} is the maximum possible frequency variation when regulation is performed by the PV units. Figure 2.23b shows the BESS droop: when the SoC increases the system is allowed to deliver more power. When the BESS takes control of the regulation, the MG frequency varies from f_1 (end of the PV units' regulation region) to f_{min} (minimum allowed frequency allowed).

The bottom trace in Figure 2.22 shows the frequency estimation for islanded mode under the two contingencies described in 2.3. In the first fault, frequency is regulated by the PV droop in the derating mode intervals, by the BESS in the remaining intervals. In the second fault, the PV production is greater than the load

demand (the BESS is recharging), therefore the PV inverters take charge of the frequency regulation.

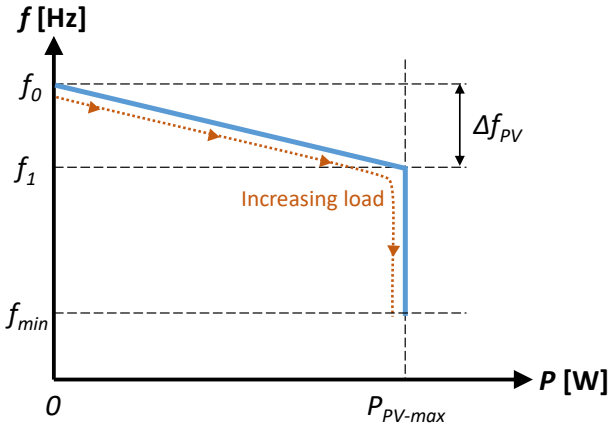

(a)

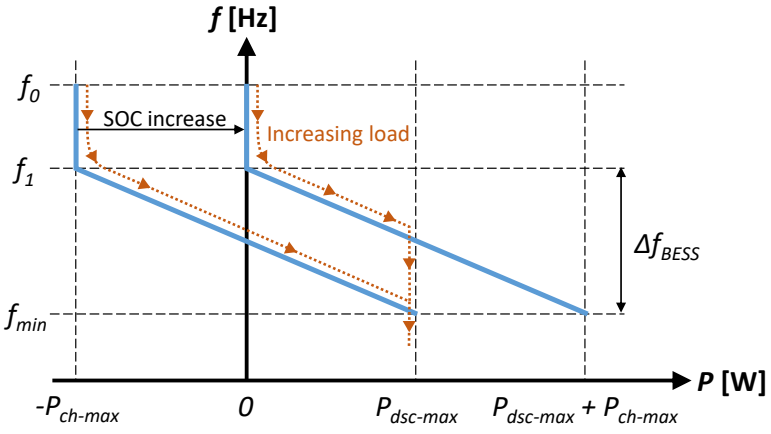

(b)

Figure 2.23: P/f droop characteristics for the PV units (top) and the BESS (bottom).

In this chapter, a library of models for top-level behavioral simulations of a campus microgrid has been presented: including PV generation, BESSs, load profiles, EV charging stations, heat-pump-based heating/cooling systems, etc. The aim of the tool is to simulate the evolution of the grid on a large time scale (in the order of months to years) allowing to make system-level considerations about the introduction and sizing of new grid components considering many aspects: from the electrical one to the economic balance, the environmental benefits, etc. Thanks to the given level of abstraction, the time required to complete a simulation is kept into reasonable bounds, obtaining a ratio between the simulated time span and the computation time lower than 0.15% (i.e., about 9 to 12 hours – depending on the host CPU – for simulating an entire year).

Chapter 3

Smart Soiling Monitoring System for Photovoltaic Modules

The diffusion of decentralised small-scale RES power generation is giving a boost to the development of smart NG, particularly to increase the sustainability of electricity production and the efficiency of distribution. To ensure continuity of service, the reliability and maintainability of NGs are crucial problems that must be considered. Consequently, alongside management aspects connected with the generation and efficient use of RES, there are also equally important aspects related with the system maintenance and its automation via continuous real-time monitoring. Smart monitoring and maintenance policies affect the quality and timing of restoring interventions and can significantly reduce downtime, therefore they can have a relevant impact on the energy production, cost and waste.

Solar photovoltaic technology is one of the renewable technologies, which has a potential to shape a clean, reliable, scalable and affordable electricity system for the future. In addition, it is the most abundant, inexhaustible and clean. Considering this fact, all over the world governments are encouraging the development and deployment of solar PV technology. Nevertheless, the use of solar PV modules requires particular attention to the monitoring and maintenance processes of the PV modules.

Thanks to its ubiquity and to the progress of PV technologies – which prompted significant cost reduction in the last decade [118] – solar energy often plays a key role in MGs and NGs.

The power output of PV installations depends on several factors: environmental factors such as solar irradiance, temperature, dust deposition, and system factors such as module and inverter efficiencies; storage capabilities also play a significant role in the overall system performance by allowing some decoupling between energy production and demand [119].

In the first place, the energy output of a PV module is directly related to the incoming solar energy, irradiance varying according to weather conditions and the sun position. The module output current is approximately linearly dependent on the impinging irradiance level, hence the MPP is strongly related to irradiance. Consequently, module soiling due to dust accumulation etc., and the maintenance countermeasures aimed at assuring adequate conversion efficiency over the PV plant lifetime, must be factored in when making life-cycle economic estimates for PV installations.

Soiling is caused by dirt, dust and other particles covering the surface of the PV modules. The dust composition (pollutants, airborne liquid constituents, particulates, pollen), colour (due to different mineral composition) and the amount and type of soiling vary widely with plant location [120]–[122]. The dust properties and its deposition rate are also affected by ambient conditions including humidity, wind speed and direction, and seasonal variations [123].

To counter the effects of soiling, panels must be periodically cleaned. This can be carried out with manual, mechanised, or robotic action by either wet or dry solutions, or by electrodynamic screen techniques [124], [125].

At present, most PV arrays are inspected and cleaned with a scheduling that typically does not depend on the actual state of dirtiness and its effect on energy production efficiency. Neglecting the efficiency/maintenance trade-off may result in wasteful costs due to unnecessary cleaning actions. Therefore, an automated soiling sensing approach can be useful to develop a decision-making process accounting also for the trade-off between reliability of energy production, demand/offer matching, and cost. In this way, a supervisor can plan targeted interventions with optimal maintenance timing.

Detection of dust deposition, concentrated dirt, or any soiling-related malfunction allows to decide when and what kind of cleaning is required, which calls for the development of a monitoring system with smart data management to automatically plan maintenance interventions, by combining weather forecasts and historical data,

irradiance sensors and soiling sensors. Papers in [126]–[129] show studies of PV module cleaning protocols, while analysis of the effects of dirt and dust deposition can be found in [130]–[134].

A few soiling detection kits for medium/large scale plants have already been developed and marketed. A non-exhaustive list is reported in refs. [135]–[141]. These systems base their operation on the comparison of electrical measurements obtained from a clean reference module and from one exposed to soiling agents (except for the one in [135], which is based on LED and photodiode soiling ratio detection).

In this chapter we propose a prototype of a soiling detection system for PV modules, designed to be a low-cost solution for small-scale DC NG operating either in grid-connected or islanded mode. The prototype sensor can detect dust deposition, thus helping distinguish between efficiency reduction due to dust and that due to degradation of PV modules or electronic components[142]. In order to test the usefulness of the automated sensing approach, we developed a MATLAB/Simulink model of a smart NG and estimated the economic benefits of the proposed approach and the optimum cleaning intervention rates [143].

3.1 Soiling Sensor Prototype

The proposed soiling sensing approach applies two techniques in parallel, namely, I-V curve analysis [144] and optical inspection [145], to quantify the degradation and qualify the dirt accumulated on PV modules, respectively.

The sensor consists of a small off-grid PV module employed as a reference for dust analysis. Factory data about the two different modules employed in the experiments can be found in Table 3.1. We developed an acquisition board for module electrical performance characterization and used a camera to take photos of the module to be processed by MATLAB optical analysis algorithms.

In order to measure the I-V curve of the PV reference module we built an acquisition board (Figure 3.1) equipped with a power MOSFET acting as an active load.

Table 3.1: Factory data of the reference modules use in the experiments.

S. E. Project SEM25M (c-Si)	
Open circuit voltage (V_{oc})	21.3 V
Short circuit current (I_{sc})	1.6 A
Maximum Power rating (P_{max})	25 W
Active area (A)	1869 cm^2

ICO-SPT-40W (thin-film)	
Open circuit voltage (V_{oc})	24 V
Short circuit current (I_{sc})	2.88 A
Maximum Power rating (P_{max})	40 W
Active area (A)	4293 cm^2

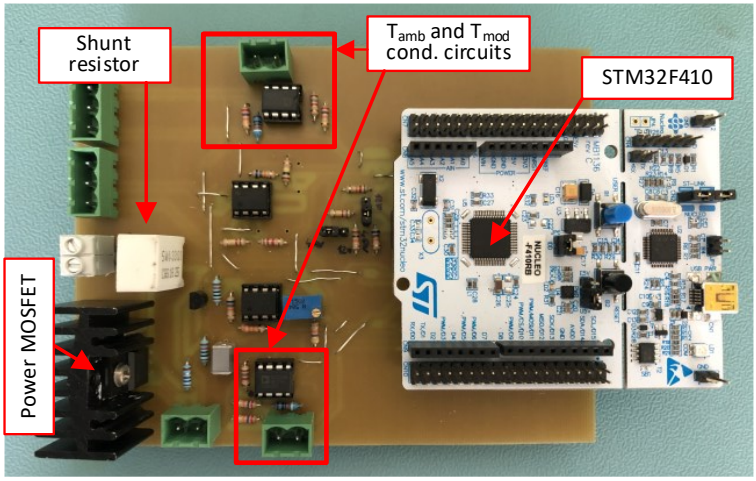

Figure 3.1: I-V characteristic acquisition board prototype.

An STM32 microcontroller generates a PWM wave, which is input to a low-pass filter. The duty-cycle is varied to obtain a DC voltage sweep that is applied to the transistor gate, thereby varying its channel resistance, from below threshold to fully-on state, hence obtaining a sweep from open circuit to short circuit for the PV module load.

Under each load condition, the current and voltage across the module are sampled by the microcontroller ADC, after being properly conditioned by onboard signal

attenuation circuits. The voltage drop across a shunt resistor is used to measure the magnitude of the current. The acquisition board is also equipped with circuits suitable for measuring the ambient temperature and the cell temperature by means of PT1000 thermistors. The collected data are finally sent to a computer where a MATLAB script performs the necessary processing tasks. The electrical and logical structure of the board is shown in Figure 3.2.

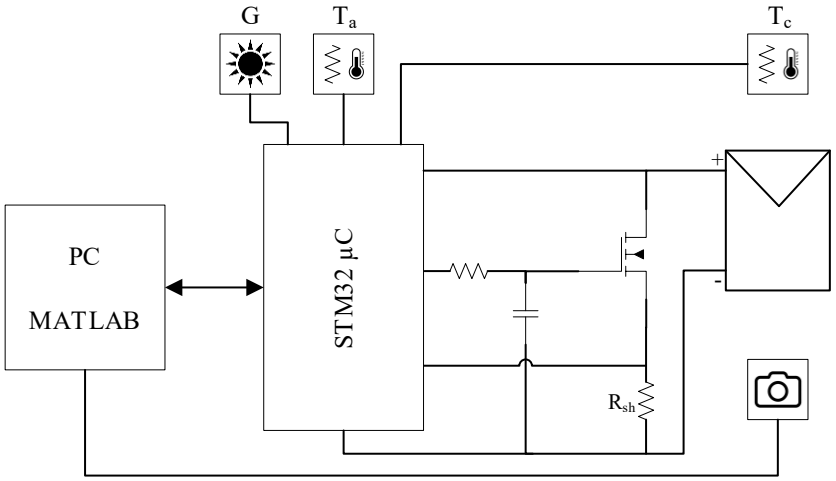

Figure 3.2: Diagram of the soiling sensing system.

The optical analysis is performed by taking digital photos of the module from a fixed position. A MATLAB script processes the image by artificial vision algorithms to calculate the amount of the soiled area. The process starts with a photo of the clean module, which serves the purpose of the masking step that is necessary to cut out non-active areas, such as the frame and cell interconnect metallization. Four red markers serve as reference points for the geometric transformation that removes deformation effects due to perspective.

Figure 3.3 shows the flowchart of the overall image analysis process. First the image object is loaded and the position of the markers detected. Second, the image is binarized applying appropriate color threshold levels. Third, the image is cropped and de-warped with the help of the markers. If the size of the image differs from the reference one, it is properly scaled to fit the reference frame. Finally, the dust-covered area is determined by means of a pixel analysis. In addition, the algorithm can

detect sub-areas characterized by different kind of depositions, thus allowing to establish if the dust distribution is uniform or aggregated in spots. Quantitative data is output on the percentage of covered area, the area of the widest spot (if any), and the prevailing color component (useful in determining the type of dirt).

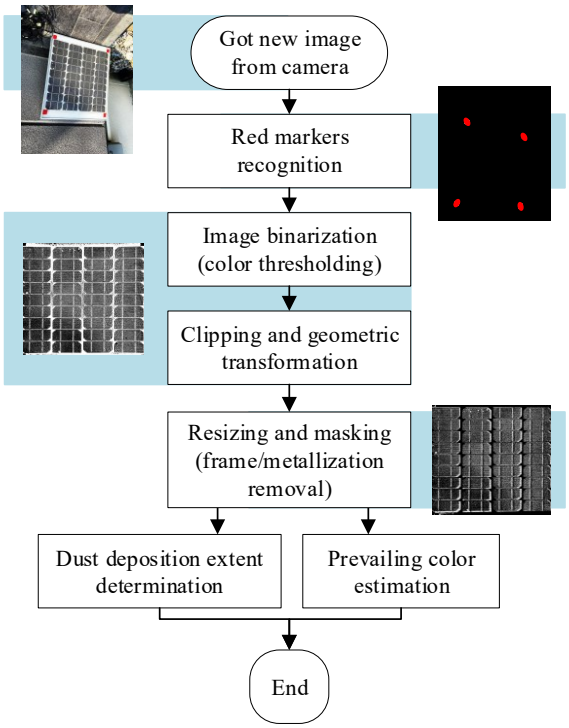

Figure 3.3: Flowchart of the image analysis process.

3.1.1 Experimental Results

Experiments were performed artificially depositing a weighted amount of dust on the reference module. Dust is collected from area surrounding the module. It is obtained by finely sieving some dry soil, resulting in a mixture of potting soil, sand, etc. This technique allows only particles with a diameter < 0.5 mm to pass through. Then, dust is spread on the reference module, which was preventively cleaned. The selected amount of powder is quantified by means of a precision scale with 1 mg accuracy. To avoid powder to be dispersed, a thin layer of water is sprayed on the

module. This also allows to emulate the effects of rain and dew effects on dust deposition. Once the module has dried the analysis procedure starts: the I-V curve is acquired in parallel with irradiance, ambient temperature, and cell temperature (a PT1000 sensor is tightly attached behind the PV reference module in correspondence with a cell). Meanwhile, a photo of the module is taken and processed. Figure 3.4 shows the test setup for I-V curves acquisition at different levels of controlled dust deposition.

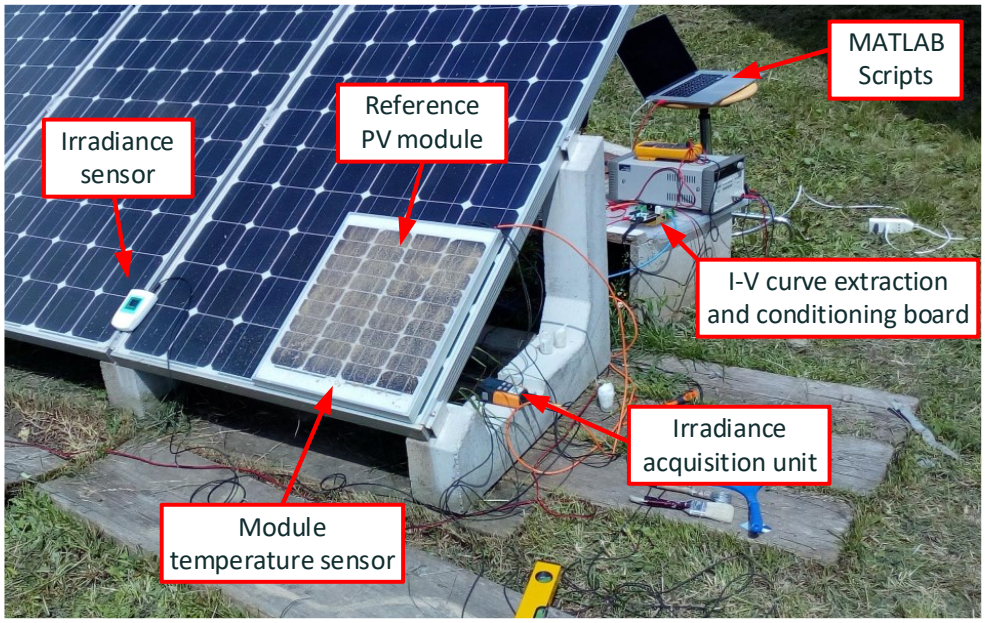

Figure 3.4: Soiling sensor test setup.

In Figure 3.5 we show some results obtained with I-V characteristics extraction for different amount of dust, for a c-Si (Figure 3.5a) and for a thin-film module (Figure 3.5b). Tests are performed for each module at constant irradiance and ambient temperature.

From each curve, the MPP is determined. MPPs are plotted in Figure 3.6, normalized with respect to the STC value, showing a quite linear relationship between the amount of deposited dust and power loss. The extracted slopes are about $1.7 \cdot 10^{-3}$ $(g/m^2)^{-1}$ and $1.9 \cdot 10^{-3}$ $(g/m^2)^{-1}$ for c-Si and thin-film, respectively.

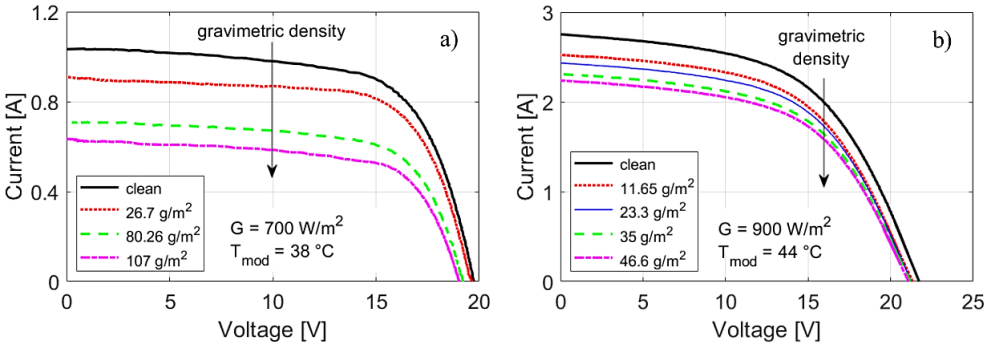

Figure 3.5: I-V characteristics at different levels of dust deposition obtained by means of the soiling sensor prototype: in a) using the c-Si reference module, in b) using the thin film module.

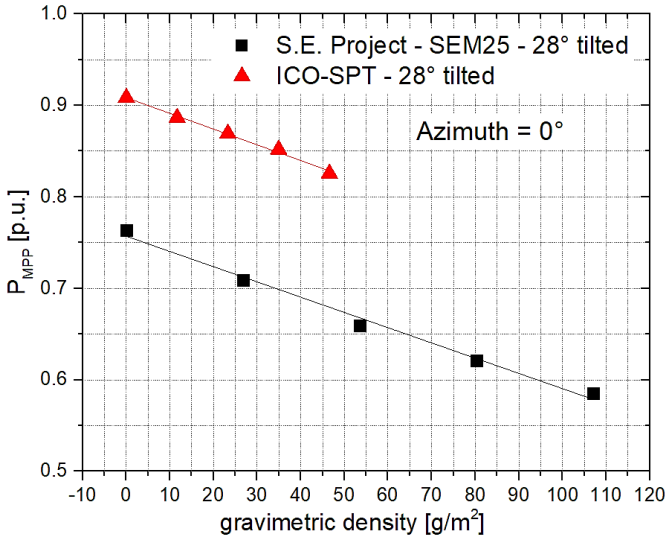

Figure 3.6: Normalized MPP plot as function of the deposited dust density.

The levels of dust we choose are not referred to a specific real case and have been chosen to be able to deposit a known quantity of dust in a controlled manner, in order to study the evolution of the electrical characteristics of the module as function of the quantity of deposited dust.

Optical analysis has also been performed on the reference modules. Results for two different dust distributions are shown in Figure 3.7. Case a) shows a uniform powder distribution on a c-Si module, resulting in a detected covered area of 36%; in case b) dust is deposited on a thin-film panel in non-uniform random stains, resulting in 10% coverage. Finally, Figure 3.8 illustrates a result obtained applying a new soiling technique in which dust is deposited using compressed air. This allows to obtain uniformity levels similar to the ones reached with aerosol method [144] but much more quickly.

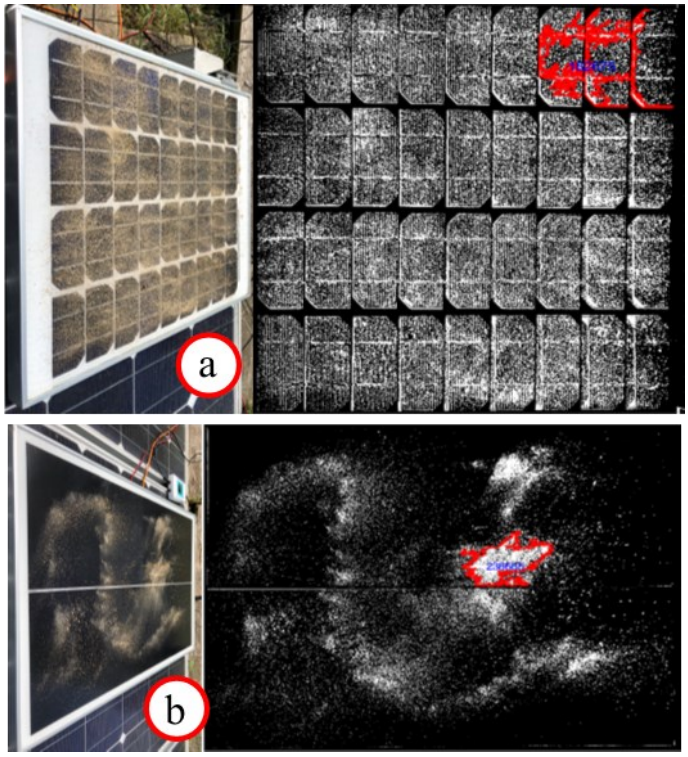

c-Si module

$G = 700\ W/m^2$
$T_{mod} = 38\ °C$

Thin-film module

$G = 900\ W/m^2$
$T_{mod} = 44\ °C$

Figure 3.7: Optical analysis results. a) uniform dust deposition on c-Si module (36% cov-ered area); b) stain-like deposition on thin film module (10% covered area). The camera viewport is parallel to the ground while modules are tilted by about 28°.

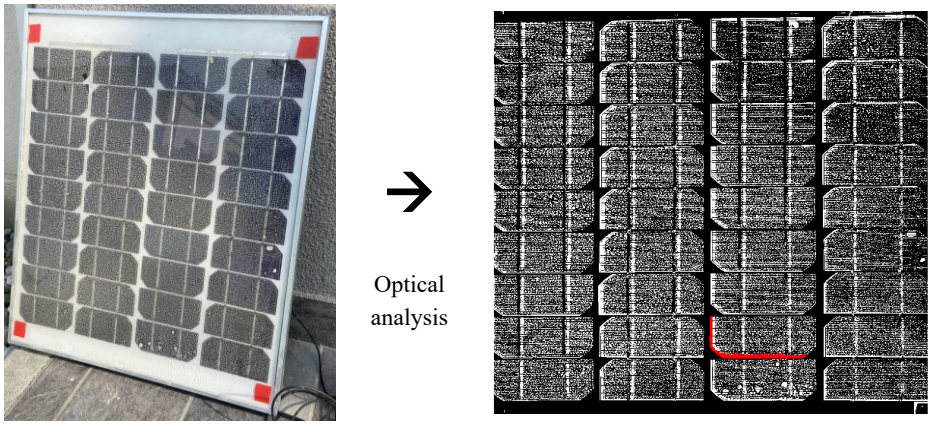

Figure 3.8: Photo of the c-Si PV module with compressed-air deposited dust (left) and image after MATLAB elaboration (right). Estimated heavily covered area: about 30%.

3.2 Simulation Model of a Nano Grid with PV Soiling Monitoring

In order to test different control strategies and to assess the usefulness of quantitative knowledge of PV modules soiling for maintenance policy optimization, we developed a simulation model of a DC NG in MATLAB/Simulink environment.

Power losses due to dust accumulation are quantified introducing the concept of Soiling Factor (SF). As defined in [146], the SF is the percentage loss in equivalent irradiance (G_{eq}) reaching the module due to the presence of dust accumulation on the PV module (Figure 3.9). The SF value can be estimated by means of the soiling sensor prototype presented (paragraph 3.1).

The model can simulate both islanded mode and grid-connected operation. Figure 3.10 shows the model's root level, where two independent nano-smart-grid (NSG) sub-models are instantiated. One (*NSG Dirty*) models the actual NG operation, with a PV plant subjected to dust deposition effects; the other (*NSG Clean*) is a reference NG model featuring perfectly clean PV modules. The *NSG* models run in parallel and are fed by the same scenario inputs, except for the soiling profile and the cleaning task activation trigger, which apply to *NSG Dirty* only.

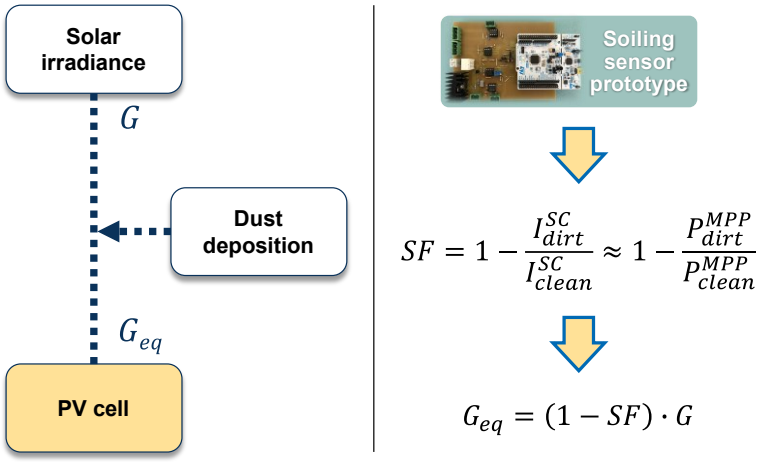

Figure 3.9: The SF concept (*left*) and how SF value is computed starting from data coming from the proposed soiling sensor (*right*).

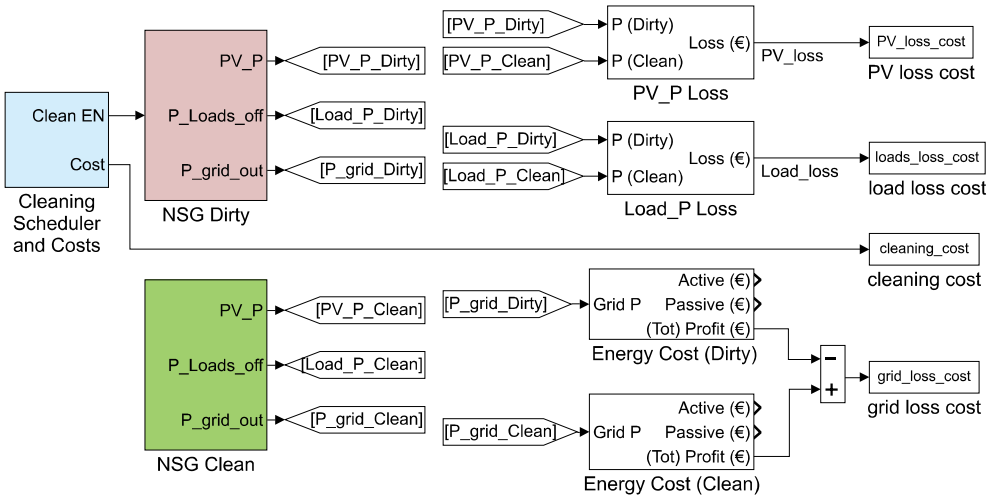

Figure 3.10: Root level of the Simulink model: two NG models run in parallel: the first one (*NSG Dirty*) takes into account the soiling effect, the second (*NSG Clean*) features perfectly clean PV modules.

The root level of the model (Figure 3.10) also features energy cost computation blocks yielding quantitative information about economic losses due to soiling effects; economic losses are evaluated differently, depending on the NG operation mode (islanded or grid-connected).

In the grid-connected scenario the focus is on the energy flow to and from the grid, and losses come from two main contributions: the reduction of energy exported to the grid, and the increase of energy import from the grid during shortfall phases. Starting from the power flowing out of the NG (P_{grid}), we define exported (P_{out}) and imported (P_{in}) power flows (3.1) which, integrated over time, yield the amounts of sold (E_{sold}) and purchased (E_{purch}) energy (3.2). The prices per kWh of sold and purchased energy (R_{sold}, and R_{purch}, respectively) are then used to compute the revenue for energy sold (C_{sold}) and the expenditure for energy purchased (C_{purch}) (3.2), and the overall energy cost (C_{tot}) for the NG (3.4).

$$P_{out} = \begin{cases} P_{grid}, & P_{grid} > 0 \\ 0, & P_{grid} \leq 0 \end{cases}, \quad P_{in} = \begin{cases} -P_{grid}, & P_{grid} < 0 \\ 0, & P_{grid} \geq 0 \end{cases} \tag{3.1}$$

$$E_{sold} = \int_0^{T_{stop}} P_{out}(t)\, dt\,, \quad E_{purch} = \int_0^{T_{stop}} P_{in}(t)\, dt \tag{3.2}$$

$$C_{sold} = R_{sold} \cdot E_{sold}, \quad C_{purch} = R_{purch} \cdot E_{purch} \tag{3.3}$$

$$C_{tot} = C_{sold} - C_{purch} \tag{3.4}$$

These equations are applied to both *Dirty* and *Clean NSG* models and, finally, the loss due to soiling is computed as:

$$C_{loss} = C_{tot}^{clean} - C_{tot}^{dirty} \tag{3.5}$$

When operating in islanded mode, losses come from the reduction of energy production due to soiling resulting in extra load shedding relative to the clean PV scenario. Thus, in this case, the power profiles of off-forced loads are integrated, the value of unsold energy is computed based on the price per kWh, and, finally, the economic loss relative to the clean-PV scenario is determined.

The cleaning task trigger and the total cost of cleaning interventions are generated and computed by the *Cleaning Scheduler and Costs* block, starting from cleaning frequency set-point input.

Our NSG model (Figure 3.11) represents a typical office environment, powered by PV plant, featuring an energy storage system and a few DC loads, such as LED lamps, laptops, printers, tablets and smartphones. Figure 3.11, in particular, shows

the *NSG Dirty* subsystem; *NSG Clean* differs from *NSG Dirty* in that the effects of dust deposition and cleaning interventions are neglected in the *Scenario* subsystem.

The *Scenario* block reads solar irradiance and load power profiles in workspace look-up-tables, as well as the values of ambient temperature and wind speed, and computes the SF as the integral over time of an average soiling rate that depends on the specific geographical location [147], [148]. SF saturates at 80%, and is reset at 0% every time a rising edge coming from *Cleaning Scheduler* is detected, signaling that a cleaning task has been carried out.

The *PV Plant* subsystem (Figure 3.12) contains both the PV array model and the MPPT control algorithm. The PV module behaviour is described starting from the 1-diode model equations, to which we added a static thermal model (see paragraph 2.2.4) and the effect of the SF on the equivalent irradiance hitting the cell. The 1-diode model parameters are computed starting from datasheet values. The MPPT controller can be enabled or disabled by the central control unit in order to achieve either MPPT or LPT operating modes. The latter is to be selected in islanded mode, when there is an excess of available energy, and storage is full. Under these conditions, the PV energy production is curtailed to satisfy load demand only. The irradiance input (G) is reduced according to the SF, by computing a complementary cleanness factor ($1 - SF$) (Figure 3.12).

The *Loads control block* implements a load shedding algorithm by assigning predefined priorities to loads. Knowing priority levels and load power profiles, according to the storage State of Charge (SoC) and PV power availability, loads are allowed to be on or disconnected.

The *Storage* subsystem (Figure 3.13) models a lithium cell battery pack with its charging and control units (see paragraph 2.2.5), considering, in addition, elementary thermal and aging behaviour Figure 3.14. The DP signal injects the excess power from the PV block into the grid when the battery is fully charged, or absorbs the PV power deficit from the grid when the battery is discharged.

Finally, power balance is computed by the *BUS Power Balance* block, which calculates the energy flowing to the storage unit based on PV power production and load consumption.

The *Control Unit* subsystem coordinates energy flows by determining whether enabling or disabling the MPPT mode. In grid-connected mode MPPT is always enabled and all loads are connected.

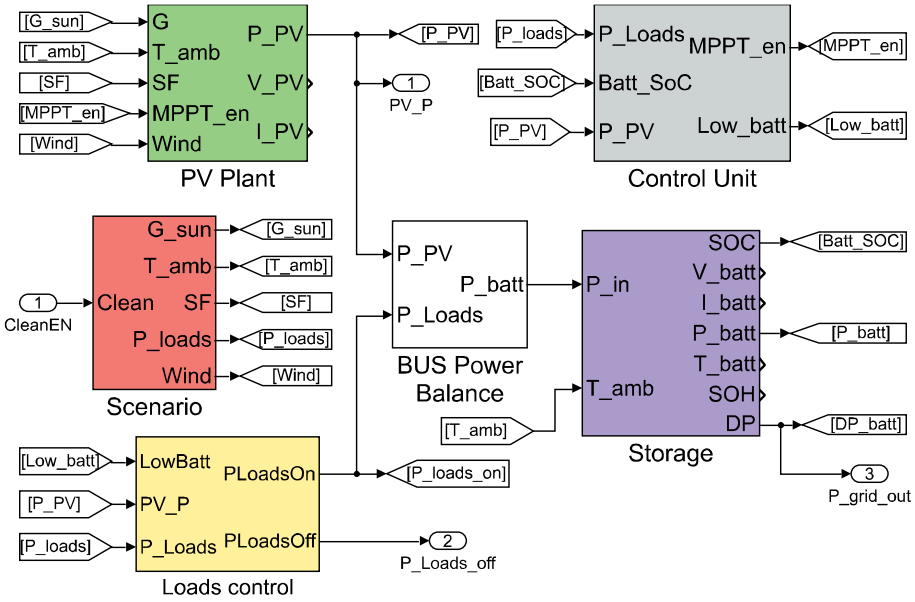

Figure 3.11: View of the NG sub-model (dirty case).

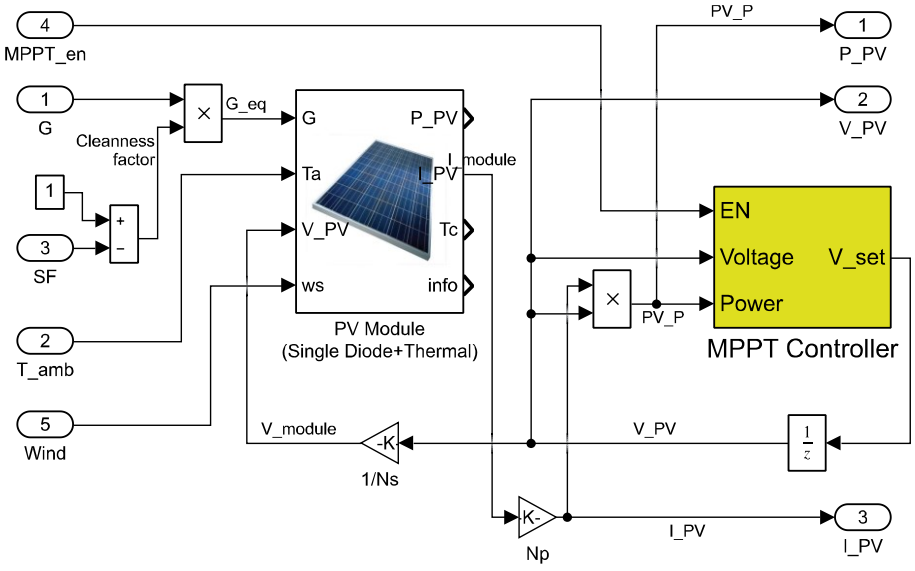

Figure 3.12: PV plant subsystem comprising PV module model, MPPT controller, and the SF effect on the irradiance level.

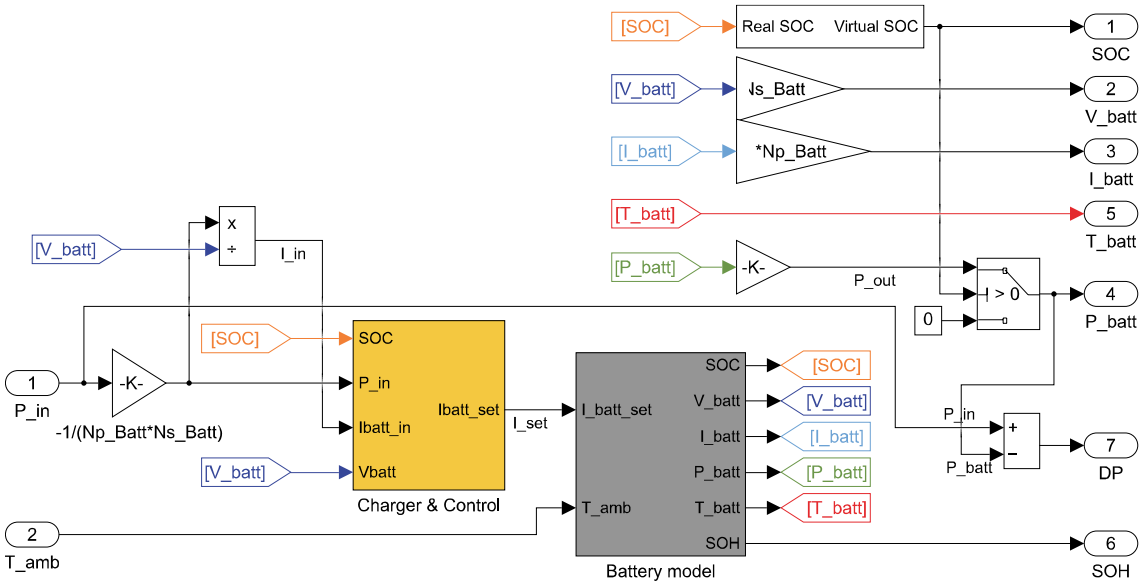

Figure 3.13: NG Storage subsystem consisting of the charger control and the battery model.

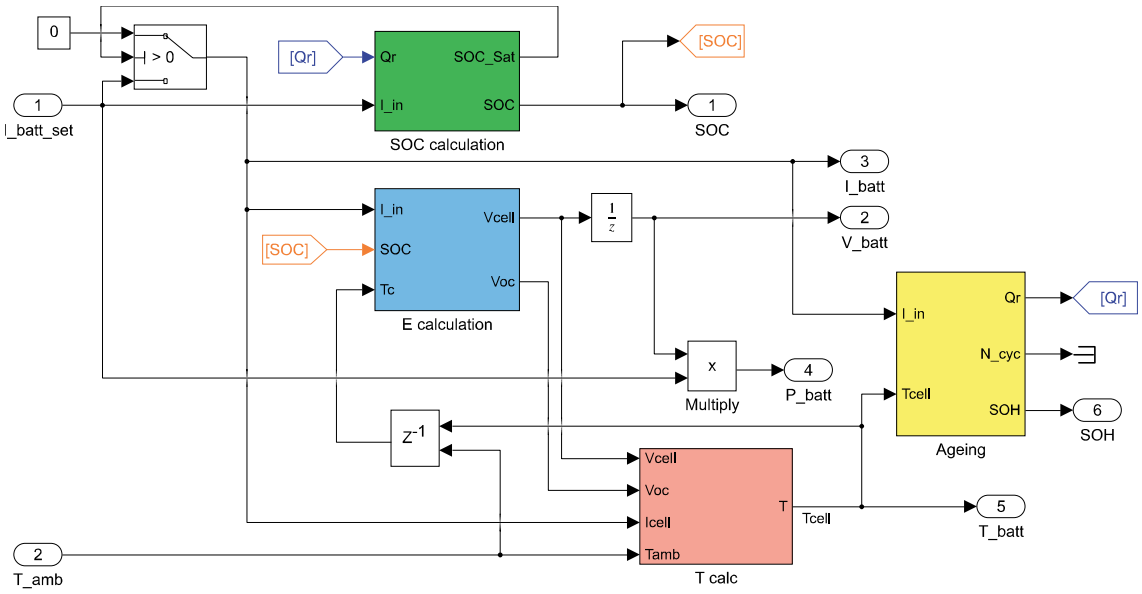

Figure 3.14: Detailed view of the battery model with SOC calculation (ampere counter), cell voltage calculation, cell temperature calculation and ageing estimation.

3.2.1 Simulation Results

Figure 3.15 gives an example of results for the NSG subsystem obtained under a 2-days long scenario under three different soiling conditions: SF = 0 (clean modules), 10%, and 30%. Irradiance and ambient temperature data from PVGIS [149] refers to Parma, Italy, Azimuth = 0°, Slope = 30°; typical load power profiles are from [150].

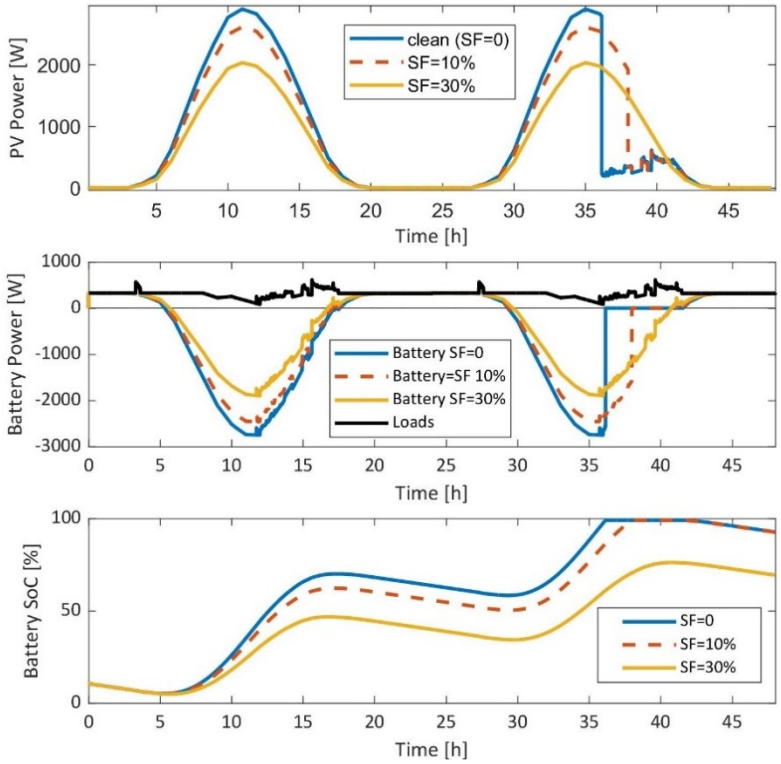

Figure 3.15: Simulation results obtained with 0 (clean PV array), 10%, and 30% SF. Irradiance profile from June 21-22 scenario in Parma (Italy). PV array peak power is 3 kWp, azimuth is 0° and slope is 30°.

Some parametric simulations involving the whole model have been carried out to evaluate the economic loss due to dust deposition. Different scenarios have been considered to take into account various economic conditions and SF ratios. Complete results are given in Table 3.2, while one specific result is detailed in Figure 3.16

Table 3.2: Results obtained with multi scenario parametric simulations.

Cleaning cost [€/intervention]	Energy price [€/kWh]		SF rate [%/year]	Optimal scheduling interval [years]	
	Buying	Selling		Grid conn.	Islanded
150	0.18	0.13	0.015	3	10
150	0.18	0.13	0.03	2	6
150	0.18	0.13	0.06	1.5	3.75
150	0.18	0.13	0.09	1	15.75
150	0.18	0.13	0.12	1	15.75
150	0.24	0.18	0.015	2.5	10
150	0.24	0.18	0.03	1.75	6
150	0.24	0.18	0.06	1.25	3.75
150	0.24	0.18	0.09	1	15.75
150	0.24	0.18	0.12	1	15.75
200	0.18	0.13	0.015	3	15.75
200	0.18	0.13	0.03	2.5	7.5
200	0.18	0.13	0.06	1.5	15.75
200	0.18	0.13	0.09	1.25	15.75
200	0.18	0.13	0.12	1	15.75
200	0.24	0.18	0.015	3	10
200	0.24	0.18	0.03	2	6
200	0.24	0.18	0.06	1.5	3.75
200	0.24	0.18	0.09	1	15.75
200	0.24	0.18	0.12	1	15.75
290	0.18	0.13	0.015	3.75	15.75
290	0.18	0.13	0.03	3	7.5
290	0.18	0.13	0.06	2	15.75
290	0.18	0.13	0.09	1.5	15.75
290	0.18	0.13	0.12	1.5	15.75
290	0.24	0.18	0.015	3	15.75
290	0.24	0.18	0.03	2.5	7.5
290	0.24	0.18	0.06	1.5	15.75
290	0.24	0.18	0.09	1.5	15.75
290	0.24	0.18	0.12	1	15.75

Referring to the case of a SF yearly increase rate of 0.06% (absolute), cost per cleaning intervention of 300 €, and energy price of 0.24 €/kWh and 0.18 €/kWh for buying and selling, respectively. In all scenarios, the final cost is evaluated just before the plant end-of-life (30 years). Table 3.2 shows that cleaning interventions are much more convenient in grid-connected NGs. In islanded mode, on the other hand, often PV and storage systems are oversized in order to minimize the occurrence of load shedding. Therefore, the PV plant often operates in LPT mode, and performance loss due to soiling has no significant impact. It should be noted that in this work the energy deficit (causing load shedding) was given the same economic value as that of energy purchased from the grid; this assumption has no universal value and should therefore be modified depending on the specific operational context.

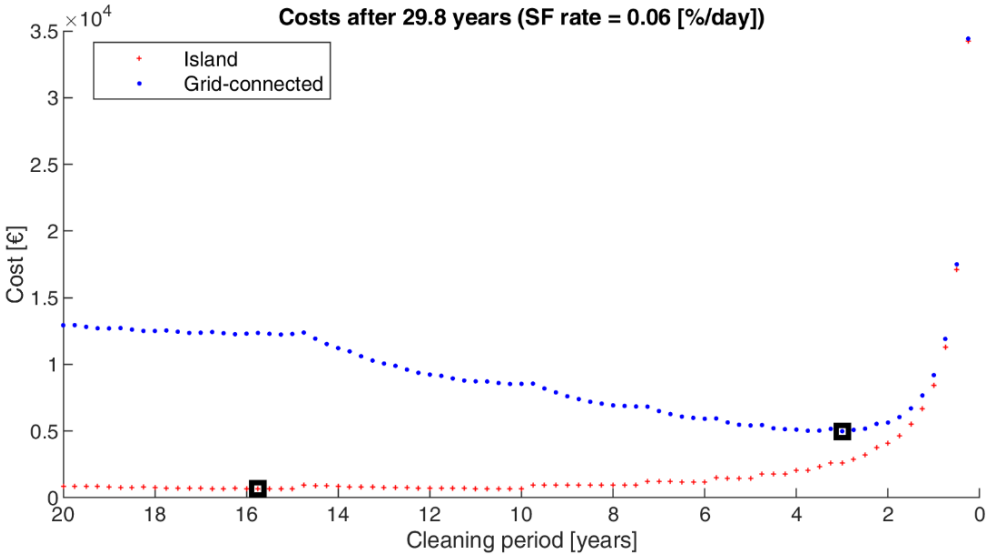

Figure 3.16: Detailed results of the scenario with 0.06%/year SF rate, cleaning intervention cost of 300 €, energy cost of 0.24 €/kWh and 0.18 €/kWh for selling and buying respectively. Results are shown for both islanded and grid-connected modes.

Concluding, the contribution of this chapter is to describe a new sensing approach to detect PV module performance degradation due to soiling. As shown by the simulation results, the proposed prototype can be integrated inside a NG in order to provide optimum cleaning intervention rates according to the operating scenario, differing by energy price, soiling rate, and grid operating mode. This will allow to reduce PV plant downtime due to cleaning interventions, and keep efficiency at its maximum, considering the best trade-off between maintenance cost and losses due to soiling.

Chapter 4

Modelling of a Nano Grid to Charge a Fleet of Industrial Electric Vehicles

The increased use of EVs in industrial environments (e.g., battery-powered forklifts) requires proper design of the grid architecture. Environmental and economic considerations encourage the use of RES to charge the vehicle fleet batteries [151]. However, the sizing of the facility power system, including the source nominal power and the capacity of the ESS, requires careful consideration of various parameters. From an environmental standpoint, increased self-sufficiency is mandatory to maximize the use of the green energy produced. However, if the primary energy source is a PV plant, maximizing self-sufficiency requires the installation of a suitably sized ESS, and increasing the ESS capacity is critical for reducing the energy exchange with the PG [152]. From an economic perspective, the optimum trade-off between the costs of initial investment (i.e., PV and ESS size), running costs and PG consumption must be determined [153]. From the technical and logistical standpoints, one must include considerations about the real estate footprint of the PV array and ESS, which critically depend on the size and location of the facilities. Finally, the EV charging strategy, namely, timing, frequency, and duration, must be defined considering the electric grid characteristics to reduce the cost of PG power consumption, increase the battery lifetime, and maximize the operability time of the EV [154].

In this chapter a novel approach to define the most suitable grid architecture based on behavioral PLECS modeling is presented [155]. Preliminary validation on the behavior of the model is carried out through tests on a reduced-scale system. The model considers the number of EVs, initial investment costs, PG consumption costs, CO_2 footprint, and EV working time requirements. Through simulations, the optimum capacity of the PV and ESS installations can be determined by considering economic, technological, or environmental aspects.

4.1 Overview of the model

Figure 4.1 shows the grid architecture of the simulation model considering a case study featuring a fleet of 10 EVs, each equipped with a 10.5 kWh battery, and 2 charging stations supplied by a PV plant supported by an ESS and by the PG. the EVs fleet is governed by a job scheduler assigning jobs and recharging actions. The default schedule consists of working phases of about 2 hours alternated with 5-minute charging phases (exceptions are made when the state of charge of an EV is too low). Work cycles and durations are assigned in a pseudo-random way.

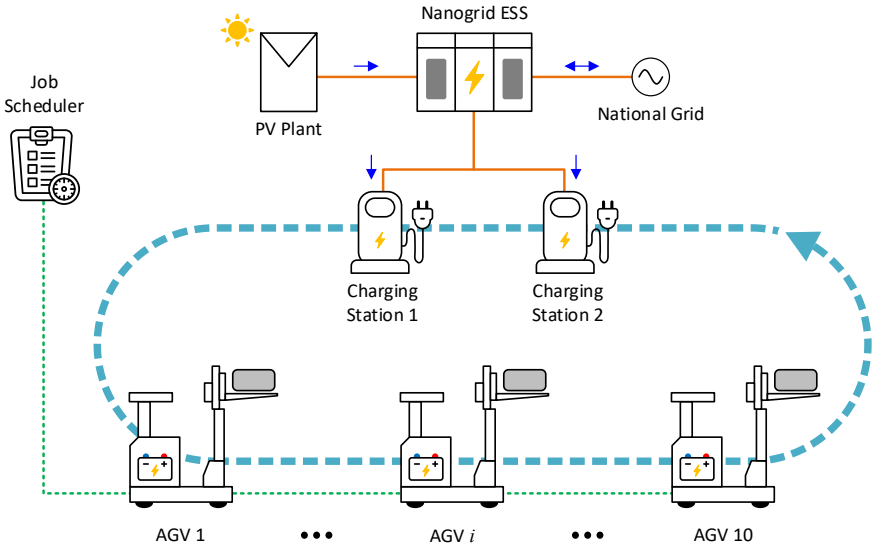

Figure 4.1: Grid architecture of the simulation model.

We choose PLECS as simulation tool, in anticipation of carrying out HIL simulations using a Plexim RT-BOX for model validation. The model consists of 5 main blocks (Figure 4.2): a subsystem (*10 AGVs*) that runs the models of 10 vehicles in parallel, a subsystem modelling the job scheduling algorithm, the model of the PV plant, alongside with its MPPT controller, the BESS and an energy meter to estimate the global energy consumption from the PG and the operating costs.

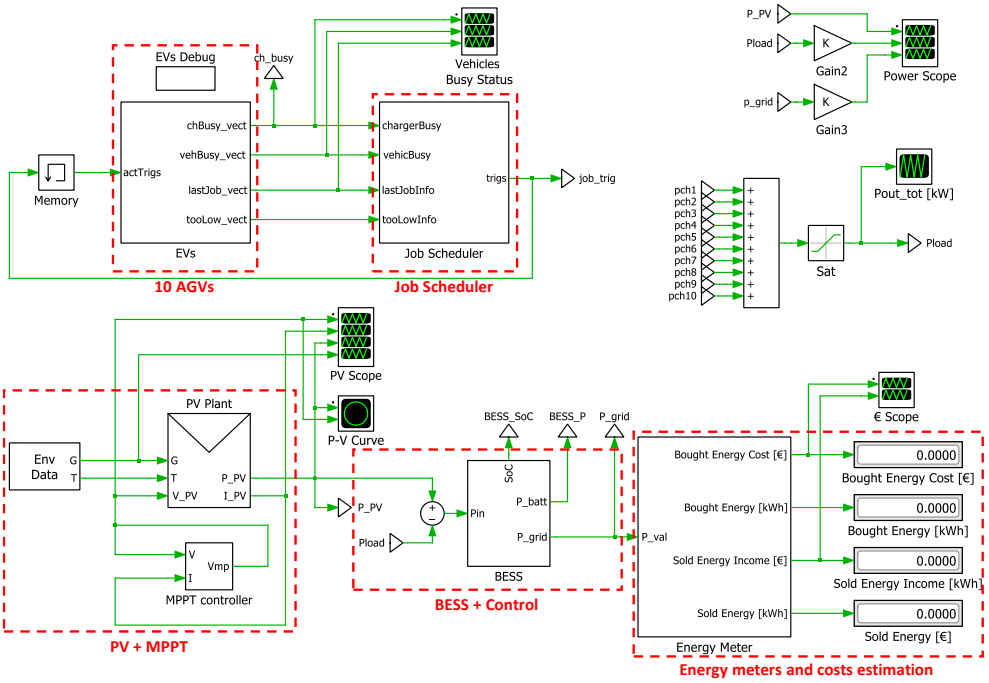

Figure 4.2: Global view of the model implemented in PLECS simulation environment.

4.1.1 Vehicles and Charging Stations

Vehicles are modelled by means of a FSM (Figure 4.3) coupled with the model of a battery as shown in Figure 4.4. To simplify the model, each vehicle contains both the logic underlying the duration of the jobs and the one underlying the charging station. The two algorithms are mutually selected depending on the commands coming from the job scheduler.

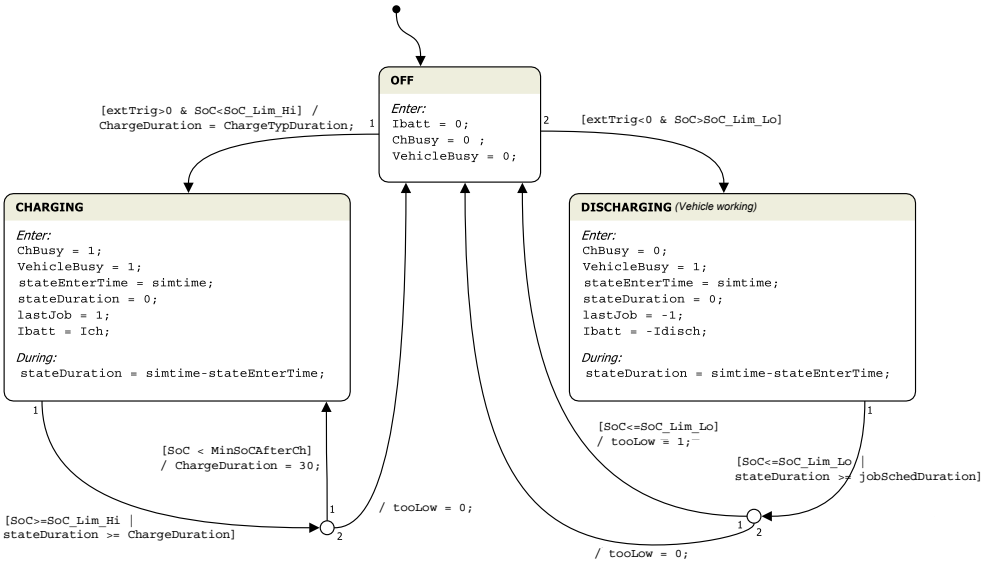

Figure 4.3: FSM modelling the behavior of the EV.

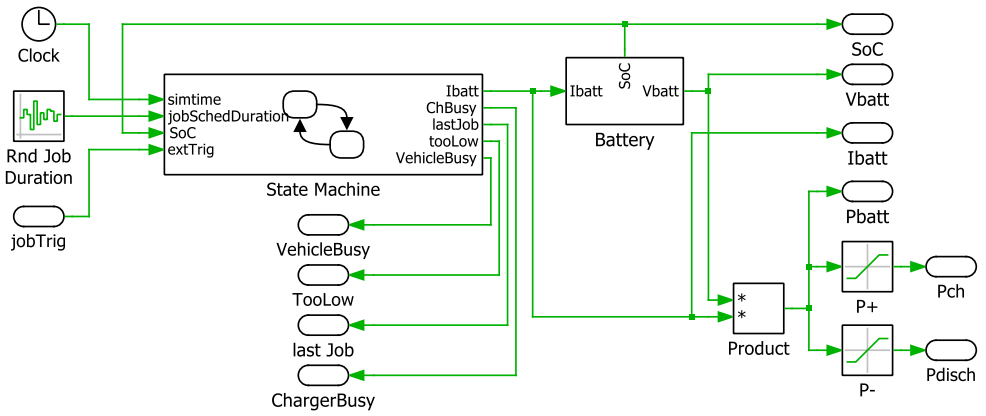

Figure 4.4: PLECS model of a vehicle.

A vehicle can be in three different states. The initial one is the *off* state in which, the vehicle is parked, waiting to receive a *trigger* from the job scheduler. If a *job trigger* is received the FSM sets the vehicle as *busy* (*VehicleBusy* goes high) and keeps it in this state for a random period of 2 ± 0.5 hours. An exception is made if the vehicle reaches a state of charge (SoC) below 20% and it is unable to complete

its work: in this case the *TooLow* signal is asserted to properly notify the job scheduler. When the job is completed successfully, *VehicleBusy* is reset, and the vehicle is ready the receive a new *trigger*. If a *charging trigger* is received the *ChargerBusy* flag is asserted (together with the *VehicleBusy* signal) allowing the job scheduler to count the number of vehicles under charge (thus virtually the number of free charging stations). Then the battery is fast-charged at constant current rate for 5 minutes. An extension on the charging time is allowed in case, after 5 minutes, the SoC is still below the minimum threshold of 80%. (See paragraph 2.2.5 for details about the model of the battery.)

4.1.2 Job Scheduling Algorithm

The job scheduler is designed to monitor the global state of the system, namely the state of the vehicles and the number of available (or busy) charging stations.

At each iteration of the simulation, the algorithm checks whether there are any free vehicles. If at least one charging station is available, foreach free vehicle, if its last performed action was carrying out an assigned job, it is triggered for charging its battery. Then the algorithm extracts a random number (limited to the total number of vehicles in the fleet) and if the corresponding vehicle is free, and its SoC is above a minimum safe value, it is triggered for a new job. Figure 4.5 shows the job scheduler model. Finally, through the subsystem mask, it is possible to specify the working hours and days, outside of which no new action is triggered.

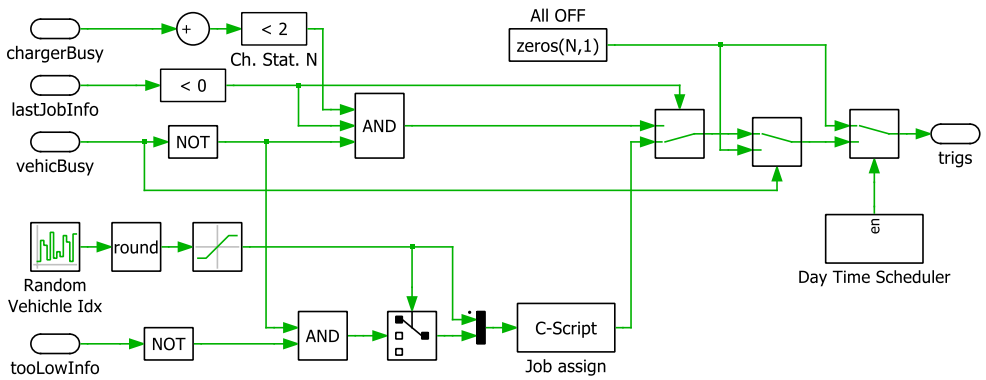

Figure 4.5: Job Scheduler implementation in PLECS.

4.1.3 Power Supply System and Costs Estimation

The power required to charge the EVs is supplied by a PV plant supported by a BESS and by the connection with the PG.

The PV array production is obtained by combining in series and parallel the model of a PV module described by the 1-diode equivalent circuit equations (see paragraph 2.2.4). The perturb & observe MPPT algorithm (see 2.2.4.2) is implemented to continuously extract the maximum available power from the PV plant. Observing the variation in PV voltage and power output the algorithm determines a new value of voltage to set as input of the 1-diode PV model. Solar irradiance and ambient temperature datasets are from the PVGIS database [149].

The BESS is modelled (similarly to the PV plant) starting from empirical equations representing the behavior of a Li-ion battery unit, the voltage and current of which are suitably scaled (series and parallels) to obtain the entire storage unit (see 2.2.5).

The system is operated to try to minimize the amount of energy exchanged with the power grid. The power entering (positive) or supplied by (negative) the BESS is computed by subtracting the value of power consumed by the loads from the PV power. If the BESS is in *full* SoC and there is an excess in energy production, the difference of power is sold to the PG. Conversely, if the BESS is in *low* SoC and the PV production is not able to satisfy the load demand, the required amount of energy is bought from the PG.

The total operating cost after one year ($C_{tot,1y}$) is obtained as in (4.1), (4.2) and (4.3):

$$C_{E,1y} = U_E^{bought} \int_0^{1y} P_{bought} dt - U_E^{sold} \int_0^{1y} P_{sold} dt \tag{4.1}$$

$$C_{PV}^{inst,1y} = \frac{P_{PV}^{pk} \cdot U_{PV}}{20} \quad ; \quad C_{BESS}^{inst,1y} = \frac{Q_{BSS}^{tot} \cdot U_{BESS}}{10} \tag{4.2}$$

$$C_{tot,1y} = C_{E,1y} + \left(C_{PV}^{inst,1y} + C_{BESS}^{inst,1y}\right) \tag{4.3}$$

The power exchanged with the PG is split in positive (P_{bought} $[kW]$) and negative (P_{sold} $[kW]$) components and integrated over time to obtain, the amount of energy sold and bought to/from the PG (integrals in (4.1)). Then, proper €/kWh prices

(U_E^{bought} and U_E^{sold}) are applied to each component, obtaining the energy cost balance ($C_{E,1y}$ [€]). Finally, we add the installation costs of the PV and of the BESS plants ($C_{PV}^{inst,1y}$ and $C_{ESS}^{inst,1y}$), computed from per-unit of peak-power (U_{PV} $[\frac{€}{kW_p}]$) and energy-capacity (U_{BESS} $[\frac{€}{kWh}]$) costs, considering the actual size of each plant (P_{PV}^{pk} $[kW_p]$ and Q_{BSS}^{tot} $[kWh]$) and the typical plant lifetime (20 years for PV and 10 years for BESS).

In addition, from an environmental standpoint, it is possible to estimate the amount of CO_2 produced due to the energy bought from the PG by applying a proper emission factor ($\frac{kg_{CO_2}}{kWh}$) computed in [112].

4.2 Reduced-scale Prototype

Before performing yearlong simulations, to find the optimum mix between PV and BESS size minimizing the system costs, we designed and setup a reduced-scale DC prototype to validate the behavior of the model. To reduce the prototyping time, we deployed all the control logic of the system to the PLECS RT Box 1 HIL simulator.

Figure 4.6a shows the block diagram of the prototype, while Figure 4.6b is the test bench implemented. The PV plant is emulated by means of a power generator with built-in solar array simulator which is interfaced with the BESS (emulated by *Battery 1*) by means of a DC/DC converter (*U1*). *Battery 1* is also intended to fix the common DC-bus voltage (V_{BI}). The behavior of an EV is emulated by means of a battery (*Battery 2*), representing the onboard storage of the vehicle, that can be (according to the given fleet scheduling pattern) charged by means of the DC/DC converter *U2*, or discharged in a controlled fashion (emulating a working cycle) by means of the converter *U3* closed on a power resistor (R_L). The HIL simulator is responsible for generating the Pulse-Width-Modulation (PWM) control signals for the converters. *U1* is controlled by the MPPT algorithm, while *U2* and *U3* are mutually activated according to the job scheduling algorithm and operated by a Proportional-Integrative (PI) controller, closing the proper voltage and current loops.

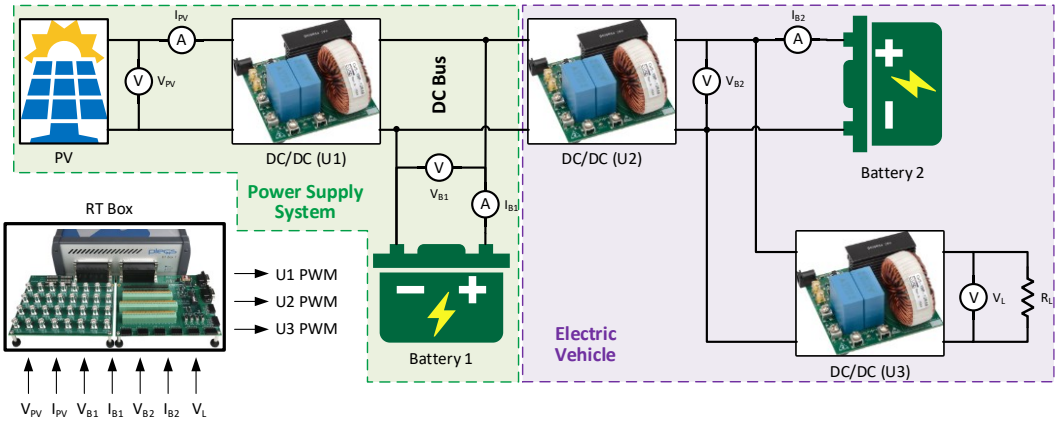

(a)

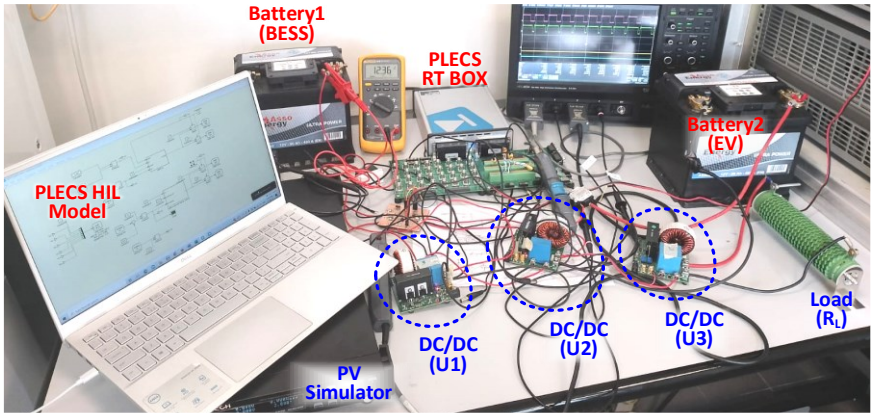

(b)

Figure 4.6: Reduced-scale system prototype: a) the block diagram, b) the test bench setup.

Figure 4.7 shows the simulated power profiles for three values of the PV plant capacity, with a working scenario of about 8 h per day. Parametric simulations are used to estimate the optimal size for PV and BESS installations. For several PV-BESS combinations, we computed the total economic cost after one year of operation, including the installation costs and the energy balance costs. The model allows the identification of the PV-ESS combination minimizing the system operational cost. Table 4.1 shows the results obtained considering a scenario where the EVs are operated 24 h a day. In this case the optimal combination can be identified with the solution of a 59 kWp PV size and a 155 kWh ESS capacity.

Table 4.1: 1-year simulation results considering a 24 h/day operating scenario for the EVs.

PV size [kWp]	ESS size [kWh]	$C_{PV}^{inst,1y}$ [10^3 €]	$C_{BESS}^{inst,1y}$ [10^3 €]	$C_{E,1y}$ [10^3 €]	$C_{tot,1y}$ [10^3 €]	CO_2 emissions [kg]
20	0	0.50	0.00	17.71	18.21	6.43
20	52	0.50	1.76	15.88	18.14	5.53
20	78	0.50	2.64	15.84	18.98	5.52
20	104	0.50	3.52	15.80	19.82	5.52
20	155	0.50	5.25	15.75	21.50	5.51
20	207	0.50	7.01	15.63	23.14	5.50
39	0	0.98	0.00	13.56	14.53	5.78
39	52	0.98	1.76	10.79	13.52	4.39
39	78	0.98	2.64	9.60	13.21	3.80
39	104	0.98	3.52	8.55	13.05	3.28
39	155	0.98	5.25	7.15	13.38	2.60
39	207	0.98	7.01	6.93	14.91	2.52
59	0	1.48	0.00	10.09	11.57	5.48
59	52	1.48	1.76	7.10	10.33	3.98
59	78	1.48	2.64	5.77	9.89	3.32
59	104	1.48	3.52	4.50	9.49	2.69
59	155	1.48	5.25	2.53	9.25	1.70
59	207	1.48	7.01	1.99	10.47	1.47

Concluding, in this chapter we have shown a novel approach to define the most suitable grid architecture to charge EV fleets in the industrial environment using system-level models implemented in PLECS simulation environment.

Models has been validated through a reduced-scale experimental test bench. The proposed approach allows to define different EVs operation scenarios and to obtain the optimum capacity of the PV and ESS installations by considering economic, technological, or environmental aspects.

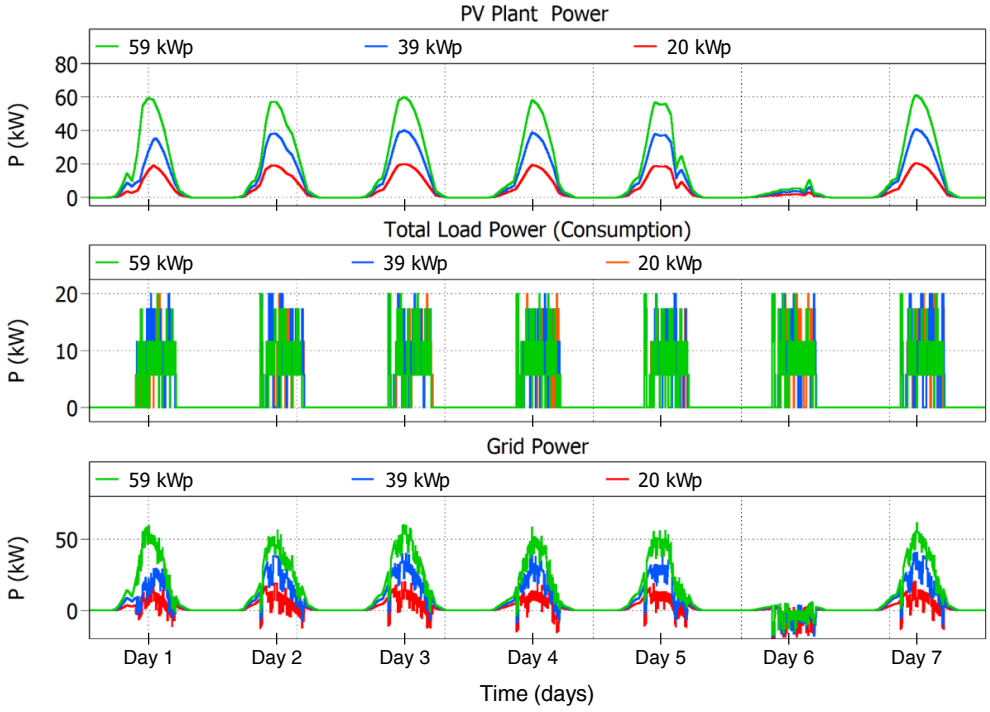

Figure 4.7: Power profiles of a 1-week simulation. Results for 8h/day EVs operation scenario considering 3 different PV installations: 59 kWp, 39 kWp, 20 kWp.

Chapter 5

Behavioral Modeling of Power Devices for System-level Simulations for Automotive Applications

In this chapter, a system simulation approach to model the behavior of PROFET™ devices [156] for automotive applications is presented. This work has been carried out in collaboration with Infineon Technologies Austria, Automotive Division, Villach, Austria.

PROFET™ (protected FET) is the commercial name under which Infineon commercializes high-side power devices featuring built-in protections including over-temperature and over-current, plus additional diagnostic features such as current sensing. These fast electronic protected switches can detect a hazardous condition and respond in quickly and reliably. This allows to enhance the safety of the automotive distribution system where robustness against different types of unexpected events such as electrical overloads and short-circuit events is a mandatory feature. In fact, a short-circuit that is not interrupted fast enough could generate drastic overheating of cables, potentially leading to a permanent damage of harnesses and the involved electrical components, or even to a fire event in the worst-case scenario.

System integrators need accurate models that can simulate the product's behavior, usually available as SPICE models. However, it is also necessary to investigate alternative approaches to the modelling of such products, especially when the focus is on the simulation of a mission profile, possibly with changing conditions during lifetime (e.g., ambient temperature, overload situations, etc.). Hence, a simplified modelling approach is required to keep the simulation time within reasonable bounds [157], [158].

In this work PLCES simulation environment [159] is the tool chosen to design the behavioral model for the PROFET™ device thanks to its simplified approach to the modeling of solid-state switches and the possibility to graphically design finite state machines (FSM) useful in modeling the behavior of the integrated control logic [160].

The system applications presented in this chapter are relatively simple, but the modelling concept can be applied to more extensive and modular systems. Such a modelling approach is of particular importance during the early concept development phase of a product or a system, especially when physical prototypes are not available. Virtual prototyping is especially advantageous to evaluate new concepts for the product itself, or to check how the product would behave in more complex systems [161], [162]. In particular, early detection of pitfalls, block interdependences and topology optimization can be performed relying on behavioral models, even in the absence of experimental data. Behavioral modelling gives the user flexibility to replicate the relevant behavior of the system of which the considered product will be a part, while neglecting aspects that are not relevant to the problem at hand, thus making the model lean and quick to simulate.

5.1 PROFET™ Behavioral Simulation Model

Figure 5.1 shows the block diagram of a dual-channel PROFET™ product. A PROFET™ device is a high-side power device, consisting of an integrated power stage (or more, in case of multi-channel devices) and the logic necessary to operate it correctly. Since the focus is on the behavioral modelling of the product, certain

features closely related to the electrical domain (e.g., gate control, charge pump) can be neglected in PLECS, where the gate is driven by a logic signal (high/low).

The main features to be included in the model are:

- over-temperature protection, including basic thermal modelling of the thermal sensors;
- over-current protection;
- output voltage limitation (namely, Zener clamping);
- internal state diagram;
- the power stage.

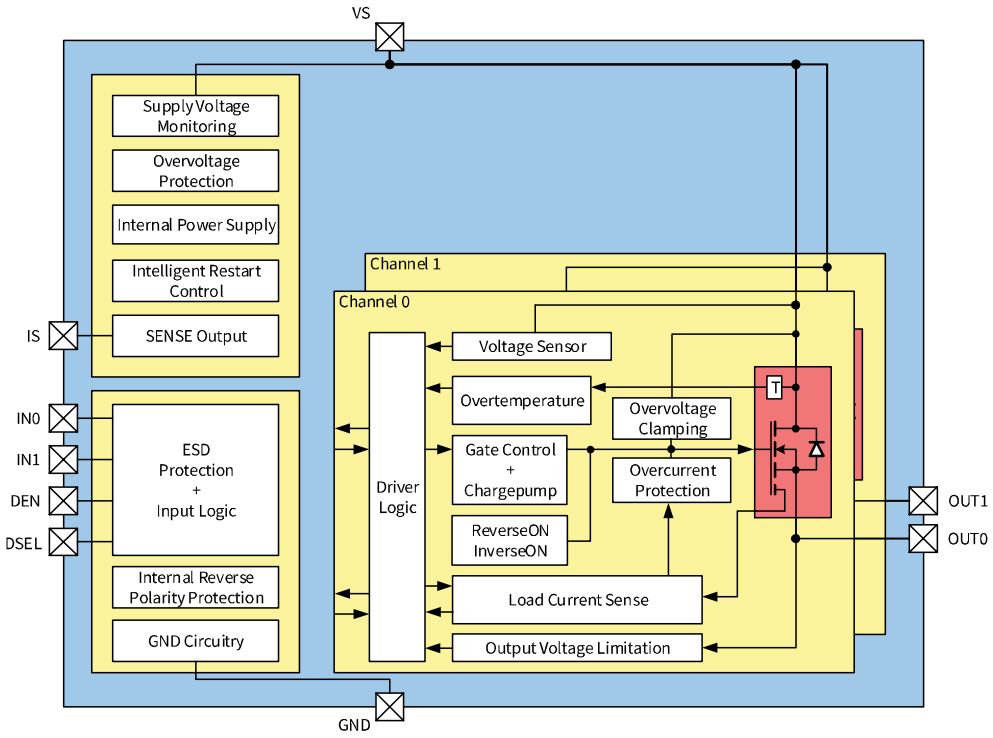

Figure 5.1: Block diagram of a PROFET™ device [163].

The model implemented is composed of four subsystems (Figure 5.2): the input state machine (with the FSM), the power stage, the thermal model, and the fault-

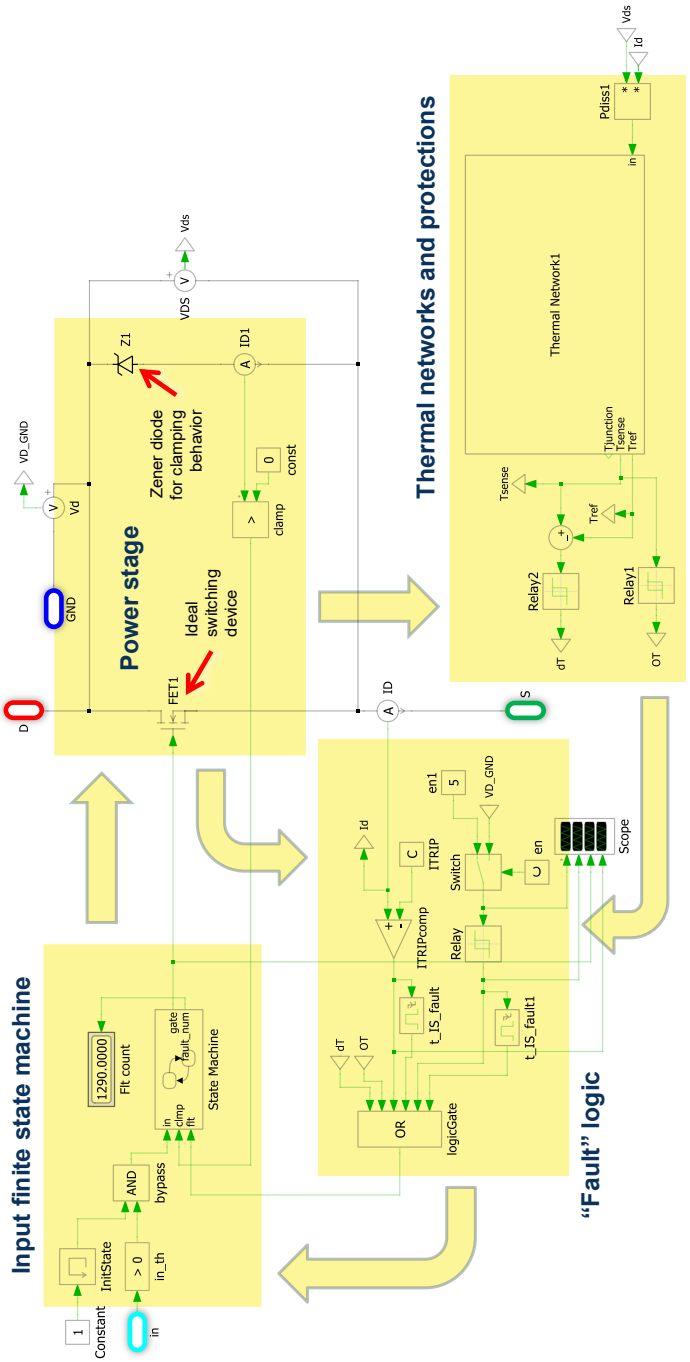

Figure 5.2: Global view of the model implemented, divided into 4 main parts: the input FSM, the power stage, the thermal model, the fault handling logic.

handling logic. The approach shown in this chapter is general, and it should be understood as an investigation of the modelling possibilities, not necessarily related to a particular product.

5.1.1 Input Control Logic

Since the device keeps memory of its operational state in order to properly detect and manage faulty conditions, an FSM is introduced in the model as the core of the integrated control logic behavior. The FSM presents three inputs (Figure 5.3): the user control signal (*in*), the clamping condition signal (*clmp*), and the fault condition signal (*flt*). Outputs of the subsystem are the power stage gate control signal (*gate*) and a fault condition counting number (*fault_num*).

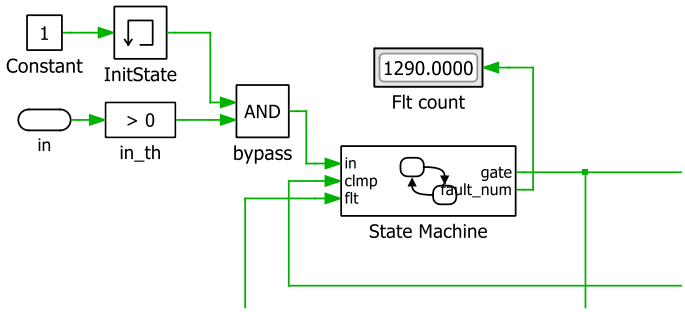

Figure 5.3: Particular of the input state machine subsystem.

At the first simulation step, the FSM user input signal is kept at zero through a memory block, connected with the user control signal through an AND gate logic block. This improves convergence at the first simulation step.

Figure 5.4 shows in detail the FSM, composed by four states: *Off* state, *On* state, *Fault* state and *Clamping* state.

Starting from the *Off* state, when the user input *in* goes to 1 with no fault and no clamping signal condition, the FSM moves to the *On* state, setting the output *gate* to 1. In this state, two possible signal transitions can happen: the input could change from 1 to 0, still with no fault and no clamping conditions, therefore the FSM moves to the *Off* state. Otherwise, a fault signal transition from 0 to 1 could move the FSM

to the fault state. In both cases, the gate output signal is 0. In both *Off* state and *Fault* state, when the clamping signal becomes 1 the FSM moves to the *Clamping* state.

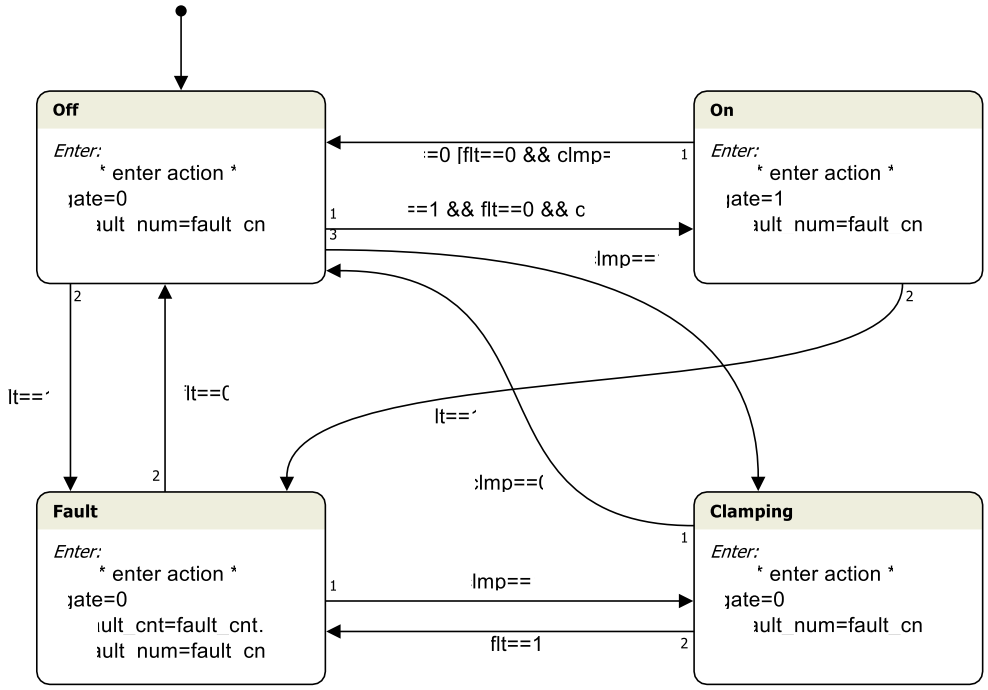

Figure 5.4: PROFET™ FSM state diagram in PLECS.

To turn on the power stage, the FSM necessarily moves through the *Off* state. Therefore, latch or automatic restart behavior in case of fault can be modeled by changing the verification of the user input, which can be done through either transition detection or a condition verification. In Figure 3, the *in* signal is written between square brackets, meaning that the device will restart automatically as long as the signal is kept high. Therefore, the restart is defined by the external fault signal. After a fault condition vanishes, the fault signal can be kept high for a determined amount of time. This allows to restart the PROFET™ with a different rate in relation to the detected fault. Instead, if the *in* signal is checked outside the brackets, the input has to be lowered and then raised back to 1 for the *Off* to *On* transition, obtaining a latch behavior of the PROFET™.

5.1.2 Power Stage

The behavior of the power stage of the product is described (Figure 5.5) by means of an ideal switch (*FET1*) with a Zener diode (*Z1*) connected in antiparallel. The model considers the on-resistance of the PROFET™ (included in *FET1*) and the body-diode and clamping behaviors (by means of *Z1*). If the *FET1* is turned off, *Z1* allows the current discharge and fixes V_{DS} at the clamping voltage. When $I_D > 0$, the clamping condition is verified by a comparator block and used as input signal for the FSM control.

The voltage between drain and ground is sensed as well to check for the undervoltage fault condition.

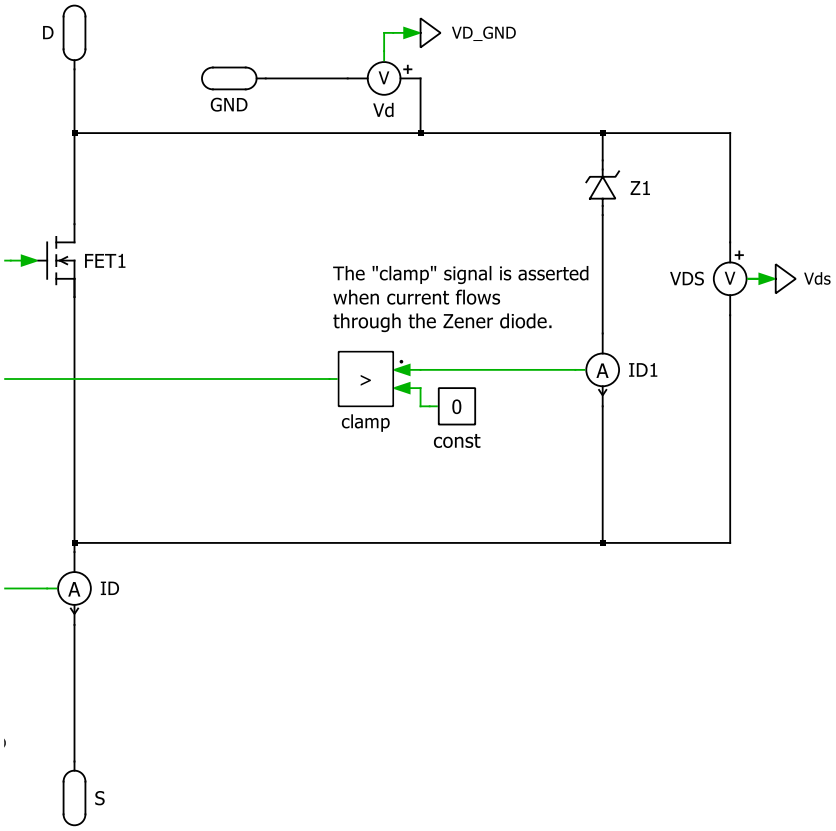

Figure 5.5: Power-stage model in PLECS.

5.1.3 Thermal Model and Protections

The thermal section of the model is shown in Figure 5.6. It consists of three RC Forster thermal networks: the first one for the estimation of the junction temperature (*Tjunction*) of the built-in DMOS (only for debug purposes), the second one (*Tsense*) estimates the temperature of the chip at the power stage side, while the third one (*Tref*) estimates the temperature of the chip at the logic side.

Input of the thermal block is the instant power dissipation on the DMOS, given by $V_{DS} \cdot I_D$. The DMOS temperature sensor model output is connected to a relay block (*Schmitt trigger*) with thresholds of 150 °C and 180 °C (*Relay1*), which generates an *OT* fault signal. Furthermore, the difference between the sense temperature and the reference temperature of the PROFET™ is checked with a hysteresis from 40 °C to 80 °C, generating a *dT* fault signal (*Relay2*).

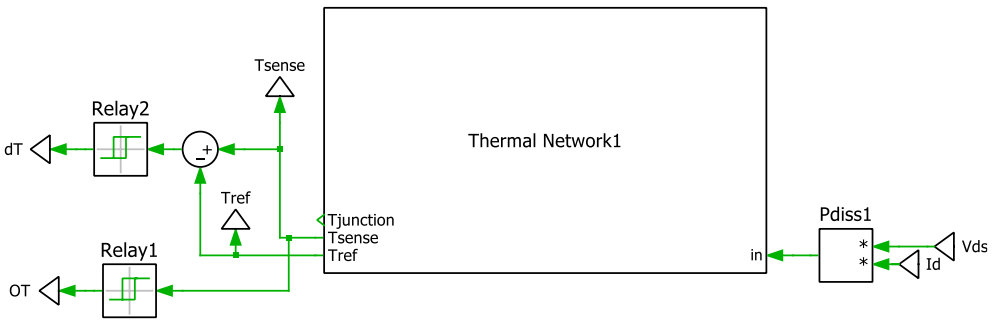

Figure 5.6: Thermal network and protections subsystem.

5.1.4 Fault Detection Logic

The fault logic subsystem shown in Figure 5.7 considers all the different fault signals from the power stage and the thermal subsystem. The output of the *OR logic gate* is sent to the FSM (*flt*). I_D is compared with the ITRIP value and an overcurrent fault signal is generated if $I_D > ITRIP$. When the undervoltage fault is enabled, the $V_{D\text{-}GND}$ voltage is connected to a hysteresis block, and a fault signal is sent to the FSM when the voltage decreases under 3.1 V. For the overcurrent and undervoltage faults, a *monoflop* block of PLECS is used to maintain the fault condition for a certain amount of time after the condition is terminated.

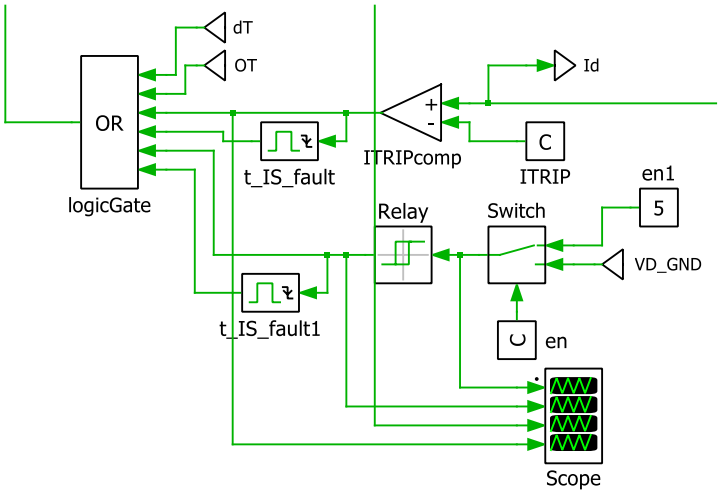

Figure 5.7: Fault logic subsystem consisting of overcurrent protection, undervoltage detection and thermal protections.

5.2 Auxiliary Components Modeling

To test the model of the PROFET™ device under realistic circuit configurations, we modeled in PLECS additional components, namely, the model of DC distribution cables and, as a typical load, a heated filament bulb lamp.

5.2.1 DC Automotive Wire

The cable contribution to the global system robustness cannot be neglected for many reasons, especially when fault events are considered. From the electrical and operating point-of-view, potentially dangerous behaviors are induced by voltage drops. Cable resistive and inductive effects are responsible for these drops. Furthermore, from a safety point-of-view, cable heating must be modeled. Overheating issues can be checked, and the cable resistance per-unit-length (*pul*) can be changed in relation to the chosen cable. Figure 5.8 shows a possible PLECS implementation where simple modeling approach for both the electrical and thermal behavior of a DC cable has been considered [164].

The electrical part of the model consists of an elementary R-L series circuit featuring *pul* values for the specific type of cable; *pul* values are multiplied by the particular cable length. The thermal behavior of the cable is modelled by a single stage RC Foster thermal network. The heat flow in W/m Q_{wire} is computed starting from the value of the current flowing in the cable according to equation (5.1):

$$Q_{wire} = R_{pul} * I_{wire}^2 \tag{5.1}$$

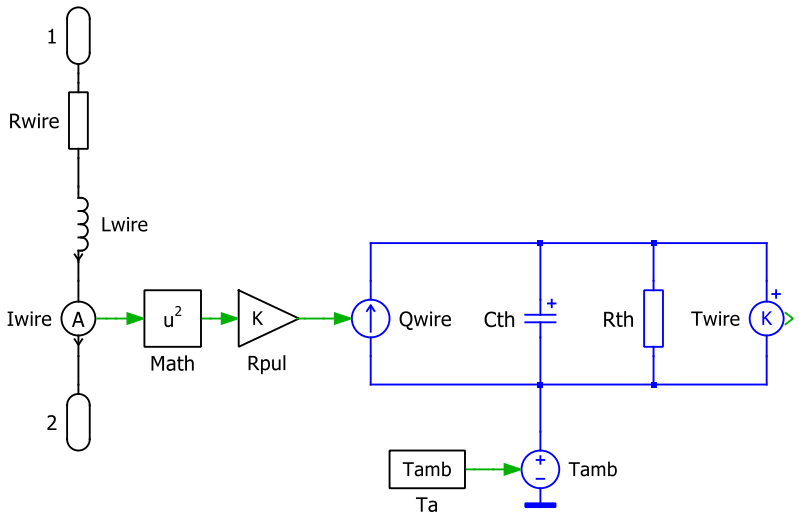

Figure 5.8: Simple thermal and electrical model for a DC cable.

5.2.2 Heated Filament Bulb Lamp

Legacy electromechanical components, such as relays and passive protections like fuses, can be replaced by PROFET™ devices for driving loads turn-on and turn-off. A typical load is represented by heated filament lamps [165]. This kind of light sources are characterized by a strong dependence between the electrical and the thermal behavior. In particular, the filament equivalent resistance is related to its temperature by a positive coefficient.

The resulting behavior consists in high inrush currents at cold temperature (at turn-on), decreasing to the nominal rated value as the filament reaches the typical operating temperature of a few thousand Kelvin. The model presented in [166] has

been chosen for the PLECS implementation. It consists of a thermal network with two thermal capacitances, as shown in Figure 5.9.

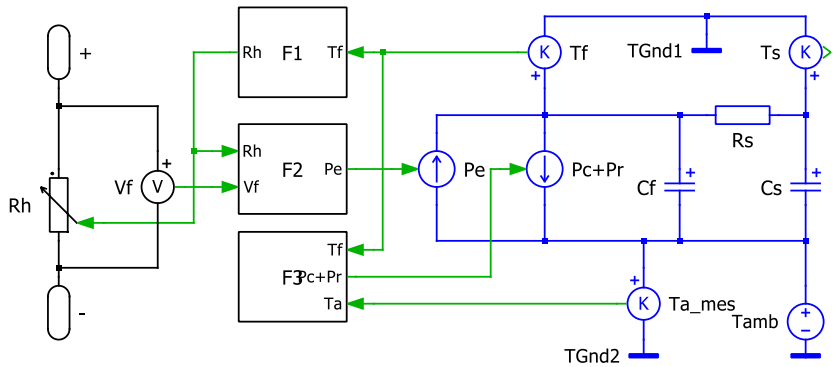

Figure 5.9: Heated filament bulb lamp model in PLECS.

C_f represents the thermal capacitance of the filament, while C_s is the lamp support thermal capacitance. T_f and T_s represent the filament and lamp support absolute temperatures, respectively. There are three power contributions: the joule effect electric power contribution P_e, the convection (P_c) and radiation (P_r) power contributions. The joule effect power P_e is computed by the subsystem *F2* according to equation (5.2).

$$P_e = \frac{V_{in}^2}{R_h} \tag{5.2}$$

Convection and radiation are packed as a single negative source and computed through the empirical expression related to Fourier and Stefan-Boltzmann laws of equation (5.3).

$$P_c + P_r = a\left(T_f - T_a\right) + b\,T_f^4 \tag{5.3}$$

The coefficients, a and b, have been empirically extracted in [166] for an H4 automotive lamp.

A comprehensive expression for the thermal model is given by the system of equations (5.4).

$$\begin{cases} \frac{dT_f}{dT} = \frac{1}{C_f}\left[P_e - (P_c + P_r) - \frac{T_f - T_s}{R_s}\right] \\ \frac{dT_s}{dT} = \frac{T_f - T_s}{R_s C_s} \end{cases} \tag{5.4}$$

Finally, the electrical behavior is modelled by a variable resistor, the value of which is obtained by implementing equation (5.5) in subsystem *F1*:

$$R_h = R_c \left(\frac{T_f}{T_c}\right)^{1.2285} \tag{5.5}$$

R_h and T_f are the estimated resistance and temperature of the filament, while R_c is a resistance reference value measured at cold conditions, at the temperature T_c.

5.3 Simulation Results

In this paragraph simulation results are shown involving the PROFET™ device behavioral model. The simulations are focused on typical application scenarios at both normal and faulty operating conditions.

Figure 5.10 shows the first simulation scenario presented. It consists of a PROFET™ driving a bulb lamp. Realistic conditions are modeled introducing two distribution cables: a 2-meter-long supply-side wire (20 mΩ, 2 µH) and a 10-meter-long load-side wire (100 mΩ, 10 µH).

Figure 5.12 shows simulation results of the turn-on behavior with a lamp load. Initially, the current quickly increases up to 45 A and the temperature T_{sense} on the PROFET™ device increases due to the current inrush; T_{ref} increases, too, but with a slower time constant. Then, in about 200 ms, the current approaches its nominal value corresponding with the lamp filament steady-state temperature. In this scenario no faults are triggered.

The second scenario, shown in Figure 5.11, consists of a short circuit event with the device automatic restart configuration.

Simulation results are summarized in Figure 5.13. Because of the short circuit, when the device is switched on, the current starts increasing and it quickly reaches the ITRIP threshold of 80 A (red line in Figure 5.13). In this case the ITRIP

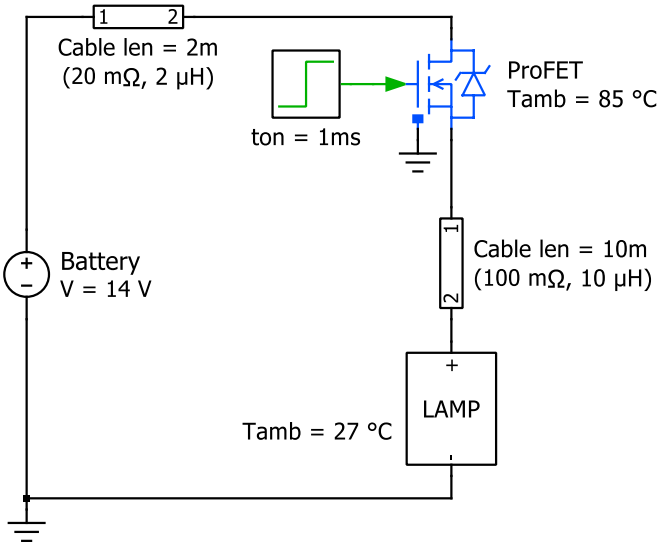

Figure 5.10: Typical load driving application scenario.

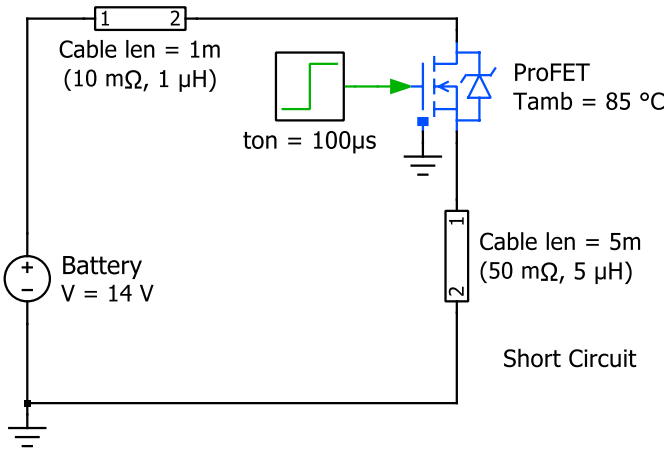

Figure 5.11: Short circuit fault scenario.

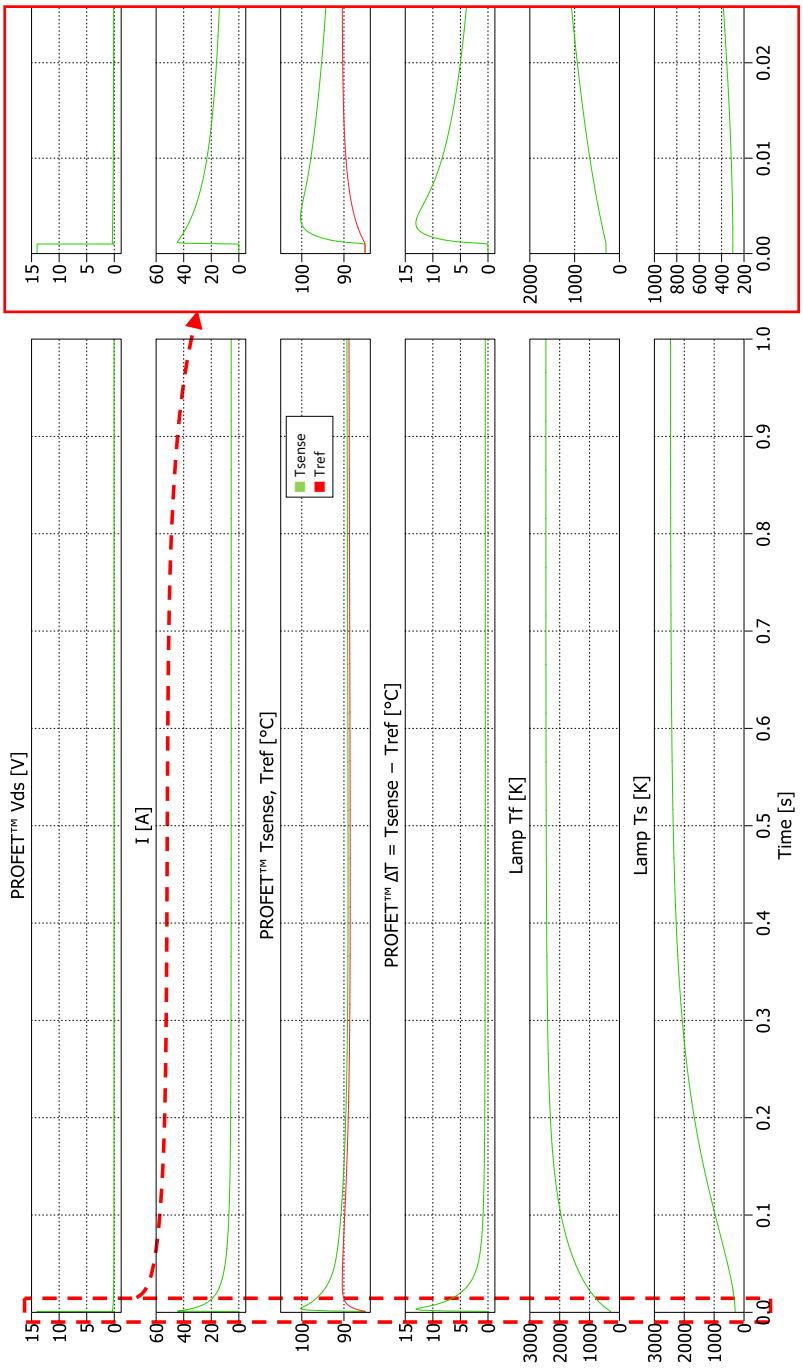

Figure 5.12: Simulation results of a typical load application scenario: the PROFET™ is driving a heaten filament lamp.

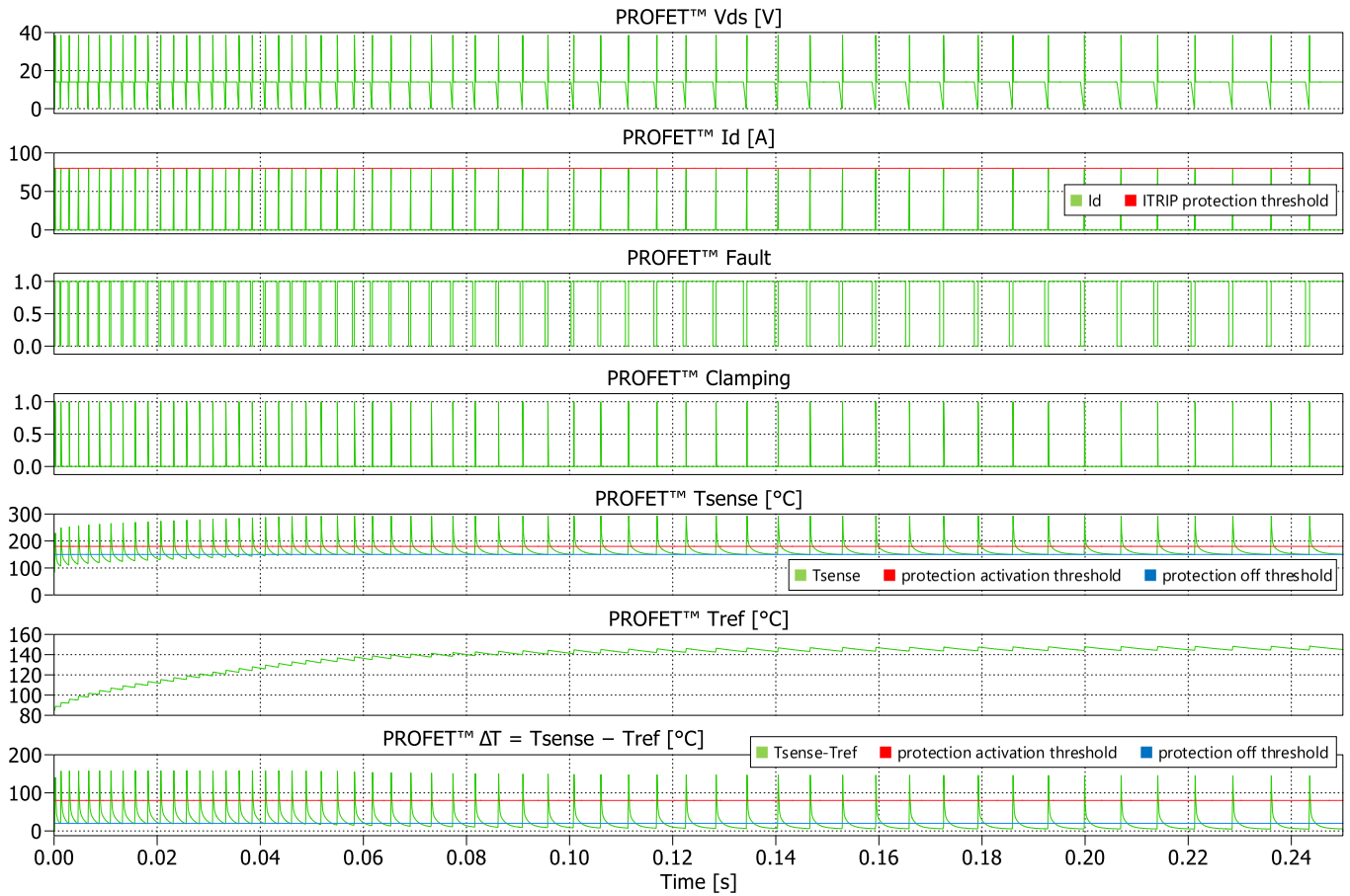

Figure 5.13: Simulation results of a short circuit fault scenario considering the protection thresholds inserted in the model.

protection signal is sent to the FSM, which forces the DMOS to switch off. The overvoltage due to the stray inductances of wires is handled by the PROFET™ via Zener clamping. The self-heating induced by such fault event is higher than in normal operation, and the protections are designed to keep the device within its Safe Operating Area (SOA). The device is then allowed to restart when the protections are internally released, since the faulty condition has disappeared. Due to the persistence of the short-circuit, at each restart the temperature T_{ref}, as well as T_{sense} peak value, keeps increasing until reaching a periodic behavior. This results in a progressive increase of the delay in restart time. In fact, the average temperature reached by the device is closer to the lower threshold, so the OT requires more time to exit from its fault condition.

5.4 Enhanced Model with Current Limitation

The model presented so far for the device represents the common behavior of the majority of the traditional PROFET™ products, which are mainly based on ITRIP (overcurrent) protection. However, newly commercialized products can operate in current limitation mode when in overload conditions. To recreate such a behavior, it is necessary to improve the model of the built-in switch in order to be able to vary the channel resistance of the device to control the current flowing through it. A physical model is required where the source-gate connection is available.

To keep the model lean and able to simulate entire mission profiles in reasonable time, we choose to adopt the Curtice model [167] to describe using a single equation (5.6) both the operating regions of the FET (avoiding discontinuities).

$$I_D = \beta(V_{GS} - V_{T0})^2(1 + \lambda V_{DS})\tanh(\alpha V_{DS}) \tag{5.6}$$

where:

- α: is the V_{DS} slope [1/V],
- β: is the gain [A/V^2],
- λ: is the channel length modulation [1/V],
- V_{T0}: is the channel threshold voltage [V].

The Curtice model implementation in PLECS is shown in Figure 5.14. We put an additional RC stage on the gate to obtain a realistic finite turn-on and turn-off behavior of the FET and we added a bypass switch to avoid reaching negative current flowing in *FET1* if going outside of the model's field of existence.

Figure 5.15 shows the global view of the enhanced PROFET™ model with current limitation. Because when I_D becomes negative a clamping occurs and *Z1* acts as a short circuit, *FET1* is no more effective, and its effect can be temporarily removed bypassing it (*S1*) in order to help the solver and to speed up the simulation, avoiding handling discontinuities in Curtice model due to abrupt variations of V_{DS}.

Current limitation behavior is modelled, as in Figure 5.16, by monitoring the difference between the nominal current limit (*I_lim*) of the product (adjustable in the PROFET™ model mask) and the instantaneous value of I_D. When the latter starts approaching the limit value, the gate voltage (*Vg0*) of the Curtice FET is proportionally reduced till reaching a null value when $I_D \geq I\_lim$. The slope of the limitation action can be controlled by varying the *klim* gain value.

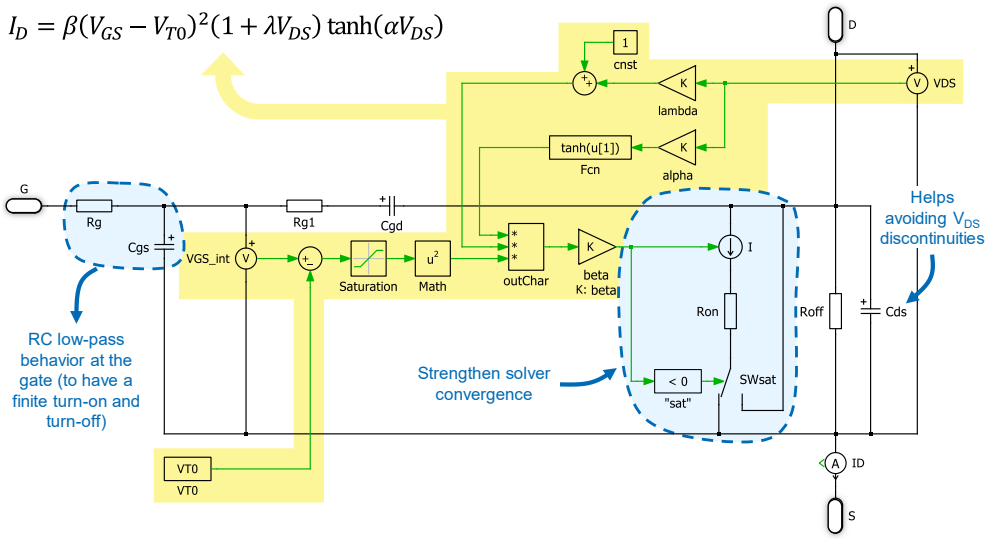

Figure 5.14: Curtice FET model implementation in PLECS.

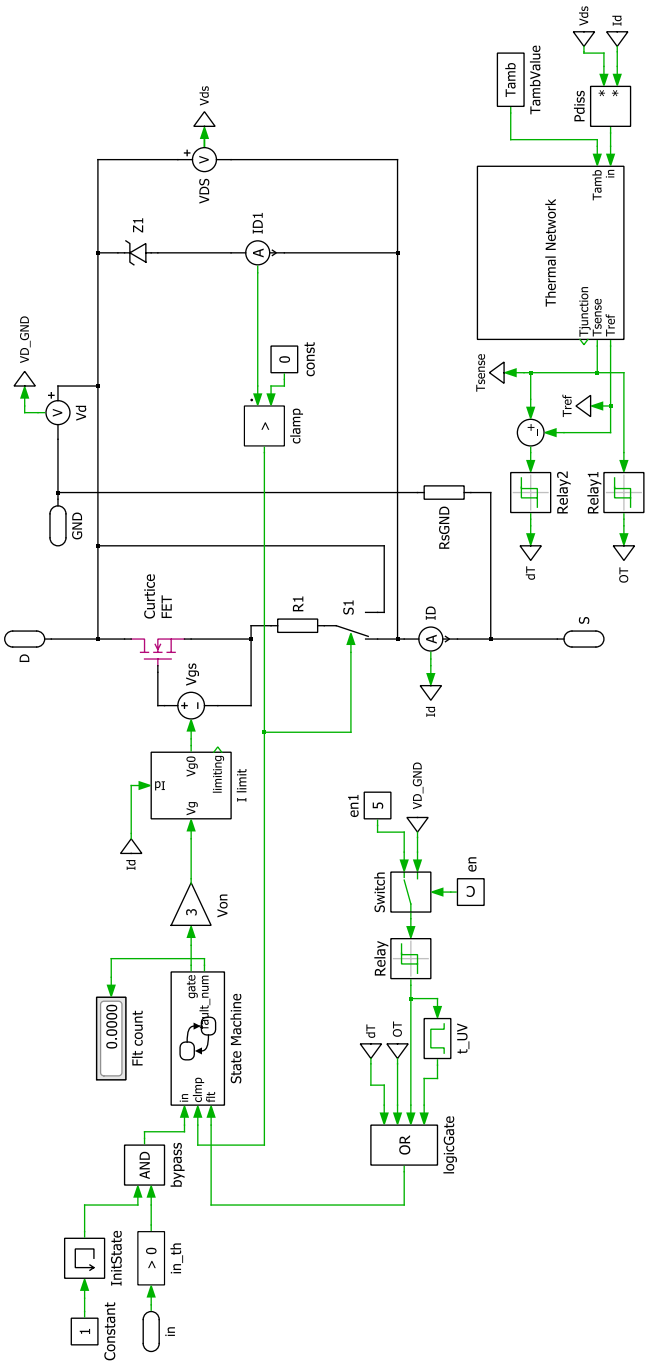

Figure 5.15: Global view of the PROFET™ model with *Curtice FET* model (Figure 5.14) and current limitation control (*I limit*).

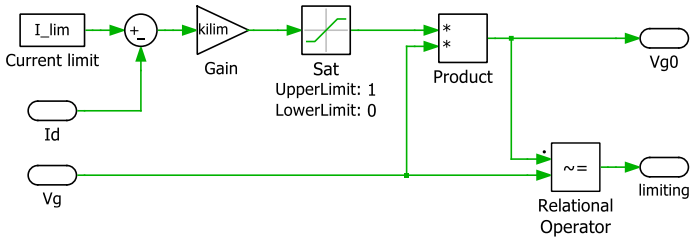

Figure 5.16: Current limitation controller.

5.4.1 Simulation of Power Distribution Networks

The two models presented so far for the PROFET™ devices – namely the one with current protection (*ITRIP*) and the one with current limitation (*ILIM*) – are very useful in understanding the behavior of power distribution networks (PDN), where multiple high-side switches are employed at different levels of the network. In this sub-paragraph we show two simple examples of a 2-layer PDN. They show the advantages of this kind of simulation approach which allows system designers to test many different configurations of a PDN choosing the right PROFET™ products, accounting for possible faulty conditions at different levels of the PDN and their effects on the remaining parts of the network.

The first simulation scenario is presented in Figure 5.17. The PDN is supplied by a 12 V battery (2nd order R-R‖C equivalent model [168]). The whole network is driven by an *ILIM* device (90 A limitation threshold) located at the root level, then each load, namely 2 lamps, a resistive load, and a capacitive load, is controlled by an *ITRIP* device (80 A protection threshold). Also the cables are considered, with typical lengths for automotive applications. Details about the size of each component can be found in Figure 5.17.

Simulation output in Figure 5.18 shows that, in the turn-on phase (all loads are turned on at time t = 3 ms), the current inrush on the lamps, along with the capacitor *Cld3*, causes the *PROFET0* to trigger the current limitation state. When the current limitation threshold is exceeded the control logic makes the embedded DMOS to increase its channel resistance, so the voltage across the *PROFET0* starts increasing and, consequently, the supply voltage on the lower end of the distribution network

decreases. This causes the devices *1* and *4* to trigger an under-voltage fault (namely the voltage supply protection). We see that V_{DS_0} is zero because *PROFET0* is active since the beginning of the simulation, then all the loads are turned-on (so $V_{DS_{1,2,3,4}}$ drop to 0 and $I_{D_{1,2,3,4}}$ increase) and I_{D_0} starts increasing until it reaches the 90 A threshold. At this point, V_{DS_0} rapidly increases in order to cope with the current in-rush. The increase in V_{DS_0} voltage-drop, causes *PROFET1* and *4* to go in voltage supply protection (third group of plots in Figure 5.18), therefore they turn-off and back on again after a short recovery time. In addition, it is interesting to note that, while *PROFET1* and *4* go in under voltage condition, this is not the case for *PROFET2* and *3*. This is due to the inductive behavior of the cables which allows to keep the voltage of the second side of the network at a sufficient level.

Summarizing, this first scenario allows system designers to catch one possible issue arising when using current-limited devices as upper-level switches.

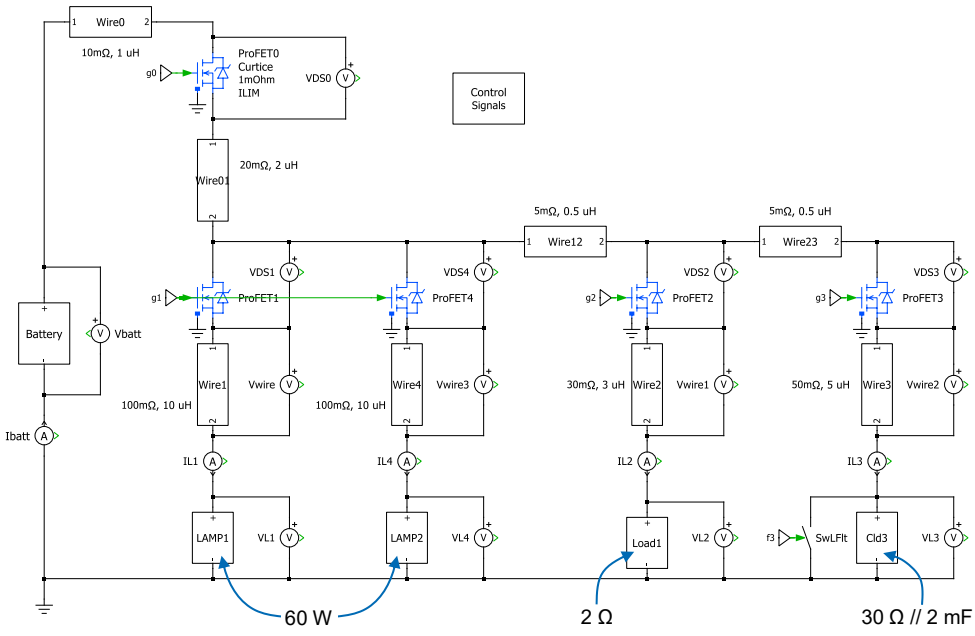

Figure 5.17: Simulation scenario of a 2-layer PDN with an *ILIM* root device and four load driving *ITRIP* devices.

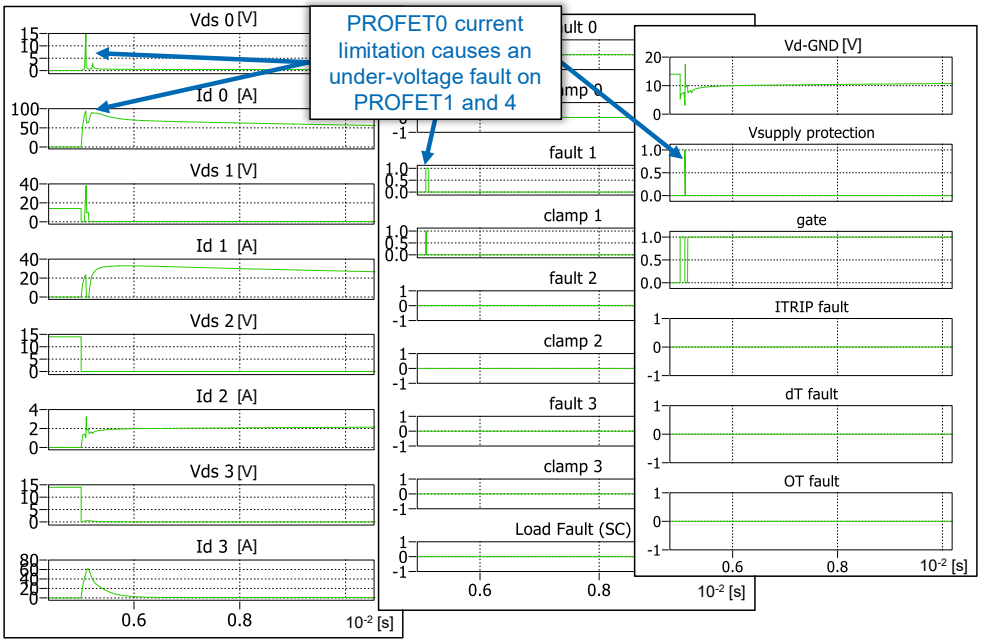

Figure 5.18: Simulation results of the first proposed scenario (Figure 5.17).

The schematic of the second example we propose is in Figure 5.19. A 3.3 mF intermediate-level buffer capacitor (*Cbuffer*) is added as a possible solution to mitigate current limitation effects due to *ILIM* root devices, when coping with loads with high turn-on inrush currents. As shown in Figure 5.20, at time t = 10ms *PROFET0* is turned on and it instantaneously goes in current limitation due to the high current inrush caused by *Cbuffer* charging.

At time t = 10ms, loads are turned-on and, as in the previous scenario, we have a high inrush current peak and *PROFET0* tries to limit it, increasing its V_{DS}. However, in this second case, thanks to the buffer capacitor, the voltage on the bus (namely the supply voltage for *PROFET1* and *4*) is kept at an acceptable level (between 8 and 9 V) resulting in no voltage supply fault condition as confirmed by the mid-plot in Figure 5.20.

We have an additional advantage coming from the introduction of *Cbuffer*: the current of *PROFET0* is much less "noisy" when one of the load-end devices is in *ITRIP* condition, therefore, I_{D_1} and I_{D_4} are less affected by the I_{D_2} or I_{D_3} behavior in case of short circuit faults.

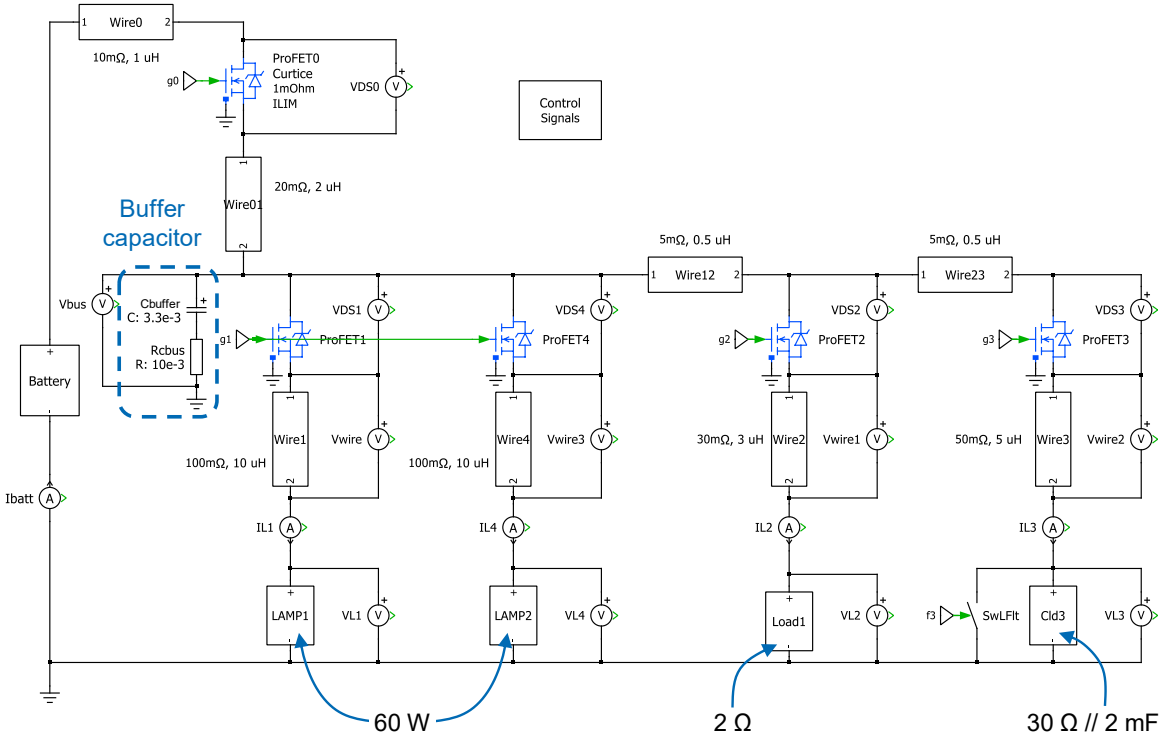

Figure 5.19: Simulation scenario of a 2-layer PDN with additional buffer capacitor.

Concluding, the modeling approach discussed in this chapter demonstrate how the behavioral modelling allows system designers to build a comprehensive system-level model including the main control functionalities and protections of the device under design, allowing to study the interaction between components at different levels of the PDN by means of mission profile simulations, keeping the simulation time within reasonable bounds.

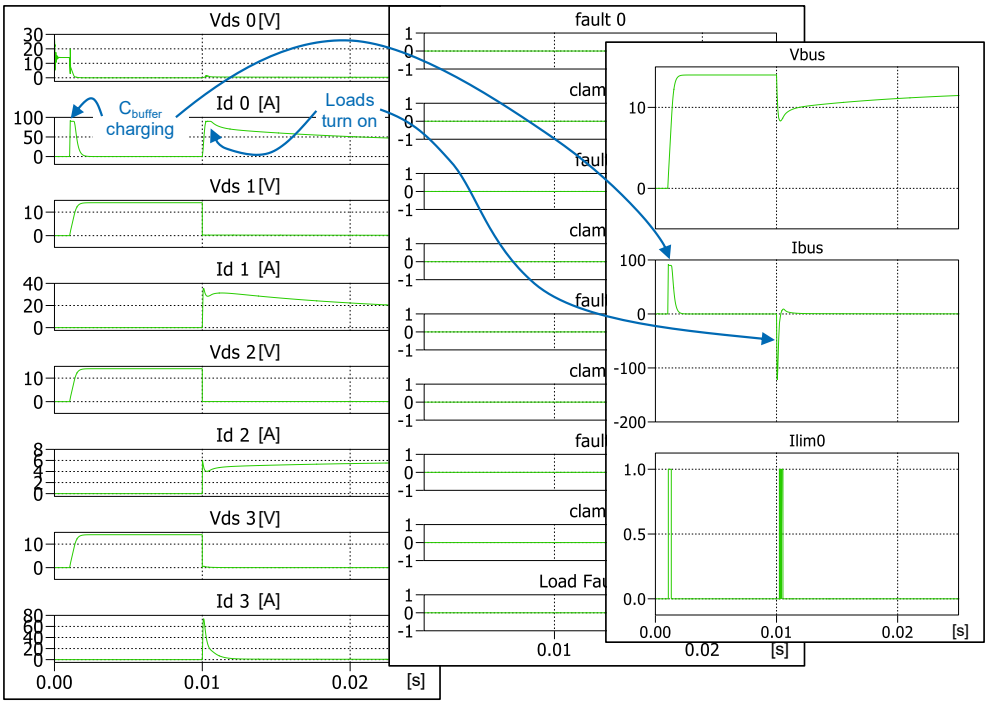

Figure 5.20: Simulation results of the second proposed scenario (Figure 5.19).

Conclusions

In this dissertation the topic of top-level behavioral simulation models for SGs (MGs and NGs) has been explored, presenting three case study (Chapter 2, Chapter 3 and Chapter 4).

The traditional power generation and distribution systems will be supplanted by the SG concept which will give a major shift the way the legacy power grid has been traditionally designed and managed. The wide plethora of actors involved in this process, including intermittent and variable generation from RES, mobile loads, and storage, such as EVs and the need of plug-and-play functionalities, will increase the uncertainty and complexity of the energy management system. This complexity accelerates the need to identify the appropriate computational tools to perform designing and sizing actions in this future SG context.

MBD approach alongside with the adoption of DTs in SCADA systems, opens for the necessity to have simplified behavioral models in order to satisfy real-time and faster than real-time execution constraints.

One of the main contributions of this thesis consists in providing a library of behavioral models, and showing the approach we adopted, to allow smart grid simulations to be carried out on a large time scale (in the order of months to years) maintaining reasonably small the ratio between the simulated time span and the computation time required by completing the simulation. In this context, the main work presented in the thesis is the simulation model of the UPSC (Chapter 2). University campuses are natural playgrounds for the development of district-level MG concepts, thanks to the ideal scale and their dynamic environment due to the presence of many different facilities: scientific, technological, recreational, sports, etc.

Detailed modeling of the key elements of the energy infrastructure and of the MG as a whole is a necessary step: first, as a design and planning tool, in the second stage, as the backbone of the MG control system. The development of a MATLAB-based campus MG model has been presented as well as its use to investigate possible scenarios of PV generation and BESS deployment in combination with EV charging stations. Additionally, a detailed model of the heat-pump-based heating/cooling system of a campus building, coupling the dynamic thermal model with the electric grid model is included; this kind of comprehensive energy grid modeling will likely gain importance in the near future as the concept of integrated energy districts and their modeling become more common.

Solar photovoltaic technology is one of the renewable technologies, which has a potential to shape a clean, reliable, scalable, and affordable electricity system for the future. In addition, it is the most abundant, inexhaustible, and clean. Considering this fact, all over the world governments are encouraging the development and deployment of solar PV technology. Nevertheless, the use of solar PV plants requires particular attention to the monitoring and maintenance processes of the PV modules. For this reason, PV monitoring issues have been analyzed in Chapter 3. A new smart soiling sensor prototype has been proposed coupled with the simulation model of a DC NG. Accounting for the effect of the soiling deposited on the modules, the model allows to plan the optimum scheduling time for PV cleaning interventions, balancing the loss of production due to soil with the cost of a cleaning intervention, thus minimizing the economic impact.

For the reasons discussed in several points of this dissertation, environmental and economic considerations encourage the use of RES to charge the batteries of EVs in industrial environments. This requires having tools to proper design the grid architecture and size the facility power system. If the primary energy source is a PV plant, maximizing self-sufficiency requires the installation of a suitably sized ESS, and increasing the ESS capacity is critical for reducing the energy exchange with the PG. In Chapter 4 a novel approach to define the most suitable grid architecture based on behavioral PLECS modeling has been presented. From simulation outputs, it is possible to find the optimum trade-off between the costs of initial investment, running costs and PG consumption considering both economic and environmental perspectives. In particular, the model considers the number of EVs, initial investment costs, PG consumption costs, CO_2 footprint, and EV working time requirements.

Recently, behavioral modelling is gaining more and more importance in various designing fields. In Chapter 5 the behavioral approach has been applied to the case of automotive PDNs. The work, carried out on behalf of Infineon Technology Austria, is focused on designing the simulation model of a high side switch (namely, PROFET™ family products) for automotive applications. The behavior of the model has been described including all the main control functionalities and protections of the device. Finally, the model of the product has been used to demonstrate how behavioral modelling allows system designers to study the interaction between components at different levels of the PDN by means of mission profile simulations, keeping the simulation time within reasonable bounds.

Appendix A

List of Publications

A1 D. Santoro, N. Rocchi, S. Sapienza, M. Simonazzi, G. Sozzi, P. Cova, G. Chiorboli, R. Menozzi, N. Delmonte, R. Guilly, “Development of a PV modules soiling monitoring system for smart maintenance”, XXXIV Conference on Design of Circuits and Integrated Systems, DCIS 2019, November 20-22, Bilbao (Spain), 2019.

A2 M. Simonazzi, G. Chiorboli, P. Cova, R. Menozzi, D. Santoro, S. Sapienza, C. Sciancalepore, G. Sozzi, N. Delmonte, “Smart soiling sensor for PV modules”, Microelectronics Reliability, 2020, doi: 10.1016/j.microrel.2020.113789.

A3 M. Simonazzi, D. Santoro, M. Bernardoni, N. Delmonte, P. Cova, R. Menozzi, “Behavioral modeling of PROFETTM devices for system-level simulation of mission profiles in automotive environment applications”, Microelectronics Reliability, 2021, doi: 10.1016/j.microrel.2021.114324.

A4 M. Simonazzi, N. Delmonte, P. Cova, G. Ferrari, F. Zanichelli, R. Menozzi, “Modeling of a university campus Micro-Grid for optimal planning of renewable generation and storage deployment”, 2020 IEEE International Smart Cities Conference (ISC2), 2021, doi: 10.1109/ISC253183.2021.9562796.

A5 A.A. Nkembi, M. Simonazzi, D. Santoro, P. Cova, R. Menozzi, N. Delmonte, “Designing power systems to charge electrical vehicle fleets in the industrial environment”, in Proceedings of SIE 2022, Lecture Notes in Electrical Engineering, SpringerLink, 2022.

Bibliography

[1] A. R. Javed *et al.*, "Future smart cities: requirements, emerging technologies, applications, challenges, and future aspects," *Cities*, vol. 129, p. 103794, Oct. 2022, doi: 10.1016/j.cities.2022.103794.

[2] M. Angelidou, "Smart cities: A conjuncture of four forces," *Cities*, vol. 47, pp. 95–106, Sep. 2015, doi: 10.1016/j.cities.2015.05.004.

[3] ITU-T Focus Group on Smart Sustainable Cities, "Smart sustainable cities: An analysis of definitions," *Technical Report*, Oct. 2014.

[4] M. Masera, E. F. Bompard, F. Profumo, and N. Hadjsaid, "Smart (Electricity) Grids for Smart Cities: Assessing Roles and Societal Impacts," *Proceedings of the IEEE*, vol. 106, no. 4. Institute of Electrical and Electronics Engineers Inc., pp. 613–625, Apr. 01, 2018. doi: 10.1109/JPROC.2018.2812212.

[5] "26 marzo: presentazione di SMART CITY 4.0 Sustainable Lab," *Università di Parma*, 2018. https://www.unipr.it/notizie/26-marzo-presentazione-di-smart-city-40-sustainable-lab (accessed Sep. 23, 2022).

[6] Roberto Menozzi and Dario Costi, "A University-Driven Regional-Scale Initiative for Transitioning To Smart & Wise Cities and Towns in the Northern Italian Emilia Region," *IEEE Smart Cities eNewsletter*. Sep. 2021. Accessed: Sep. 23, 2022. [Online]. Available: https://smartcities.ieee.org/newsletter/september-2021/a-university-driven-regional-scale-initiative-for-transitioning-to-smart-wise-cities-and-towns-in-the-northern-italian-emilia-region

[7] N. Hatziargyriou, *Microgrid: architecture and control*. Wiley-IEEE Press, 2014.

[8] C. Greer *et al.*, “NIST Framework and Roadmap for Smart Grid Interoperability Standards, Release 3.0,” Gaithersburg, MD, Oct. 2014. doi: 10.6028/NIST.SP.1108r3.

[9] Fred Sissine, “Energy Independence and Security Act of 2007: A Summary of Major Provisions,” Dec. 2007.

[10] O. Siddiqui, “The Green Grid - Energy Savings and Carbon Emissions Reductions Enabled by a Smart Grid,” Palo Alto, CA, May 2008.

[11] P. Palensky and F. Kupzog, “Smart Grids,” *Annu Rev Environ Resour*, vol. 38, no. 1, pp. 201–226, Oct. 2013, doi: 10.1146/annurev-environ-031312-102947.

[12] Y. Bamberger *et al.*, “Vision and Strategy for Europe’s Electricity Networks of the Future,” *European Technology PlatformSmartGrids*, Sep. 2006.

[13] C. Marnay *et al.*, “Microgrid Evolution Roadmap,” in *2015 International Symposium on Smart Electric Distribution Systems and Technologies (EDST)*, Sep. 2015, pp. 139–144. doi: 10.1109/SEDST.2015.7315197.

[14] S. Parhizi, H. Lotfi, A. Khodaei, and S. Bahramirad, “State of the Art in Research on Microgrids: A Review,” *IEEE Access*, vol. 3, pp. 890–925, 2015, doi: 10.1109/ACCESS.2015.2443119.

[15] S. Ansari, A. Chandel, and M. Tariq, “A Comprehensive Review on Power Converters Control and Control Strategies of AC/DC Microgrid,” *IEEE Access*, vol. 9, pp. 17998–18015, 2021, doi: 10.1109/ACCESS.2020.3020035.

[16] K. Cabana-Jiménez, J. E. Candelo-Becerra, and V. S. Santos, “Comprehensive Analysis of Microgrids Configurations and Topologies,” *Sustainability (Switzerland)*, vol. 14, no. 3. MDPI, Feb. 01, 2022. doi: 10.3390/su14031056.

[17] M. Y. Nguyen and Y. T. Yoon, “A Comparison of Microgrid Topologies Considering Both Market Operations and Reliability,” *Electric Power Components and Systems*, vol. 42, no. 6, pp. 585–594, Apr. 2014, doi: 10.1080/15325008.2014.880963.

[18] J. J. Justo, F. Mwasilu, J. Lee, and J. W. Jung, “AC-microgrids versus DC-microgrids with distributed energy resources: A review,” *Renewable and Sustainable Energy Reviews*, vol. 24. pp. 387–405, 2013. doi: 10.1016/j.rser.2013.03.067.

[19] D. Boroyevich, I. Cvetković, D. Dong, R. Burgos, F. Wang, and F. Lee, “Future electronic power distribution systems - A contemplative view,” in

Proceedings of the International Conference on Optimisation of Electrical and Electronic Equipment, OPTIM, 2010, pp. 1369–1380. doi: 10.1109/OPTIM.2010.5510477.

[20] A. Karabiber, C. Keles, A. Kaygusuz, and B. B. Alagoz, "An approach for the integration of renewable distributed generation in hybrid DC/AC microgrids," *Renew Energy*, vol. 52, pp. 251–259, Apr. 2013, doi: 10.1016/j.renene.2012.10.041.

[21] D. Salomonsson and A. Sannino, "Low-voltage DC distribution system for commercial power systems with sensitive electronic loads," *IEEE Transactions on Power Delivery*, vol. 22, no. 3, pp. 1620–1627, 2007, doi: 10.1109/TPWRD.2006.883024.

[22] B. Nordman, K. Christensen, and A. Meier, "Think Globally, Distribute Power Locally: The Promise of Nanogrids," *Computer (Long Beach Calif)*, vol. 45, no. 9, pp. 89–91, Sep. 2012, doi: 10.1109/MC.2012.323.

[23] A. Werth, N. Kitamura, and K. Tanaka, "Conceptual Study for Open Energy Systems: Distributed Energy Network Using Interconnected DC Nanogrids," *IEEE Trans Smart Grid*, vol. 6, no. 4, pp. 1621–1630, Jul. 2015, doi: 10.1109/TSG.2015.2408603.

[24] C. L. Sulzberger, "Triumph of ac," *IEEE Power and Energy Magazine*, vol. 99, no. 3, pp. 64–67, 2003, doi: 10.1109/MPAE.2003.1197918.

[25] C. L. Sulzberger, "Triumph of AC, Part 2," *IEEE Power and Energy Magazine*, vol. 99, no. 4, pp. 70–73, 2003, doi: 10.1109/MPAE.2003.1213534.

[26] R. Asad and A. Kazemi, "A quantitative analysis of effects of transition from AC to DC system, on storage and distribution systems," in *Asia-Pacific Power and Energy Engineering Conference, APPEEC*, 2012. doi: 10.1109/APPEEC.2012.6307519.

[27] T. Dragičević, J. C. Vasquez, J. M. Guerrero, and D. Škrlec, "Advanced LVDC electrical power architectures and microgrids: A step toward a new generation of power distribution networks," *IEEE Electrification Magazine*, vol. 2, no. 1, pp. 54–65, Mar. 2014, doi: 10.1109/MELE.2013.2297033.

[28] A. Stippich *et al.*, "From Ac to Dc: Benefits in Household Appliances," in *International ETG Congress 2017*, 2017, pp. 1–6.

[29] R. Kumar and R. K. Behera, "A Low Cost Distributed Solar DC Nanogrid: Design and Deployment with Remote Monitoring Unit," in *2018 20th*

National Power Systems Conference (NPSC), Dec. 2018, pp. 1–6. doi: 10.1109/NPSC.2018.8771825.

[30] E. Rodriguez-Diaz, J. C. Vasquez, and J. M. Guerrero, "Intelligent DC Homes in Future Sustainable Energy Systems: When efficiency and intelligence work together," *IEEE Consumer Electronics Magazine*, vol. 5, no. 1, pp. 74–80, Jan. 2016, doi: 10.1109/MCE.2015.2484699.

[31] M. Starke, Fangxing Li, L. M. Tolbert, and B. Ozpineci, "AC vs. DC distribution: Maximum transfer capability," in *2008 IEEE Power and Energy Society General Meeting - Conversion and Delivery of Electrical Energy in the 21st Century*, Jul. 2008, pp. 1–6. doi: 10.1109/PES.2008.4596730.

[32] S. Moussa, M. J.-B. Ghorbal, and I. Slama-Belkhodja, "Bus voltage level choice for standalone residential DC nanogrid," *Sustain Cities Soc*, vol. 46, p. 101431, Apr. 2019, doi: 10.1016/j.scs.2019.101431.

[33] A. Khan, M. B. Shadmand, S. Bayhan, and H. Abu-Rub, "A Power Ripple Compensator for DC Nanogrids via a Solid-State Converter," *IEEE Open Journal of the Industrial Electronics Society*, vol. 1, pp. 311–325, 2020, doi: 10.1109/OJIES.2020.3035073.

[34] F. A. Rahman, R. James, S. Jose, S. Ahmed, M. S. A. Mohammed, and K. B. Kunju, "Solar DC Homes: Energy for All," in *TENCON 2019 - 2019 IEEE Region 10 Conference (TENCON)*, Oct. 2019, pp. 2428–2432. doi: 10.1109/TENCON.2019.8929303.

[35] S. C. Joseph, S. Ashok, and P. R. Dhanesh, "An effective method of power management in DC nanogrid for building application," in *2017 IEEE International Conference on Signal Processing, Informatics, Communication and Energy Systems (SPICES)*, Aug. 2017, pp. 1–5. doi: 10.1109/SPICES.2017.8091303.

[36] R. Weiss, L. Ott, and U. Boeke, "Energy efficient low-voltage DC-grids for commercial buildings," in *2015 IEEE First International Conference on DC Microgrids (ICDCM)*, Jun. 2015, pp. 154–158. doi: 10.1109/ICDCM.2015.7152030.

[37] X. Wu, Z. Wang, T. Ding, and Z. Li, "Hybrid AC/DC Microgrid Planning with Optimal Placement of DC Feeders," *Energies (Basel)*, vol. 12, no. 9, p. 1751, May 2019, doi: 10.3390/en12091751.

[38] P. C. D. Goud and R. Gupta, “Solar PV based nanogrid integrated with battery energy storage to supply hybrid residential loads using single-stage hybrid converter,” *IET Energy Systems Integration*, vol. 2, no. 2, pp. 161–169, Jun. 2020, doi: 10.1049/iet-esi.2019.0030.

[39] M. C. Bozchalui and R. Sharma, “Optimal operation of commercial building microgrids using multi-objective optimization to achieve emissions and efficiency targets,” in *2012 IEEE Power and Energy Society General Meeting*, Jul. 2012, pp. 1–8. doi: 10.1109/PESGM.2012.6345600.

[40] H. Lotfi and A. Khodaei, “Hybrid AC/DC microgrid planning,” *Energy*, vol. 118, pp. 37–46, Jan. 2017, doi: 10.1016/j.energy.2016.12.015.

[41] H. R. E. H. Bouchekara *et al.*, “Optimal sizing of hybrid photovoltaic/diesel/battery nanogrid using a parallel multiobjective PSO-based approach: Application to desert camping in Hafr Al-Batin city in Saudi Arabia,” *Energy Reports*, vol. 7, pp. 4360–4375, Nov. 2021, doi: 10.1016/j.egyr.2021.07.015.

[42] A. T. Dahiru, C. W. Tan, A. L. Bukar, and K. Yiew Lau, “Energy cost reduction in residential nanogrid under constraints of renewable energy, customer demand fitness and binary battery operations,” *J Energy Storage*, vol. 39, p. 102520, Jul. 2021, doi: 10.1016/j.est.2021.102520.

[43] M. Shahidehpour, Z. Li, W. Gong, S. Bahramirad, and M. Lopata, “A Hybrid ac/dc Nanogrid: The Keating Hall Installation at the Illinois Institute of Technology.,” *IEEE Electrification Magazine*, vol. 5, no. 2, pp. 36–46, Jun. 2017, doi: 10.1109/MELE.2017.2685858.

[44] J. Kumar, A. Agarwal, and V. Agarwal, “A review on overall control of DC microgrids,” *J Energy Storage*, vol. 21, pp. 113–138, Feb. 2019, doi: 10.1016/j.est.2018.11.013.

[45] Chaoyong Hou, Xuehao Hu, and Dong Hui, “Hierarchical control techniques applied in micro-grid,” in *2010 International Conference on Power System Technology*, Oct. 2010, pp. 1–5. doi: 10.1109/POWERCON.2010.5666418.

[46] J. M. Guerrero, J. C. Vasquez, J. Matas, L. G. de Vicuna, and M. Castilla, “Hierarchical Control of Droop-Controlled AC and DC Microgrids—A General Approach Toward Standardization,” *IEEE Transactions on Industrial Electronics*, vol. 58, no. 1, pp. 158–172, Jan. 2011, doi: 10.1109/TIE.2010.2066534.

[47] A. Bidram, “Distributed Cooperative Control of ac microgrid,” 2014.

[48] Z. Liu, J. Liu, D. Boroyevich, and R. Burgos, "Stability criterion of droop-controlled parallel inverters based on terminal-characteristics of individual inverters," in *2016 IEEE 8th International Power Electronics and Motion Control Conference (IPEMC-ECCE Asia)*, May 2016, pp. 2958–2963. doi: 10.1109/IPEMC.2016.7512767.

[49] A. Saleh-Ahmadi, M. Moattari, A. Gahedi, and E. Pouresmaeil, "Droop Method Development for Microgrids Control Considering Higher Order Sliding Mode Control Approach and Feeder Impedance Variation," *Applied Sciences*, vol. 11, no. 3, p. 967, Jan. 2021, doi: 10.3390/app11030967.

[50] U. B. Tayab, M. A. bin Roslan, L. J. Hwai, and M. Kashif, "A review of droop control techniques for microgrid," *Renewable and Sustainable Energy Reviews*, vol. 76. Elsevier Ltd, pp. 717–727, 2017. doi: 10.1016/j.rser.2017.03.028.

[51] R. A. F. Ferreira, H. A. C. Braga, A. A. Ferreira, and P. G. Barbosa, "Analysis of voltage droop control method for dc microgrids with Simulink: Modelling and simulation," in *2012 10th IEEE/IAS International Conference on Industry Applications, INDUSCON 2012*, 2012. doi: 10.1109/INDUSCON.2012.6452563.

[52] K. R. Bharath, A. D. Student, and P. Kanakasabapathy, "A simulation study on modified droop control for improved voltage regulation in DC microgrid," in *2017 International Conference on Intelligent Computing, Instrumentation and Control Technologies, ICICICT 2017*, Apr. 2018, vol. 2018-January, pp. 314–319. doi: 10.1109/ICICICT1.2017.8342581.

[53] T. v. Vu, D. Perkins, F. Diaz, D. Gonsoulin, C. S. Edrington, and T. El-Mezyani, "Robust adaptive droop control for DC microgrids," *Electric Power Systems Research*, vol. 146, pp. 95–106, May 2017, doi: 10.1016/j.epsr.2017.01.021.

[54] P. Singh, P. Paliwal, and A. Arya, "A Review on Challenges and Techniques for Secondary Control of Microgrid," *IOP Conf Ser Mater Sci Eng*, vol. 561, no. 1, p. 012075, Oct. 2019, doi: 10.1088/1757-899X/561/1/012075.

[55] A. Kaur, J. Kaushal, and P. Basak, "A review on microgrid central controller," *Renewable and Sustainable Energy Reviews*, vol. 55, pp. 338–345, Mar. 2016, doi: 10.1016/j.rser.2015.10.141.

[56] S. K. Mazumder, M. Tahir, and K. Acharya, "Master–Slave Current-Sharing Control of a Parallel DC–DC Converter System Over an RF Communication Interface," *IEEE Transactions on Industrial Electronics*, vol. 55, no. 1, pp. 59–66, Jan. 2008, doi: 10.1109/TIE.2007.896138.

[57] S. Guiying, L. Da, L. Yuesheng, and T. Yanbin, "Master-slave with phase-shift control strategy for input-series and output-parallel full-bridge DC-DC converter system," in *2016 IEEE 11th Conference on Industrial Electronics and Applications (ICIEA)*, Jun. 2016, pp. 2546–2551. doi: 10.1109/ICIEA.2016.7604022.

[58] W. Zhao, X. Zhang, Y. Li, and N. Qian, "Improved master-slave control for Smooth Transition Between Grid-connected and Islanded Operation of DC Microgrid Based on I -ΔV Droop," in *2020 IEEE 9th International Power Electronics and Motion Control Conference (IPEMC2020-ECCE Asia)*, Nov. 2020, pp. 1194–1198. doi: 10.1109/IPEMC-ECCEAsia48364.2020.9367870.

[59] V. Nasirian, S. Moayedi, A. Davoudi, and F. L. Lewis, "Distributed Cooperative Control of DC Microgrids," *IEEE Trans Power Electron*, vol. 30, no. 4, pp. 2288–2303, Apr. 2015, doi: 10.1109/TPEL.2014.2324579.

[60] Q. Shafiee, J. M. Guerrero, and J. C. Vasquez, "Distributed Secondary Control for Islanded Microgrids—A Novel Approach," *IEEE Trans Power Electron*, vol. 29, no. 2, pp. 1018–1031, Feb. 2014, doi: 10.1109/TPEL.2013.2259506.

[61] E. Espina, J. Llanos, C. Burgos-Mellado, R. Cardenas-Dobson, M. Martinez-Gomez, and D. Saez, "Distributed Control Strategies for Microgrids: An Overview," *IEEE Access*, vol. 8, pp. 193412–193448, 2020, doi: 10.1109/ACCESS.2020.3032378.

[62] M. Yazdanian and A. Mehrizi-Sani, "Distributed control techniques in microgrids," *IEEE Trans Smart Grid*, vol. 5, no. 6, pp. 2901–2909, Nov. 2014, doi: 10.1109/TSG.2014.2337838.

[63] F. Mumtaz and I. S. Bayram, "Planning, Operation, and Protection of Microgrids: An Overview," *Energy Procedia*, vol. 107, pp. 94–100, Feb. 2017, doi: 10.1016/j.egypro.2016.12.137.

[64] P. Panciatici *et al.*, "Advanced optimization methods for power systems," in *2014 Power Systems Computation Conference*, Aug. 2014, pp. 1–18. doi: 10.1109/PSCC.2014.7038504.

[65] K. Mahmud, A. K. Sahoo, E. Fernandez, P. Sanjeevikumar, and J. B. Holm-Nielsen, "Computational Tools for Modeling and Analysis of Power Generation and Transmission Systems of the Smart Grid," *IEEE Syst J*, vol. 14, no. 3, pp. 3641–3652, Sep. 2020, doi: 10.1109/JSYST.2020.2964436.

[66] H.-K. Ringkjøb, P. M. Haugan, and I. M. Solbrekke, "A review of modelling tools for energy and electricity systems with large shares of variable renewables," *Renewable and Sustainable Energy Reviews*, vol. 96, pp. 440–459, Nov. 2018, doi: 10.1016/j.rser.2018.08.002.

[67] S. Sinha and S. S. Chandel, "Review of software tools for hybrid renewable energy systems," *Renewable and Sustainable Energy Reviews*, vol. 32, pp. 192–205, Apr. 2014, doi: 10.1016/j.rser.2014.01.035.

[68] C. Dufour, Z. Soghomonian, and W. Li, "Hardware-in-the-Loop Testing of Modern On-Board Power Systems Using Digital Twins," in *2018 International Symposium on Power Electronics, Electrical Drives, Automation and Motion (SPEEDAM)*, Jun. 2018, pp. 118–123. doi: 10.1109/SPEEDAM.2018.8445302.

[69] C. Rehtanz and X. Guillaud, "Real-time and co-simulations for the development of power system monitoring, control and protection," in *2016 Power Systems Computation Conference (PSCC)*, Jun. 2016, pp. 1–20. doi: 10.1109/PSCC.2016.7541030.

[70] "What Is an S-Function?," *MathWorks website*. https://www.mathworks.com/help/simulink/sfg/what-is-an-s-function.html (accessed Jun. 14, 2022).

[71] A. Rasheed, O. San, and T. Kvamsdal, "Digital Twin: Values, Challenges and Enablers From a Modeling Perspective," *IEEE Access*, vol. 8, pp. 21980–22012, 2020, doi: 10.1109/ACCESS.2020.2970143.

[72] P. T. Baboli, D. Babazadeh, and D. R. Kumara Bowatte, "Measurement-based Modeling of Smart Grid Dynamics: A Digital Twin Approach," in *2020 10th Smart Grid Conference (SGC)*, Dec. 2020, pp. 1–6. doi: 10.1109/SGC52076.2020.9335750.

[73] Y. Zhong, W. Zhang, X. Ha, Q. Chen, J. Huang, and K. Yan, "Innovative Digital Twin Platform Construction for Smart Grid System," in *2021 IEEE 23rd Int Conf on High Performance Computing & Communications; 7th Int Conf on Data Science & Systems; 19th Int Conf on Smart City; 7th Int Conf on Dependability in Sensor, Cloud & Big Data Systems & Application (HPCC/DSS/SmartCity/DependSys)*, Dec. 2021, pp. 1833–1838. doi: 10.1109/HPCC-DSS-SmartCity-DependSys53884.2021.00271.

[74] C. Brosinsky, D. Westermann, and R. Krebs, "Recent and prospective developments in power system control centers: Adapting the digital twin technology for application in power system control centers," in *2018 IEEE International Energy Conference (ENERGYCON)*, Jun. 2018, pp. 1–6. doi: 10.1109/ENERGYCON.2018.8398846.

[75] M. S. Thomas and J. D. McDonald, *Power System SCADA and Smart Grids*. CRC Press, 2017. doi: 10.1201/b18338.

[76] S. Subedi *et al.*, "Review of Methods to Accelerate Electromagnetic Transient Simulation of Power Systems," *IEEE Access*, vol. 9, pp. 89714–89731, 2021, doi: 10.1109/ACCESS.2021.3090320.

[77] Larissa Paredes Muse, Sudhir Routray, and Irina Oleinikova, "Smart Grids for Smart Cities," *IEEE Smart Grid Bulletin*. Feb. 01, 2022.

[78] S. Bracco, M. Brignone, F. Delfino, and R. Procopio, "An Energy Management System for the Savona Campus Smart Polygeneration Microgrid," *IEEE Syst J*, vol. 11, no. 3, pp. 1799–1809, Sep. 2015, doi: 10.1109/JSYST.2015.2419273.

[79] S. Bracco, F. Delfino, F. Foiadelli, and M. Longo, "On the integration of solar PV and storage batteries within a microgrid," in *2019 IEEE International Conference on Environment and Electrical Engineering and 2019 IEEE Industrial and Commercial Power Systems Europe (EEEIC / I&CPS Europe)*, Jun. 2019, pp. 1–6. doi: 10.1109/EEEIC.2019.8783861.

[80] R. Quadros, J. L. Jucá, J. G. I. Cypriano, R. P. B. da Silva, L. C. P. da Silva, and R. G. Bento, "Implementation of Microgrid on the University Campus of UNICAMP- Brazil: Case Study," *Journal of Electronics and Advanced Electrical Engineering*, vol. 1, no. 2, pp. 21–25, May 2021, doi: 10.47890/JEAEE/2020/RodolfoQuadros/11120009.

[81] O. Lavrova, H. Barsun, R. Burnett, and A. Mammoli, "Renewable energy and smart grid principles integration into campus-wide energy strategy at the University of New Mexico," *International Journal of Technology, Policy and Management*, vol. 12, no. 2/3, p. 212, 2012, doi: 10.1504/IJTPM.2012.046927.

[82] L. A. Santos *et al.*, "Towards a smart grid to the university campus of the federal university of Ceará," in *2015 IEEE 13th Brazilian Power Electronics Conference and 1st Southern Power Electronics Conference (COBEP/SPEC)*, Nov. 2015, pp. 1–6. doi: 10.1109/COBEP.2015.7420271.

[83] M. Chiandone, M. D. Feste, D. Bosich, and G. Sulligoi, "Real-time monitoring and control system for Trieste University Campus electrical distribution grid," in *2019 IEEE Milan PowerTech*, Jun. 2019, pp. 1–5. doi: 10.1109/PTC.2019.8810653.

[84] S. Tellez *et al.*, "National Laboratory of Smart Grids (LAB+i) at the National University of Colombia-Bogotà Campus," in *2014 IEEE PES Transmission & Distribution Conference and Exposition - Latin America (PES T&D-LA)*, Sep. 2014, pp. 1–6. doi: 10.1109/TDC-LA.2014.6955185.

[85] I. M. Jomoah, A. U. M. Al-Abdulaziz, and R. S. Kumar, "Energy management in the buildings of a university campus in Saudi Arabia. A case study," in *4th International Conference on Power Engineering, Energy and Electrical Drives*, May 2013, pp. 659–663. doi: 10.1109/PowerEng.2013.6635688.

[86] F.-V. Jose, G.-M. Norma, R.-F. Ivan, R.-D. Sebastian, G.-O. Arnaldo, and A.-C. Cesar, "Digital Twin of the Medium Voltage Grid of University City at UNAM," in *2021 IEEE PES Innovative Smart Grid Technologies Europe (ISGT Europe)*, Oct. 2021, pp. 1–6. doi: 10.1109/ISGTEurope52324.2021.9640160.

[87] A. Gambarotta, M. Morini, M. Rossi, and M. Stonfer, "A Library for the Simulation of Smart Energy Systems: The Case of the Campus of the University of Parma," *Energy Procedia*, vol. 105, pp. 1776–1781, May 2017, doi: 10.1016/j.egypro.2017.03.514.

[88] A. de Lorenzi, A. Gambarotta, M. Morini, M. Rossi, and C. Saletti, "Setup and testing of smart controllers for small-scale district heating networks: An integrated framework," *Energy*, vol. 205, p. 118054, Aug. 2020, doi: 10.1016/j.energy.2020.118054.

[89] M. Simonazzi, N. Delmonte, P. Cova, G. Ferrari, F. Zanichelli, and R. Menozzi, "Modeling of a university campus Micro-Grid for optimal planning of renewable generation and storage deployment," in *2021 IEEE International Smart Cities Conference (ISC2)*, Sep. 2021, pp. 1–7. doi: 10.1109/ISC253183.2021.9562796.

[90] D. E. Olivares *et al.*, "Trends in Microgrid Control," *IEEE Trans Smart Grid*, vol. 5, no. 4, pp. 1905–1919, Jul. 2014, doi: 10.1109/TSG.2013.2295514.

[91] J. A. P. Lopes, C. L. Moreira, and A. G. Madureira, "Defining Control Strategies for MicroGrids Islanded Operation," *IEEE Transactions on Power Systems*, vol. 21, no. 2, pp. 916–924, May 2006, doi: 10.1109/TPWRS.2006.873018.

[92] H. Sharma and G. Kaur, "Optimization and simulation of smart grid distributed generation: A case study of university campus," in *2016 IEEE Smart Energy Grid Engineering (SEGE)*, Aug. 2016, pp. 153–157. doi: 10.1109/SEGE.2016.7589517.

[93] R. Morales Gonzalez, T. A. J. van Goch, M. F. Aslam, A. Blanch, and P. F. Ribeiro, "Microgrid design considerations for a smart-energy university campus," in *IEEE PES Innovative Smart Grid Technologies, Europe*, Oct. 2014, pp. 1–6. doi: 10.1109/ISGTEurope.2014.7028743.

[94] T. Nasir *et al.*, "Optimal Scheduling of Campus Microgrid Considering the Electric Vehicle Integration in Smart Grid," *Sensors*, vol. 21, no. 21, p. 7133, Oct. 2021, doi: 10.3390/s21217133.

[95] S. M. Putri and D. Maizana, "Optimal Smart Grid Management System in Campus Building," *JURNAL NASIONAL TEKNIK ELEKTRO*, vol. 9, no. 3, Nov. 2020, doi: 10.25077/jnte.v9n3.757.2020.

[96] "Introducing the Phasor Simulation Method." https://it.mathworks.com/help/physmod/sps/powersys/ug/introducing-the-phasor-simulation-method.html (accessed Aug. 01, 2022).

[97] K. H. Bachanek, B. Tundys, T. Wiśniewski, E. Puzio, and A. Marouškova, "Intelligent Street Lighting in a Smart City Concepts—A Direction to Energy Saving in Cities: An Overview and Case Study," *Energies (Basel)*, vol. 14, no. 11, p. 3018, May 2021, doi: 10.3390/en14113018.

[98] J. Parmar, "Typical Calculation of Road Lighting." https://electrical-notes.wordpress.com/2014/05/04/calculate-no-of-street-light-poles/ (accessed Jan. 18, 2022).

[99] S. Lyden and M. E. Haque, "Maximum Power Point Tracking techniques for photovoltaic systems: A comprehensive review and comparative analysis," *Renewable and Sustainable Energy Reviews*, vol. 52, pp. 1504–1518, Dec. 2015, doi: 10.1016/j.rser.2015.07.172.

[100] Hyeonah Park and Hyosung Kim, "PV cell modeling on single-diode equivalent circuit," in *IECON 2013 - 39th Annual Conference of the IEEE Industrial Electronics Society*, Nov. 2013, pp. 1845–1849. doi: 10.1109/IECON.2013.6699412.

[101] R. Chenni, M. Makhlouf, T. Kerbache, and A. Bouzid, "A detailed modeling method for photovoltaic cells," *Energy*, vol. 32, no. 9, pp. 1724–1730, Sep. 2007, doi: 10.1016/j.energy.2006.12.006.

[102] C. Schwingshackl *et al.*, "Wind Effect on PV Module Temperature: Analysis of Different Techniques for an Accurate Estimation," *Energy Procedia*, vol. 40, pp. 77–86, 2013, doi: 10.1016/j.egypro.2013.08.010.

[103] N. Taylor, "Guidelines for PV power measurement in industry," 2010.

[104] N. M. A. Alrahim Shannan, N. Z. Yahaya, and B. Singh, "Single-diode model and two-diode model of PV modules: A comparison," in *2013 IEEE International Conference on Control System, Computing and Engineering*, Nov. 2013, pp. 210–214. doi: 10.1109/ICCSCE.2013.6719960.

[105] A. Virtuani, D. Pavanello, and G. Friesen, "Overview of Temperature Coefficients of Different Thin Film Photovoltaic Technologies," in *25th European Photovoltaic Solar Energy Conference and Exhibition / 5th World Conference on Photovoltaic Energy Conversion, 6-10 September 2010, Valencia, Spain*, 2010.

[106] M. Mattei, G. Notton, C. Cristofari, M. Muselli, and P. Poggi, "Calculation of the polycrystalline PV module temperature using a simple method of energy balance," *Renew Energy*, vol. 31, no. 4, pp. 553–567, Apr. 2006, doi: 10.1016/j.renene.2005.03.010.

[107] M. Koehl, M. Heck, S. Wiesmeier, and J. Wirth, "Modeling of the nominal operating cell temperature based on outdoor weathering," *Solar Energy*

Materials and Solar Cells, vol. 95, no. 7, pp. 1638–1646, Jul. 2011, doi: 10.1016/j.solmat.2011.01.020.

[108] S. Kurtz *et al.*, "Evaluation of high-temperature exposure of rack-mounted photovoltaic modules," in *2009 34th IEEE Photovoltaic Specialists Conference (PVSC)*, Jun. 2009, pp. 002399–002404. doi: 10.1109/PVSC.2009.5411307.

[109] ARPAE Emilia Romagna, "dext3r." https://simc.arpae.it/dext3r/ (accessed Sep. 01, 2022).

[110] O. Tremblay and L.-A. Dessaint, "Experimental Validation of a Battery Dynamic Model for EV Applications," *World Electric Vehicle Journal*, vol. 3, no. 2, pp. 289–298, Jun. 2009, doi: 10.3390/wevj3020289.

[111] Weixiang Shen, Thanh Tu Vo, and A. Kapoor, "Charging algorithms of lithium-ion batteries: An overview," in *2012 7th IEEE Conference on Industrial Electronics and Applications (ICIEA)*, Jul. 2012, pp. 1567–1572. doi: 10.1109/ICIEA.2012.6360973.

[112] "electricityMap | Live CO_2 emissions of electricity consumption." https://www.electricitymap.org/ (accessed Apr. 29, 2021).

[113] J.-W. A, "PV Status Report 2019," Publications Office of the European Union, Luxembourg (Luxembourg), 2019. doi: 10.2760/326629 (online),10.2760/329862 (print),10.2760/482505 (ePub).

[114] K. Mongird, v. Viswanathan, J. Alam, C. Vartanian, v. Sprenkle, and R. Baxter, "2020 Grid Energy Storage Technology Cost and Performance Assessment," Dec. 2020.

[115] W. Cole and A. W. Frazier, "Cost projections for utility-scale battery storage: 2020 update," Jun. 2020.

[116] H. Mahmood and J. Jiang, "Decentralized Power Management of Multiple PV, Battery, and Droop Units in an Islanded Microgrid," *IEEE Trans Smart Grid*, vol. 10, no. 2, pp. 1898–1906, Mar. 2019, doi: 10.1109/TSG.2017.2781468.

[117] S. Sitompul and G. Fujita, "Implementation of BESS Load Frequency Control in Islanded Microgrid System by Considering SOC," in *2020 IEEE PES Innovative Smart Grid Technologies Europe (ISGT-Europe)*, Oct. 2020, pp. 980–984. doi: 10.1109/ISGT-Europe47291.2020.9248945.

[118] V. Ramasamy, D. Feldman, J. Desai, and R. Margolis, "U.S. Solar Photovoltaic System and Energy Storage Cost Benchmarks: Q1 2021," Golden, CO (United States), Nov. 2021. doi: 10.2172/1829460.

[119] Chr. Lamnatou, D. Chemisana, and C. Cristofari, "Smart grids and smart technologies in relation to photovoltaics, storage systems, buildings and the environment," *Renew Energy*, vol. 185, pp. 1376–1391, Feb. 2022, doi: 10.1016/j.renene.2021.11.019.

[120] I. al Siyabi, A. al Mayasi, A. al Shukaili, and S. Khanna, "Effect of Soiling on Solar Photovoltaic Performance under Desert Climatic Conditions," *Energies (Basel)*, vol. 14, no. 3, p. 659, Jan. 2021, doi: 10.3390/en14030659.

[121] E. Urrejola *et al.*, "Effect of soiling and sunlight exposure on the performance ratio of photovoltaic technologies in Santiago, Chile," *Energy Convers Manag*, vol. 114, pp. 338–347, Apr. 2016, doi: 10.1016/j.enconman.2016.02.016.

[122] L. Zhou *et al.*, "The impact of air pollutant deposition on solar energy system efficiency: An approach to estimate PV soiling effects with the Community Multiscale Air Quality (CMAQ) model," *Science of The Total Environment*, vol. 651, pp. 456–465, Feb. 2019, doi: 10.1016/j.scitotenv.2018.09.194.

[123] T. Sarver, A. Al-Qaraghuli, and L. L. Kazmerski, "A comprehensive review of the impact of dust on the use of solar energy: History, investigations, results, literature, and mitigation approaches," *Renewable and Sustainable Energy Reviews*, vol. 22, pp. 698–733, Jun. 2013, doi: 10.1016/j.rser.2012.12.065.

[124] P. A. Patil, J. S. Bagi, and M. M. Wagh, "A review on cleaning mechanism of solar photovoltaic panel," in *2017 International Conference on Energy, Communication, Data Analytics and Soft Computing (ICECDS)*, Aug. 2017, pp. 250–256. doi: 10.1109/ICECDS.2017.8389895.

[125] A. Syafiq, A. K. Pandey, N. N. Adzman, and N. A. Rahim, "Advances in approaches and methods for self-cleaning of solar photovoltaic panels," *Solar Energy*, vol. 162, pp. 597–619, Mar. 2018, doi: 10.1016/j.solener.2017.12.023.

[126] Z. Wang, Z. Xu, Y. Zhang, and M. Xie, "Optimal Cleaning Scheduling for Photovoltaic Systems in the Field Based on Electricity Generation and Dust

Deposition Forecasting," *IEEE J Photovolt*, vol. 10, no. 4, pp. 1126–1132, Jul. 2020, doi: 10.1109/JPHOTOV.2020.2981810.

[127] M. Naeem and G. TamizhMani, "Cleaning frequency optimization for soiled photovoltaic modules," in *2015 IEEE 42nd Photovoltaic Specialist Conference (PVSC)*, Jun. 2015, pp. 1–5. doi: 10.1109/PVSC.2015.7355972.

[128] Huawei Mei, Zheji Shen, and Chujie Zeng, "Study on cleaning frequency of grid-connected PV modules based on Related Data Model," in *2016 IEEE International Conference on Power and Renewable Energy (ICPRE)*, Oct. 2016, pp. 621–624. doi: 10.1109/ICPRE.2016.7871152.

[129] D. L. Alvarez, A. S. Al-Sumaiti, and S. R. Rivera, "Estimation of an Optimal PV Panel Cleaning Strategy Based on Both Annual Radiation Profile and Module Degradation," *IEEE Access*, vol. 8, pp. 63832–63839, 2020, doi: 10.1109/ACCESS.2020.2983322.

[130] Z. Wu, W. Li, S. Kuka, and M. Alkahtani, "Analysis of Dust Deposition on PV Arrays by CFD Simulation," in *IECON 2019 - 45th Annual Conference of the IEEE Industrial Electronics Society*, Oct. 2019, pp. 5439–5443. doi: 10.1109/IECON.2019.8926897.

[131] H. al Badi, J. Boland, D. Bruce, and M. Albadi, "Dust Event Impact on Photovoltaic Systems: Role of humidity in soiling and self-cleaning," in *2018 IEEE International Conference on Smart Energy Grid Engineering (SEGE)*, Aug. 2018, pp. 342–345. doi: 10.1109/SEGE.2018.8499442.

[132] Z. Abderrezzaq, M. Mohammed, N. Ammar, S. Nordine, D. Rachid, and B. Ahmed, "Impact of dust accumulation on PV panel performance in the Saharan region," in *2017 18th International Conference on Sciences and Techniques of Automatic Control and Computer Engineering (STA)*, Dec. 2017, pp. 471–475. doi: 10.1109/STA.2017.8314896.

[133] A. Gholami, M. Ameri, M. Zandi, R. G. Ghoachani, S. Eslami, and S. Pierfederici, "Photovoltaic Potential Assessment and Dust Impacts on Photovoltaic Systems in Iran: Review Paper," *IEEE J Photovolt*, vol. 10, no. 3, pp. 824–837, May 2020, doi: 10.1109/JPHOTOV.2020.2978851.

[134] S. Warade and A. Kottantharayil, "Analysis of Soiling Losses for Different Cleaning Cycles," in *2018 IEEE 7th World Conference on Photovoltaic Energy Conversion (WCPEC) (A Joint Conference of 45th IEEE PVSC, 28th*

PVSEC & 34th EU PVSEC), Jun. 2018, pp. 3644–3647. doi: 10.1109/PVSC.2018.8547867.

[135] "Kipp&Zonen. DustIQ for Soiling Monitoring of PV." https://get.otthydrometinsights1.com/kippzonen/dustiq/ (accessed Apr. 02, 2020).

[136] "Moroni & Partners. PV Cleaning Optimizer." http://www.pvcleaning.com/ (accessed Apr. 02, 2020).

[137] "Kintech Engineering. Soiling measurement kit." https://www.kintech-engineering.com/products/soiling-measurement-kit/soiling-measurement-kit/ (accessed Apr. 02, 2020).

[138] "Atonometrics. PV Device Soiling Measurement Systems for PV Power Plants." http://www.atonometrics.com/products/soiling-measurement-system-for-pv-modules/ (accessed Apr. 02, 2020).

[139] "Campbell Scientific. Solar-Module Performance Monitoring System." https://www.campbellsci.com/smp100 (accessed Apr. 02, 2020).

[140] "NRG Systems. Soiling Measurement for PV Power Plants." https://www.nrgsystems.com/products/solar/detail/soiling-measurement-kit0 (accessed Apr. 02, 2020).

[141] "Ammonit. Soiling Measurement for PV Power Plants." https://www.ammonit.com/en/component/content/article/165-ammonit-messsysteme/solar-resource-assessment/407-solar-resource-assessment (accessed Apr. 02, 2020).

[142] D. Santoro *et al.*, "Development of a PV modules soiling monitoring system for smart maintenance," in *XXXIV Conference on Design of Circuits and Integrated Systems, DCIS 2019*, Nov. 2019.

[143] M. Simonazzi *et al.*, "Smart soiling sensor for PV modules," *Microelectronics Reliability*, vol. 114, p. 113789, Nov. 2020, doi: 10.1016/j.microrel.2020.113789.

[144] J. J. John, S. Warade, G. Tamizhmani, and A. Kottantharayil, "Study of Soiling Loss on Photovoltaic Modules With Artificially Deposited Dust of Different Gravimetric Densities and Compositions Collected From Different Locations in India," *IEEE J Photovolt*, vol. 6, no. 1, pp. 236–243, Jan. 2016, doi: 10.1109/JPHOTOV.2015.2495208.

[145] T. Pivem, F. de Oliveira de Araujo, L. de Oliveira de Araujo, and G. S. de Oliveira, "Application of A Computer Vision Method for Soiling Recognition in Photovoltaic Modules for Autonomous Cleaning Robots," *Signal*

Image Process, vol. 10, no. 03, pp. 43–59, Jun. 2019, doi: 10.5121/sipij.2019.10305.

[146] P. Cova, N. Delmonte, and M. Lazzaroni, "Photovoltaic plant maintainability optimization and degradation detection: Modelling and characterization," *Microelectronics Reliability*, vol. 88–90, pp. 1077–1082, Sep. 2018, doi: 10.1016/j.microrel.2018.07.021.

[147] M. R. Maghami, H. Hizam, C. Gomes, M. A. Radzi, M. I. Rezadad, and S. Hajighorbani, "Power loss due to soiling on solar panel: A review," *Renewable and Sustainable Energy Reviews*, vol. 59, pp. 1307–1316, Jun. 2016, doi: 10.1016/j.rser.2016.01.044.

[148] D. Dahlioui *et al.*, "Soiling effect on photovoltaic modules performance: New experimental results," in *2016 International Renewable and Sustainable Energy Conference (IRSEC)*, Nov. 2016, pp. 111–114. doi: 10.1109/IRSEC.2016.7983955.

[149] T. Huld, R. Müller, and A. Gambardella, "A new solar radiation database for estimating PV performance in Europe and Africa," *Solar Energy*, vol. 86, no. 6, pp. 1803–1815, Jun. 2012, doi: 10.1016/j.solener.2012.03.006.

[150] A. Reinhardt *et al.*, "On the accuracy of appliance identification based on distributed load metering data," in *2012 Sustainable Internet and ICT for Sustainability (SustainIT)*, 2012, pp. 1–9.

[151] P. Vithayasrichareon, G. Mills, and I. F. Macgill, "Impact of electric vehicles and solar pv on future generation portfolio investment," *IEEE Trans Sustain Energy*, vol. 6, no. 3, pp. 899–908, Jul. 2015, doi: 10.1109/TSTE.2015.2418338.

[152] S. Javaid, T. Kato, and T. Matsuyama, "Power Flow Coloring System over a Nanogrid with Fluctuating Power Sources and Loads," *IEEE Trans Industr Inform*, vol. 13, no. 6, pp. 3174–3184, Dec. 2017, doi: 10.1109/TII.2017.2733550.

[153] M. Jiao, F. Pan, X. Huang, and X. Yuan, "Evaluation on Total Cost of Ownership of Electric Forklifts with lithium-ion battery," in *Proceedings of 2021 IEEE 4th International Electrical and Energy Conference, CIEEC 2021*, May 2021. doi: 10.1109/CIEEC50170.2021.9510828.

[154] B. Aluisio, M. Dicorato, I. Ferrini, G. Forte, R. Sbrizzai, and M. Trovato, "Optimal sizing procedure for electric vehicle supply infrastructure based on

DC microgrid with station commitment," *Energies (Basel)*, vol. 12, no. 10, 2019, doi: 10.3390/en12101901.

[155] A. A. Nkembi, M. Simonazzi, D. Santoro, P. Cova, R. Menozzi, and N. Delmonte, "Designing power systems to charge electrical vehicle fleets in the industrial environment," in *Proceedings of SIE 2022, Lecture Notes in Electrical Engineering*, 2022.

[156] Infineon Technologies, "High-Side Switches." https://www.infineon.com/cms/en/product/power/smart-low-side-high-side-switches/high-side-switches/ (accessed May 10, 2021).

[157] C. Dolea and A. Mocanu, "Behavior Modelling Application for Automotive Industry," in *2007 International Semiconductor Conference*, Oct. 2007, pp. 455–458. doi: 10.1109/SMICND.2007.4519758.

[158] J. Schönberger, "An Overview of Simulation Tools," 2012, pp. 391–416. doi: 10.1007/978-1-4471-2885-4_13.

[159] J. H. Allmeling and W. P. Hammer, "PLECS-piece-wise linear electrical circuit simulation for Simulink," in *Proceedings of the IEEE 1999 International Conference on Power Electronics and Drive Systems. PEDS'99 (Cat. No.99TH8475)*, 1999, pp. 355–360 vol.1. doi: 10.1109/PEDS.1999.794588.

[160] M. Simonazzi, D. Santoro, M. Bernardoni, N. Delmonte, P. Cova, and R. Menozzi, "Behavioral modelling of PROFET^{TM} devices for system-level simulation of mission profiles in automotive environment applications," *Microelectronics Reliability*, vol. 126, p. 114324, Nov. 2021, doi: 10.1016/j.microrel.2021.114324.

[161] S. Reiter, A. Burger, A. Viehl, O. Bringmann, and W. Rosenstiel, "Virtual Prototyping Evaluation Framework for Automotive Embedded Systems Engineering," in *Proceedings of the Seventh International Conference on Simulation Tools and Techniques*, 2014. doi: 10.4108/icst.simutools.2014.254625.

[162] L. Li, L. Apvrille, and D. Genius, "Virtual Prototyping of Automotive Systems: Towards Multi-level Design Space Exploration." Oct. 2016. [Online]. Available: https://hal.sorbonne-universite.fr/hal-01365609

[163] Infineon Technologies, "BTS7008-2EPA Datasheet." https://www.infineon.com/dgdl/Infineon-BTS7008-2EPA-DataSheet-v01_20-

EN.pdf?fileId=5546d46258fc0bc1015902123568 76b1 (accessed May 10, 2021).

[164] V. Balakrishnan, T. Dinh, H.-P. Phan, D. V. Dao, and N.-T. Nguyen, "A Generalized Analytical Model for Joule Heating of Segmented Wires," *J Heat Transfer*, vol. 140, no. 7, Jul. 2018, doi: 10.1115/1.4038829.

[165] Stephane Fraissé, "Smart High Side Switches," *Application Note, Infineon Technologies*, 2010. https://www.infineon.com/dgdl/Infineon-Application+Note-PROFET+12V-What+the+designer+should+know-AN-v01_00-EN.pdf?fileId=5546d46259b0420a0159d5c957260d9c (accessed May 10, 2021).

[166] S. Ben-Yaakov, M. M. Peretz, and B. Hesterman, "A SPICE compatible behavioral electrical model of a heated tungsten filament," in *Twentieth Annual IEEE Applied Power Electronics Conference and Exposition, 2005. APEC 2005.*, pp. 1079–1084. doi: 10.1109/APEC.2005.1453128.

[167] W. R. Curtice and M. Ettenberg, "A Nonlinear GaAs FET Model for Use in the Design of Output Circuits for Power Amplifiers," *IEEE Trans Microw Theory Tech*, vol. 33, no. 12, pp. 1383–1394, Dec. 1985, doi: 10.1109/TMTT.1985.1133229.

[168] L. Zhang, H. Peng, Z. Ning, Z. Mu, and C. Sun, "Comparative Research on RC Equivalent Circuit Models for Lithium-Ion Batteries of Electric Vehicles," *Applied Sciences*, vol. 7, no. 10, p. 1002, Sep. 2017, doi: 10.3390/app7101002.